Retrieval of Atmospheric Composition from the MIPAS Satellite Instrument

Alastair Burgess

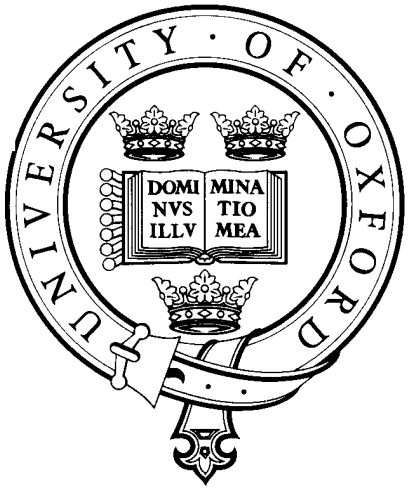

A thesis submitted for the degree of
Doctor of Philosophy

Michaelmas Term, 2005

Atmospheric, Oceanic and Planetary Physics
University of Oxford

Retrieval of Atmospheric Composition from the MIPAS Satellite Instrument

Alastair Buchanan Burgess,
Linacre College,
Atmospheric, Oceanic and Planetary Physics

A thesis submitted for the degree of Doctor of Philosophy in the University of Oxford
Michaelmas Term 2005

This thesis discusses the retrieval of atmospheric composition from the MIPAS satellite instrument, concentrating on four trace species; OCS, SF_6, SO_2 and NH_3.

A space-borne Fourier transform infrared spectrometer, MIPAS, is used to measure atmospheric limb spectra at high spectral and spatial resolution. Retrieval theory, concentrating on the optimal estimation approach is used to retrieve profiles of trace gases. The signal of species chosen for detailed investigation, ammonia, carbonyl sulphide, sulphur dioxide and sulphur hexafluoride, are at the limit of MIPAS detectability. This necessitates careful use of retrieval diagnostics to assess profile quality, followed by statistical methods to determine useful profiles. Methods of combining measurements before, during and after the retrieval process are also investigated. Finally, automation of quantitative assessments of retrieval quality, on an individual profile basis, have enabled large data volumes to be processed, giving insight into both global and seasonal processes.

Monthly mean fields for OCS are shown, with tropospheric values around 500 pptv and zonal and vertical structure that agrees with sparse balloon measurements. The stratospheric lifetime is calculated at 10 years with a sulphur loading of 0.48 Tg. A clear interannual trend of 0.30 pptv yr^{-1} is demonstrated for SF_6 with mean tropospheric values around 4.8 pptv for 2003. These results are used to derive age profiles for the atmosphere. SO_2 shows anthropogenic enhancement in the northern hemisphere of over 400 pptv with a mid stratospheric minimum of 10 pptv, in line with model distributions. There is a strong interhemispheric variability. Ammonia shows a strong vertical gradient with a mean value of around 10 pptv at 6 km.

Acknowledgements

In the course of this thesis, I have met many people and learnt many things.

Thank you to my supervisors, Don Grainger and Anu Dudhia, whose advice, comments and encouragement kept me on track.

Thank you to my CASE supervisor at RAL, Brian Kerridge, who has given me an external point of view. I also appreciate the time spent by Jolyon Reburn and others explaining the RAL retrieval.

Within AOPP, thanks to both Stuart Teasdale and Chris Lee, whose advice let the computer do the hard work so I didn't have to. Thanks, too, to Vivienne Payne who was always helpful and brought me up to speed when I arrived. Thank you to the many members of the coffee club, without whom I would never have discovered the joys of drinking sieved coffee outside in winter.

At ESTEC, thank you to Herbert Nett for introducing me to MIPAS. I also learned much from MIPAS meetings and have enjoyed time spent with their many participants.

I am grateful to my parents and especially to Helen, whose help, understanding and encouragement has enabled this thesis to be.

Contents

List of Figures

List of Tables

Chapter 1

Introduction

The aim of this thesis is the investigation of optimal methods to retrieve concentration profiles of minor species using data from the Michelson Interferometer for Passive Atmospheric Sounding (MIPAS).

It starts with a description of the MIPAS instrument and its parent satellite before considering the principles of the interferometer, radiative transfer and molecular spectroscopy. Subsequently, Chapter 2 will cover the basic elements of retrieval theory, concentrating on the optimal estimation method. New and prior work relating to coaddition is then discussed, considering the advantages and disadvantages of combining measurements before, during and after retrieval (Chapter 3).

The retrieval of a series of trace species, in order of method complexity is then considered, starting with carbonyl sulphide, OCS (Chapter 4). This is a significant precursor in the pathway leading to sulphuric acid aerosol in the stratosphere, responsible for a strong radiative forcing on the atmosphere. This work will then consider sulphur hexafluoride, SF_6 (Chapter 5) which is a useful tracer species with applications in model dynamics validation. Sulphur dioxide, SO_2 (Chapter 6) is then studied, requiring more complex retrieval methods. It too is involved in the formation of strato-

spheric aerosols. The final species, ammonia, NH_3 (Chapter 7), is a basic and highly soluble species, which is complementary to the acidic SO_2 and involved in its removal from the atmosphere. A more detailed discussion of each species appears in their respective chapters.

1.1 MIPAS

MIPAS is one of the instruments aboard the European Space Agency's Envisat satellite. The 8000 kg satellite and its associated payloads were launched on an Ariane 5 rocket from Europe's space port in French Guiana, on 1st March 2002. The sun-synchronous polar orbiting satellite has an altitude of 800 km and a period of one hundred minutes, giving approximately 14 orbits per day. A diagram of Envisat and its payload is shown in Figure 1.1. The Envisat mission and the MIPAS instrument are thoroughly described in special European Space Agency (ESA) publications (ESA, 2000a,b; Envisat, 2001).

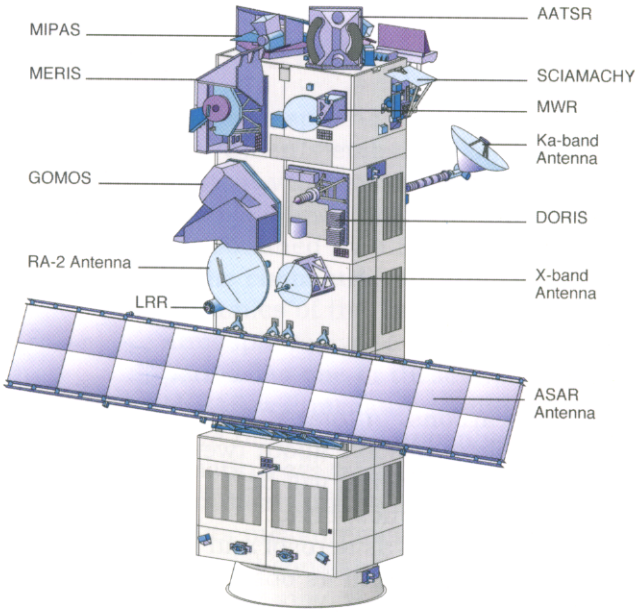

Figure 1.1: The Envisat instrument payload, (ESA, 2000a).

MIPAS is an actively cooled Fourier transform atmospheric thermal emission limb sounder, making observations between 685 and 2410 cm^{-1}, which corresponds to a wavelength range of 14.5–4.1 μm. This range enables the remote monitoring of a wide variety of trace species. The nominal altitude range observed by MIPAS is is 6–68 km, covering the upper troposphere / lower stratosphere (UTLS) region to the lower mesosphere. A complete limb scan sequence consists of 17 spectra at an unapodised spectral resolution of 0.025 cm^{-1} with tangent points at 68 km, 60 km, 52 km, 47 km, 42 km and downward to 6 km in 3 km steps. (ESA, 2000b). This thesis only considers data aquired using this measurement regime and resolution, taken before hardware problems forced a change in April 2004.

1.1.1 Background and History

A Fourier transform infrared (FTIR) instrument, such as MIPAS, is ideal for obtaining complete, high resolution, infrared (IR) spectra with good sensitivity.

FTIR instruments have a long history, giving good knowledge of their behaviour — an essential prerequisite of flying an instrument in space. There are aircraft, balloon and ground-based instruments but few FTIR instruments have flown in space prior to MIPAS. This is, in part, due to the demanding optical performance and platform stability required.

The drawback of an FTIR is its mechanical complexity. It contains optical elements that must be guided with high precision over extended distances. In addition, a very high alignment stability is required for all optical components in the interferometer. For MIPAS, the alignment constraints are unusually difficult as the optics are cooled down to -70°C to reduce the thermal self-emission.

Figure 1.2 shows the region of the electromagnetic spectrum sampled by MIPAS, along with the band positions of some of the major atmospheric constituents.

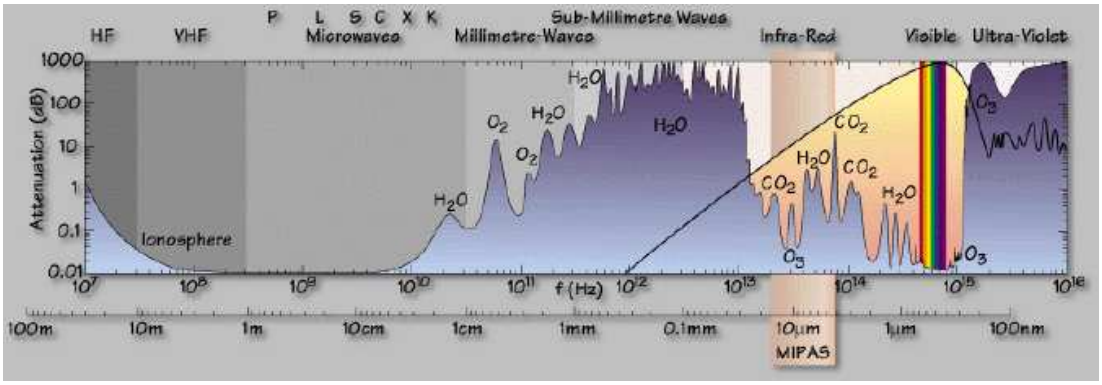

Figure 1.2: The measured data set covers a wide spectral range (685 cm^{-1} to 2410 cm^{-1}) at high spectral resolution, (ESA, 2000b).

1.1.2 Hardware

The spectral coverage of MIPAS itself is split up into five bands, summarised in Table 1.1. Bands A–B make use of a photoresistive type of detector that requires a correction to be applied to the spectra after measurement to account for the non-linear response to both the wavelength and the intensity of incident radiation. In contrast, bands C and D use a photovoltaic detector without such a limitation.

Table 1.1: MIPAS spectral bands.

Band	Spectral Range [cm^{-1}]
A	685–970
AB	1020–1170
B	1215–1500
C	1570–1750
D	1820–2410

Figure 1.3, shows the positions of the spectral features of some of the species that are found in these bands. The complexity of this plot emphasises the large amount of information available in each spectrum.

The radiometric requirements on MIPAS are highly demanding. A good radio-

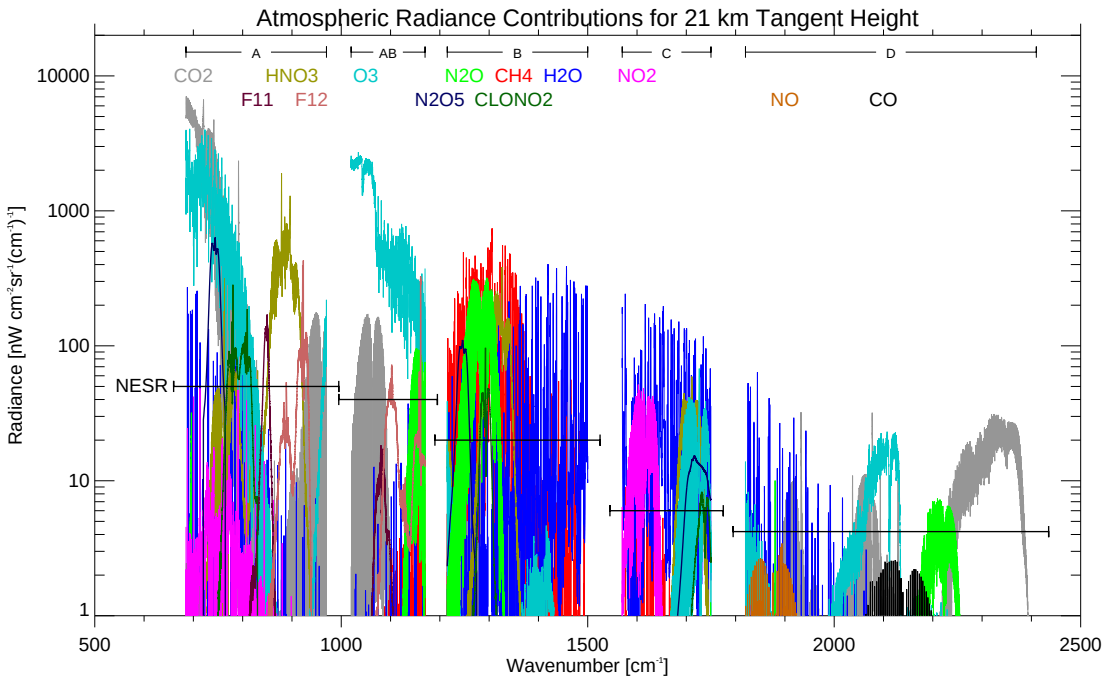

Figure 1.3: MIPAS bands and typical radiance contributions from various atmospheric species, calculated for a tangent height of 21 km (A. Dudhia, *pers. comm.*). The Noise Equivalent Spectral Radiance engineering requirements are shown as the horizontal lines.

metric sensitivity is essential to allow detection of weak atmospheric signals without additional averaging. Radiometric sensitivity is expressed here by the noise equivalent spectral radiance (NESR), which characterises the instrument noise in terms of incident radiance. The achieved design specifications of the MIPAS instrument required a sensitivity of $\leq$50 nW/(cm^2 sr cm^{-1}) at the long wavelength side, decreasing to $\leq$4.2 nW/(cm^2 sr cm^{-1}) at the short wavelength side (ESA, 2000b; ABB BOMEM, 2002). The NESR results are shown in Figure 1.4. The radiometric accuracy requirement was equally stringent and the calibration accuracy was reported as being well below one percent (Birk et al., 2002), an impressive achievement even for ground-based instruments. Such accuracy is necessary because a good absolute knowledge of the received radiance is important to the retrieval of the atmospheric temperature of the emitting layer — a key parameter in the retrieval process.

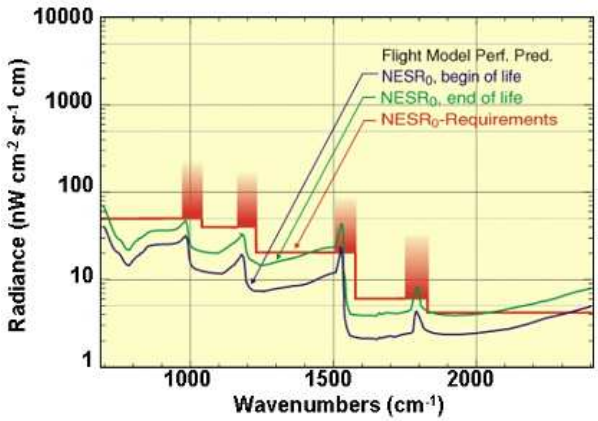

Figure 1.4: Comparison of the required engineering NESR against the launch and predicted end of life noise values (ESA, 2004). This shows how much better than the design specification the actual noise performance of the instrument was. The NESR is an important consideration in this thesis.

1.1.3 Geometry

MIPAS is designed for limb observations to balance maximum sensitivity and good vertical resolution. The instantaneous field of view is 3 km high to achieve a good vertical resolution, but 30 km wide to collect sufficient energy. This is shown in Figure 1.5.

1.1.4 Interferometry

The atmospheric radiance is collected by the front-end optics (mainly steering mirrors and a telescope) and is directed to a Michelson interferometer. The second interferometer input port is closed with a cold black body to suppress unwanted IR radiance. This black body information is used as part of the radiometric calibration. The input radiance is divided at the beamsplitter into two beams of similar intensity. They are directed to the moving retroreflectors — corner cubes — which return them to the beam combiner. The optical layout is shown in Figure 1.6.

Here the beams are superimposed and interfere, so that the resulting intensity in the

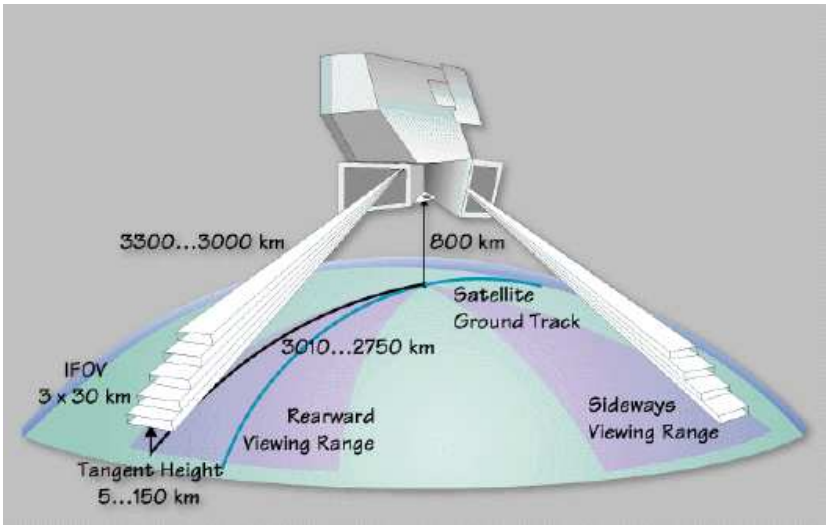

Figure 1.5: Viewing geometry of MIPAS. The instrument is capable of performing measurements in two pointing regimes, (ESA, 2000b).

output ports varies as a function of the optical path difference. At equal path length in both arms, there is 'zero-path difference' (ZPD) between the beam paths and thus constructive interference in the first output port increases the intensity to approximately twice the average value, while destructive interference in the other port reduces the intensity there to virtually zero. As the optical path difference changes, this interference causes the intensity to fluctuate between the two output ports. Importantly, however, the sum of the intensity in both ports stays constant. The interference-modulated signal as a function of optical path difference is an interferogram, and forms the basis of the raw data that MIPAS sends to Earth.

This interferogram is related to the spectrum of the incoming radiation by a Fourier transform. Therefore, the spectrum can be reconstructed from the recorded interferogram by the inverse Fourier transform. For MIPAS, this processing step is performed in the Envisat ground segment, providing maximum flexibility in the algorithms and to allow use of state-of-the-art processing hardware. The underlying theory is described in Section 1.3.

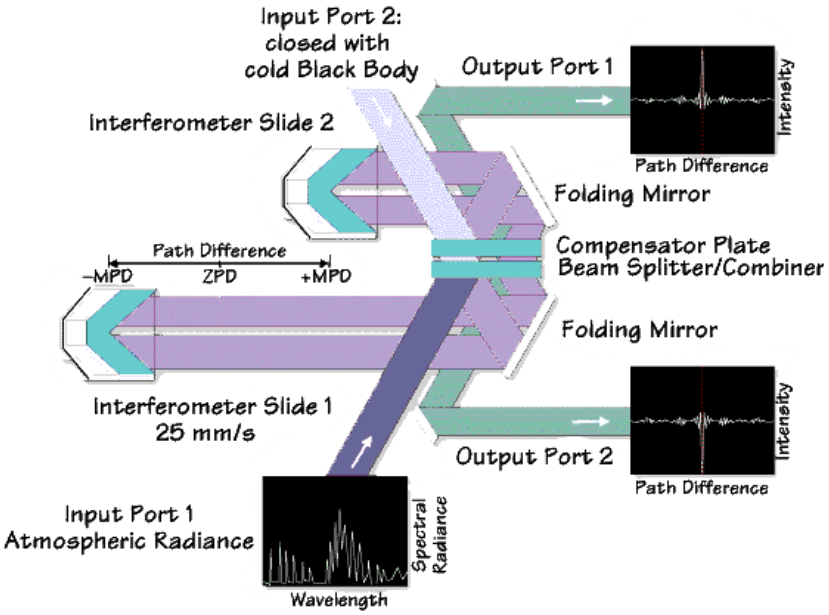

Figure 1.6: Diagram of the folded design of interferometer, (ESA, 2000b).

The spectral resolution of a FTIR is mainly determined by the maximum path difference (MPD) achievable in the particular interferometer. The MIPAS MPD of about 40 cm should give, in theory, a resolution of 0.025 cm^{-1} (this is the grid on which the spectra are supplied) but this theoretical resolution is degraded by convolution within the instrument with the ILS (instrument line shape). The ILS is not in reality a perfect sinc function (see below) as the FOV is finite which results in the incoming rays not being parallel. Some of them travel a slightly different path in the instrument, and so the interferogram is not sampled by an ideal boxcar function. For MIPAS, the obtained spectral resolution is about 0.035 cm^{-1} FWHM (Full width half maximum).

Due to the folded nature of the instrument design, the 40 cm path difference corresponds to a mechanical motion of each corner cube of around 50 mm.

To record a useful interferogram, the modulated output has to be sampled at extremely regular optical path difference intervals (the required sampling accuracy for MIPAS is about 30 nm). This is usually done with help of a laser beam transmitted in

the same optical set up, which is used to trigger the sampling electronics behind the detector at precise values.

1.1.5 Ground Segment

The steps in the chain leading from measurement to data in a form usable to the science community may be split into two conceptual pieces – the ‘Space Segment’ and the ‘Ground Segment’. Following acquisition of the interferogram, a lossy compression is applied (‘decimation’) and the data is split into packets ready for transmission to the ground stations. On arrival at the ground station(s) it enters the data processing chain. The data processing chain contains the following product levels:

- Level 0: Time-ordered satellite ‘packet’ data.
- Level 1A: Reconstructed interferograms.
- Level 1B: Radiometrically and spectrally calibrated geolocated spectra.
- Level 2: Profiles of atmospheric pressure, temperature and trace species.
- Level 3: Assimilated, global species fields (not handled by ESA).

Of these, Level 1B and Level 2 are the ones made available to the user community from ESA. They are split into ‘Near Real Time’ (NRT) and ‘Offline’ data products, where the NRT data is typically available hours after acquisition, but is less well calibrated and geolocated. The ‘Offline’ data is designed for general use and is the only type archived. This thesis deals almost exclusively with the Level 1B data, making use of ‘Offline’ products for the results presented.

1.2 Molecular Spectroscopy and Radiative Transfer

The determination of atmospheric structure and composition from satellite instruments, such as MIPAS, requires a detailed understanding of the underlying physical processes occurring in the atmosphere. The viability of remote sounding techniques is based on the fact that the atmosphere emits, absorbs and scatters electromagnetic radiation in a manner that is dependent on the molecules present. Many molecular species have characteristic spectral signatures — 'fingerprints' — in the infrared (vibrational transitions) and microwave (rotational transitions) regions. The strength and position of individual transitions depends on a complicated interaction of temperature, molecular symmetry/geometry and the individual masses of the elements that make up the molecule. Measurements of infrared thermal self-emission may be used to determine atmospheric temperature and composition.

The absorption coefficient, k, of a line centred at wavenumber ν_0, is a function of the line strength, S, absorber density/abundance, ρ, and the line shape function, g:

$$k(\nu, T, \rho) = S(T)g(\nu - \nu_0, T, \rho) \tag{1.1}$$

Spectral lines are broadened by molecular motion with respect to the point of observation (the Doppler effect) and by collisions with other molecules (Lorentz broadening). Doppler broadening dominates above 40 km and is also a function of temperature. Lorentz broadening dominates below about 10 km and is a function of pressure and temperature. Although included in the modelling of the atmosphere, a full discussion is beyond the scope of this thesis.

Application of radiative transfer techniques allows the simulation of the expected radiance for a known state. The atmosphere absorbs and emits radiation in the infrared according to its temperature and mix of constituent gases. The radiance leaving the at-

mosphere, and hence measured by the satellite instrument, can therefore be calculated. For a more in-depth textbook coverage of the theory of radiative transfer, see Goody and Yung (1989).

The radiance reaching the instrument from a certain atmospheric path consists of the radiance transmitted from one end of the path, and the balance between absorbtion and emission along the path to the instrument. If scattering is negligible (a reasonable approximation at infrared wavelengths in the absence of cloud) and the atmosphere is in Local Thermodynamic Equilibrium (LTE), then the emitted radiation is given by the Planck function:

$$B(\nu, T) = \frac{2hc^2\nu^3}{\exp(hc\nu/k_B T) - 1} \tag{1.2}$$

where ν is wavenumber, h is the Planck constant, c is the speed of light, T the temperature and k_B is the Boltzmann constant.

The monochromatic transmittance between a source and an observer is given by:

$$\tau\left(\nu, x_s, x_{obs}\right) = \exp\left(-\int_{x_s}^{x_{obs}} \Sigma_i k_i(\nu, x)\rho_i(x)\, dx\right) \tag{1.3}$$

The sum is over absorbers, i, with monochromatic absorption coefficient $k_i(\nu, x)$ and absorber number density $\rho_i(x)$. The source is at position x_s and the measurement is taken at x_{obs}.

The radiance L at the satellite as a function of wavenumber (ν) may be expressed as

$$L(\nu, x_{obs}) = L(\nu, x_s)\tau(\nu, x_s, x_{obs}) + \int_{x_s}^{x_{obs}} B(\nu, T(x))\frac{\partial\tau(\nu, x, x_{obs})}{\partial x}\, dx \tag{1.4}$$

$$= L(\nu, x_s)\tau(\nu, x_s, x_{obs}) + \int_{x_s}^{x_{obs}} B(\nu, T(x))\tau(\nu, x, x_{obs})\Sigma_i k_i(\nu, x)\rho_i(x)\, dx \tag{1.5}$$

For a limb viewing instrument, it is helpful to be able to set the background ra-

diance (the term transmitted through the whole view volume) $L(\nu, x_s)$ to zero, as the limb viewer sees cold space through the atmosphere.

Infrared spectroscopy is based on the vibrational-rotational transitions in gas molecules which gives rise to the spectral lines we observe. The positions, sizes and shapes of the spectral lines are determined by the type and abundance of the molecule and its temperature. To obtain the final observed line, external factors are included, such as the instrument optics and the effect of pressure.

1.3 Fourier Transform Spectroscopy

The interference-modulated signal $G(x)$ as a function of the optical path difference (x) measured by the detectors after the input radiance has passed through the Michelson optics is called an interferogram. It consists of a series of cosine waves, one per spectral point — about 60,000 for MIPAS.

$$G(x) = \int_{-\infty}^{+\infty} F(\nu) \cos(2\pi\nu x)\, \mathrm{d}\nu \tag{1.6}$$

The Fourier transform is used to recover the radiance spectrum, $F(\nu)$, observed by the instrument

$$F(\nu) = \frac{1}{L} \int_{-\infty}^{+\infty} G(x) \cos(2\pi\nu x)\, \mathrm{d}x \tag{1.7}$$

$$= \mathcal{F}(G(x)) \tag{1.8}$$

However, the optical path difference is finite in extent and hence the integral transform of a continuous function must be approximated by a discrete Fourier transform that makes use of a summation (Beer, 1992). For a number of points that is a power

of 2, the fast Fourier transform (FFT) is used to massively reduce the number of computations required (Griffiths and de Haseth, 1986). Normally padding of the measured interferogram ('zero-filling') is used to achieve this power of 2, although it does not add any information. The discrete transform and its inverse may be written as

$$I(m\delta x) = \sum_{k=0}^{N} F(k\delta\nu)\exp(2\pi ik\delta\nu \cdot m\delta x) \tag{1.9}$$

$$F(n\delta x) = \frac{1}{N}\sum_{j=0}^{N} I(j\delta\nu)\exp(-2\pi in\delta\nu \cdot j\delta x) \tag{1.10}$$

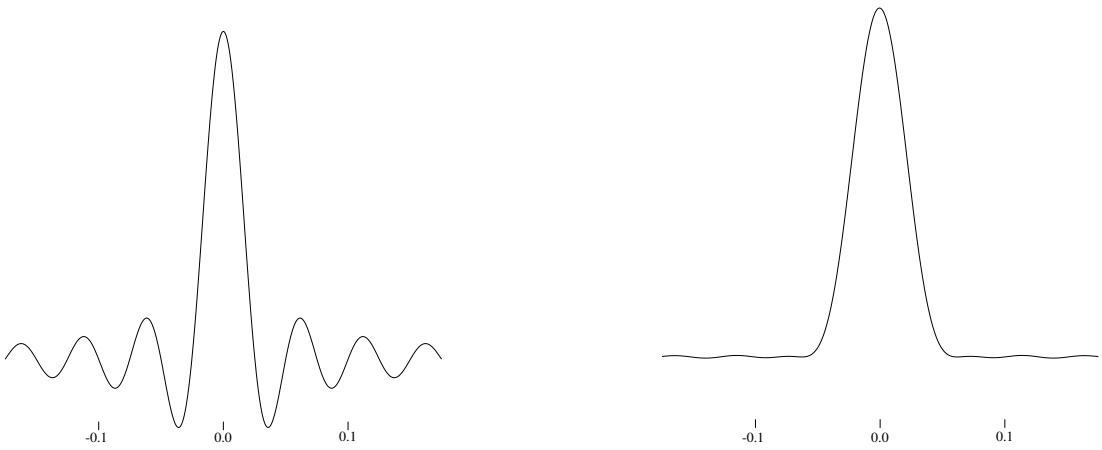

Figure 1.7: Sinc function (left) and apodised sinc function (right) with Norton–Beer strong apodisation.

A finite path difference is mathematically equivalent to the product of a continuous (infinite) interferogram with a boxcar function, $B(x)$, of the same width as the MPD (i.e. $B(x) = 1$ for $0 \leq x \leq$ MPD). Multiplication in the interferogram domain is equivalent to the convolution of the spectrum with a sinc function (the Fourier transform of a boxcar) in the spectral domain. This has the effect of smearing out the fine structure in the spectrum. In fact, the width of the sinc function determines the spectral resolution of the instrument (as it is proportional to the inverse of the MPD).

$$F(\nu)_{\rm obs} = \mathcal{F}(G(x)B(x)) \quad (1.11)$$

$$= F(\nu) * \mathcal{F}(B(x)) \quad (1.12)$$

The sinc function (Figure 1.7) is essentially the instrument line shape. It has side lobes/oscillations which extend out either side of the main peak. These oscillations cause interference between spectral lines, which can be damped out to some extent by using a numerical operation known as 'apodisation' [1]. Apodisation reduces the oscillations, but also widens the apparent peak of the ILS, reducing the spectral resolution and introducing correlations between spectral points. An ideal Fourier transform spectrometer would have a sinc function ILS. However, in practice, the ILS shape is affected by instrumental factors.

[1] *Apodise* literally means 'the cutting off of feet'.

Chapter 2

Theoretical Background

2.1 Retrieval Theory

Retrieval theory deals with solving the inverse problem. A set of measurements exists, with associated errors, that are representative of a true state. The aim is to obtain this true state based only on a finite number of imperfect measurements. The general approach involves the setting up and solution of a set of linear (or non-linear) equations based on these measurements, possibly with some external constraint. The naive inversion of this set of measurements is an ill-conditioned (ill-posed / under-constrained) problem for most practical situations, leading to meaningless solutions where the errors have been greatly magnified. This work makes extensive use of the standard reference on retrieval theory that deals with these problems, Rodgers (2000), and the following mathematical relations are quoted from this source and not derived. The optimal estimation approach will be the example case used to illustrate the pertinent concepts – other retrieval approaches, such as the least squares approach, will be touched upon later.

2.1.1 Forward Model

The measurement vector $\mathbf{y}$ of dimension m (e.g. a set of radiances as a function of wavenumber) and the state vector $\mathbf{x}$ of dimension n (e.g. values of temperature as a function of a vertical ordinate) are related by the forward model, $\mathbf{F}(\mathbf{x})$, which models the system under investigation. For a perfect forward model that includes all the complications of the real system,

$$\mathbf{y} = \mathbf{F}(\mathbf{x}) + \boldsymbol{\epsilon} \tag{2.1}$$

where the error (noise) on the measurement is given by $\boldsymbol{\epsilon}$. The forward model used in this work is the Reference Forward Model (RFM), developed at Oxford as a reference standard against which the optimised operational ESA forward model could be validated (Dudhia, 2002; Dudhia et al., 2002b).

2.1.2 Weighting Functions (Jacobians)

The linear problem is the simplest and most convenient case to study. If the problem is non-linear — and it almost always is — it is generally possible to linearise Equation 2.1 about a reference state, $\mathbf{x}_0$, provided $\mathbf{F}(\mathbf{x}_0)$ is linear to within the error bounds of the retrieval:

$$\mathbf{y} - \mathbf{F}(\mathbf{x}_0) = \frac{\partial \mathbf{F}(\mathbf{x}_0)}{\partial \mathbf{x}}(\mathbf{x} - \mathbf{x}_0) + \boldsymbol{\epsilon} \tag{2.2}$$

$$= \mathbf{K}(\mathbf{x} - \mathbf{x}_0) + \boldsymbol{\epsilon} \tag{2.3}$$

This defines the weighting function matrix $\mathbf{K}$ of dimension $m \times n$ (i.e. the dimensions of $\mathbf{y} \times \mathbf{x}$). Each element of $\mathbf{K}$ is the partial derivative of a forward model element with respect to a state vector element such that $\mathbf{K}_{ij} = \partial \mathbf{F}_i(\mathbf{x}_0)/\partial \mathbf{x}_j$. $\mathbf{K}$ is also known

as the Jacobian matrix and can be thought of as representing the change in radiance associated with, say, a 1 Kelvin change in the state vector.

2.1.3 Covariance Matrices

The retrieval system is never perfect, and errors occur in both the measurement and the accuracy of the simulation within the forward model. The error terms that influence the final result may be represented by covariance matrices. For example, element i, j of the error covariance matrix, $\mathbf{S}_\epsilon$, is given by

$$S_{ij} = \mathcal{E}\{\epsilon_i \epsilon_j\} \tag{2.4}$$

where $\mathcal{E}$ is the expected value operator and ϵ_i an element of the measurement error. The diagonal elements of $\mathbf{S}_\epsilon$ are the variances of the individual elements of $\mathbf{y}$ and the off-diagonal elements show correlations of size $S_{ij}/\sqrt{S_{ii} \times S_{jj}}$ between y-elements i and j.

2.1.4 Prior Information

The result can be constrained by the use of a priori information, $\mathbf{x}_a$, which is a 'best guess' of the target state with an associated uncertainty (covariance), $\mathbf{S}_a$. This could be based on previous measurements but is generally a climatological value. If one considers the set of all possible solutions consistent with the measurement vector and its associated errors, there are usually an infinite number of solutions. By using this estimate of what the state vector should be, even if this is very uncertain, a finite set of possible state vectors can be constrained as the retrieval. This is shown graphically in Figure 2.1.

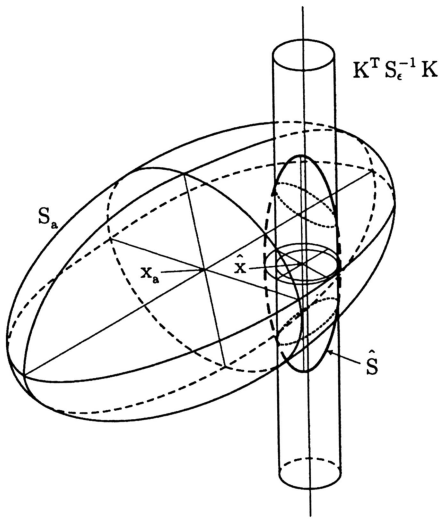

Figure 2.1: Illustrating the relationship between the prior state estimate, the measurement mapped in to state space and the posterior estimate (result) for a three-dimensional state space and a two dimensional measurement space. The large ellipsoid is a contour of the prior PDF, the cylinder is a contour of the PDF of the state given only by the measurement and the small ellipsoid is a contour of the resulting posterior PDF. Figure from Rodgers (2000).

2.1.5 Using Prior Information — Optimal Estimation

In general, there is no 'correct' solution obtainable because, fundamentally, a continuous function is being approximated by a finite number of imperfect measurements. Instead, the best solution is the most probable state. If the reasonable assumption of Gaussian statistics is made then the most probable state is the same as the expectation value of the state, $\hat{\mathbf{x}} = \int \mathbf{x} P(\mathbf{x}|\mathbf{y}) d\mathbf{x}$, where $P(\mathbf{x}|\mathbf{y})$ is the probability of $\mathbf{x}$ given $\mathbf{y}$.

By using our prior estimate of the state and our measurements with associated error covariances, the following expression may be derived (where the coordinate system has been chosen such that $\mathbf{x}_0$ and $\mathbf{F}(\mathbf{x}_0)$ are at the origins).

$$\hat{\mathbf{x}} = \mathbf{x}_a + (\mathbf{K}^T \mathbf{S}_\epsilon^{-1} \mathbf{K} + \mathbf{S}_a^{-1})^{-1} \mathbf{K}^T \mathbf{S}_\epsilon^{-1} (\mathbf{y} - \mathbf{K}\mathbf{x}_a) \tag{2.5}$$

where the total covariance of this result is given by

$$\hat{\mathbf{S}} = (\mathbf{K}^T \mathbf{S}_\epsilon^{-1} \mathbf{K} + \mathbf{S}_a^{-1})^{-1} \tag{2.6}$$

It is possible to see how the a priori uncertainty and measurement error covariances are both involved in determining the final choice of $\hat{\mathbf{x}}$ and its final uncertainty.

2.1.6 χ^2 as an indicator of convergence

This most probable solution, $\hat{\mathbf{x}}$, minimises a joint cost function (χ^2). An expression for the calculation of a scalar χ^2 quantity may be written as

$$\chi^2 = (\mathbf{y} - \mathbf{F}(\hat{\mathbf{x}}))^T \mathbf{S}_\epsilon^{-1} (\mathbf{y} - \mathbf{F}(\hat{\mathbf{x}})) + (\hat{\mathbf{x}} - \mathbf{x}_a)^T \mathbf{S}_a^{-1} (\hat{\mathbf{x}} - \mathbf{x}_a) \tag{2.7}$$

This quantity is useful in determining $\hat{\mathbf{x}}$ numerically and should tend to m. Commonly in retrieval codes a sequence of iterations are deemed to have converged if the change in χ^2 between steps is small.

2.1.7 Gain Matrix

The generalised inverse of the weighting function, $\mathbf{K}$, may be described as a *gain matrix*, $\mathbf{G}$ (it is also referred to in the literature as the measurement contribution function matrix). It is defined as

$$\mathbf{G} = \frac{\partial \hat{\mathbf{x}}}{\partial \mathbf{y}} \tag{2.8}$$

and determines the contribution of the measurement to the retrieved state. It can be shown that for an optimal solution

$$\mathbf{G} \;=\; (\mathbf{K}^T \mathbf{S}_\epsilon^{-1} \mathbf{K} + \mathbf{S}_a^{-1})^{-1} \mathbf{K}^T \mathbf{S}_\epsilon^{-1} \tag{2.9}$$

So Equation 2.5 may be more simply expressed as

$$\hat{\mathbf{x}} = \mathbf{x}_a + \mathbf{G}(\mathbf{y} - \mathbf{K}\mathbf{x}_a) \tag{2.10}$$

2.1.8 Averaging Kernel Matrix

The averaging kernel matrix, $\mathbf{A}$, relates the most probable state to the true state. It describes the subspace of state space in which the retrieval must lie.

$$\mathbf{A} = \frac{\partial \hat{\mathbf{x}}}{\partial \mathbf{x}} \tag{2.11}$$

It is possible to think of $\mathbf{A}$ as the weights of a weighted mean of the true state and a priori estimate that give rise to $\hat{\mathbf{x}}$. $\mathbf{A}$ is related to $\mathbf{G}$ such that

$$\mathbf{A} = \mathbf{G}\mathbf{K} \tag{2.12}$$

and

$$\hat{\mathbf{x}} = \mathbf{A}\mathbf{x} + (\mathbf{I} - \mathbf{A})\mathbf{x}_a \tag{2.13}$$

The rows of $\mathbf{A}$ are the averaging kernels (smoothing functions) that map the true state into retrieval space. The width of the kernel is a measure of retrieval resolution. The area of a kernel is approximately unity for an accurate retrieval and can be interpreted as a measure of the fraction of the retrieved value that originates from the signal and not the a priori.

2.1.9 Degrees of Freedom

The number of degrees of freedom, d, is a scalar measure of the number of independent quantities that can be measured. The largest number of degrees of freedom possible is

clearly determined by the number of elements in the measurement vector (or, indeed, the state vector — whichever is the smaller). There is the possibility of linear dependence between rows of $\mathbf{K}$ and it is probable that the error on some measurements is large enough to render their contribution to the retrieved state worthless. As a result, the number of independent pieces of information associated with signal (d_s) will be less than m (the number of elements of $\mathbf{y}$), with the difference being the number of degrees of freedom associated with the measurement error (noise). We may use $\mathbf{G}$ and $\mathbf{K}$ to calculate d_s,

$$d_s = \mathrm{tr}(\mathbf{GK}) \tag{2.14}$$

2.1.10 Information Content of a Measurement

The Shannon definition of information content (Shannon and Weaver, 1949) was originally developed to describe the information carrying capacity of communications channels. Information depends on the entropy of PDFs and is a scalar quantity that is ideally suited to optimising observing systems. The information component of a measurement (H) can be described as the factor by which our knowledge of a system is improved by taking a measurement ($\mathbf{y}$). In other words, the difference between $P(\mathbf{x})$ and $P(\mathbf{x}|\mathbf{y})$, where $S(P)$ is the entropy of P.

$$\begin{aligned} H &= S[P(\mathbf{x})] - S[P(\mathbf{x}|\mathbf{y})] && (2.15)\\ &= \frac{1}{2}\ln|\mathbf{S}_a| - \frac{1}{2}\ln|\mathbf{S}_{\hat{\mathbf{x}}}| && (2.16)\\ &= \frac{1}{2}\ln|\mathbf{S}_{\hat{\mathbf{x}}}^{-1}\mathbf{S}_a| && (2.17)\\ &= \frac{1}{2}\ln|\mathbf{I} - \mathbf{A}| && (2.18) \end{aligned}$$

This last relation is useful, as $\mathbf{A}$ is a readily available diagnostic, and so the information content of a retrieval can be simply derived.

2.1.11 Other Retrieval Methods

Least Squares

An alternative approach to optimal estimation is the use of a cost function based on a least squares difference between model and measurement. In this case, $\mathbf{A} = \mathbf{I}$. This is because in the cost function that is minimised during the retrieval (Equation 2.7), $\mathbf{S}_a^{-1} = \mathbf{O}$, corresponding to infinite prior uncertainty. The key quantities outlined for the optimal estimation approach previously are of slightly different form for the least squares fit.

$$\hat{\mathbf{x}} = \mathbf{G}\mathbf{y} \tag{2.19}$$

$$\mathbf{G} = (\mathbf{K}^T\mathbf{S}_\epsilon^{-1}\mathbf{K})^{-1}\mathbf{K}^T\mathbf{S}_\epsilon^{-1} \tag{2.20}$$

$$\mathbf{A} = \mathbf{I} \tag{2.21}$$

$$\hat{\mathbf{S}} = (\mathbf{K}^T\mathbf{S}_\epsilon^{-1}\mathbf{K})^{-1} \tag{2.22}$$

The ORM code, Ridolfi et al. (2000), is the prototype retrieval code that is implemented as the operational ESA retrieval scheme. It makes use of the least squares approach, and is run with a hard cutoff after a few iterations for the NRT data and this has a smoothing effect on the retrieved profile.

Conceptually, the main advantage is its lack of prior information, so no bias can be introduced other than a smoothness-type constraint. The disadvantage, especially when the problem is under-constrained as in the case of very dilute species, is a high

degree of instability and a tendency for the resulting retrieval to oscillate strongly.

Kalman Filter

The Kalman filter is a more computationally expensive approach to optimal estimation. After Rodgers (2000), the general formulation of the problem for discrete samples, t, that are spatial or temporal in nature may be described by an evolution (prediction) equation and a measurement equation:

$$\mathbf{x}_t = \boldsymbol{\mathcal{M}}_t(\mathbf{x}_{t-1}) + \boldsymbol{\xi}_t \tag{2.23}$$

$$\mathbf{y}_t = \mathbf{F}_t(\mathbf{x}_t) + \boldsymbol{\epsilon}_t \tag{2.24}$$

where $\mathcal{M}_t$ is a 'system model' that transforms $\mathbf{x}_{t-1}$ to $\mathbf{x}_t$ and $\boldsymbol{\xi}_t$ is a random vector known as the 'process noise'.

In our applications, the model is set to the result of the previous step (or the a priori for the first step), including its covariance. This is often called a Kalman Smoother. In effect, we are performing an iterative retrieval using new measurement information at each step, where an extra constraint is applied — the assumption that geospatially similar measurements will have similar characteristics. The profile retrievals of adjacent steps become correlated, with a strength related to the information content of each measurement in relation to the covariance of the previous step.

It may be clearer to look at the form of the χ^2 value used to determine $\hat{\mathbf{x}}$ for this approach, as compared to Equation 2.7,

$$\chi^2 = (\mathbf{y}_t - \mathbf{F}(\hat{\mathbf{x}}_t))^T \mathbf{S}_{t,\epsilon}^{-1} (\mathbf{y}_t - \mathbf{F}(\hat{\mathbf{x}}_t)) + (\hat{\mathbf{x}}_t - \hat{\mathbf{x}}_{t-1})^T \hat{\mathbf{S}}_{t-1}^{-1} (\hat{\mathbf{x}}_t - \hat{\mathbf{x}}_{t-1}) \tag{2.25}$$

The advantage of this approach is the minimisation of a priori influence by mak-

ing use of the previously retrieved state. The prior information only enters the final coadded state once as part of the initial conditions. The disadvantage is that it is essentially a smoothing in the time domain, which for satellite measurements also implies a smoothing in the along track direction. Fine latitudinal structure therefore becomes lost, but no more so than the other methods of coaddition. In addition, various spectral anomalies can strongly perturb one of the iterative steps. If this also strongly reduces the covariance, as is often the case, the Kalman filter approach will become 'locked' to this perturbed profile and take the information from many addditional measurements to return to the true mean state. Fortunately, this type of anomalous step can usually be spotted by examining the retrieval diagnostics at the end of each iteration and subsequently discarding the bad measurements from consideration.

Data Assimilation

More basic assimilation schemes make use of the Kalman filter, where a full model with associated error covariances is used. Assimilation is very computer intensive, as a model must be run in addition to the retrieval, but it has the advantage of allowing a 'snapshot' at any location and time to be taken. This result will have optimally used both the measurements and the additional constraints imposed by the model's knowledge of chemical processes, advection etc. Although beyond the scope of this thesis, the future of remote sensing for end-user applications will almost certainly make use of data assimilation due to its ability to give a best estimate of a value at any time and geolocation based on a rigorous combination of all the information and knowledge available together with their uncertainties.

2.2 Microwindows

A ‘microwindow’ is a small region of the spectrum with a high information content with respect to its target species, but with a minimised sensitivity to other parameters. Microwindows are used operationally on MIPAS data by ESA for the retrieval of the main trace gases listed in Chapter 1 (Echle et al., 2000). The development and application of microwindows for more dilute trace gases is being studied at Oxford (Dudhia, 2000; Dudhia et al., 2002a) and their use forms an important part of this thesis. These minor species, such as sulphur dioxide and sulphur hexafluoride are not available in the ESA products, but are significant in many areas of atmospheric research.

2.2.1 Microwindow Selection

One approach to the selection of these optimised spectral regions is by the simulation of random error propagation through the chosen retrieval scheme. It is then possible to choose measurements that best satisfy some selection criteria, such as maximised information content. This approach is best if random error on the measurement is the main source of retrieval uncertainty. It does not allow for systematic errors associated with unretrieved parameters, such as the modelling of minor interfering species based on their climatological abundance.

Alternatively, one may select microwindows by minimising the *total* error. This contains both random and systematic components. The simple implementation describes the profile as a set of independent single-layer retrievals, neglecting inter-level correlations.

A combination of these two approaches was used for the MIPAS microwindow selection, where a full profile retrieval is simulated, including the effect of systematic error terms. As part of the selection procedure, each microwindow is assigned a score

that can be used to sort the microwindows by various criteria. This allows the user to make decisions about many aspects of the final microwindows, such as computational vs accuracy trade-offs.

2.2.2 Error Propagation

Climatological uncertainties, as used operationally, were applied for all species, with uncertainties of 1 Kelvin for temperature, 2% for pressure and appropriate 1σ uncertainties for the trace gases (Remedios, 1999). The propagation of these errors and our initial estimates of their magnitude is significant for the MW selection.

When taking the mean of a set of measurements or retrievals, one must consider the behaviour of the systematic error terms over extended periods of time. Systematic error sources are defined here as correlated between measurements in a single profile. Fortunately, the majority of systematic terms are either constant over time or vary randomly on a scan by scan basis. For example, the error term relating to the accuracy of the spectral database is independent of orbit and would be constant over the year. Conversely, the retrieved water uncertainty varies randomly between profiles and so does not influence mid to long term means. The effect of variation in other systematics, especially interfering species, averages out over the course of a week or month. In fact, the only systematic error parameter that varies over the medium term is the gain (due to buildup of ice on the detectors), but the gain settings are recalibrated every orbit by reference to a black body and deep space views and so should have minimal effect on the mean. The various systematic parameters are defined in more detail in Table 2.1.

Table 2.1: Key to the various error terms considered by the microwindow selection.

Label	Error term
TEM	Temperature propagation error, effect of a nominal 1K uncertainty
PRE	Pressure propagation error, effect of a nominal 2% uncertainty
GRA	Error from a 1 K / 100 km gradient within the FOV along the LOS
SHIFT	Error from spectral calibration
SPREAD	Uncertainty in the ILS width of 2%
SPECDB	Uncertainty in spectroscopic line parameters
NONLTE	Error from assuming local thermodynamic equilibrium in the FM
CO2MIX	Residual error from neglecting CO_2 line mixing in the FM
CTMERR	Uncertainty in gaseous continua, with $\pm$25% modelling error
HIALT	Uncertainty in high altitude column, which is fixed
GAIN	Radiometric gain uncertainty, mainly from non-linearity correction
H2O	Water vapour profile uncertainty (climatological 1-σ)
O3	Ozone profile uncertainty
...	Uncertainty in other species' profiles

2.2.3 Modelling Errors

Following Dudhia (2000), the total error covariance is given by the sum of random and systematic terms,

$$\mathbf{S}_x^{\mathrm{tot}} = \mathbf{S}_x^{\mathrm{rnd}} + \mathbf{S}_x^{\mathrm{sys}} \tag{2.26}$$

where we have made the assumptions that the systematic error sources can be split into independent components $\mathbf{S}_y^i$

$$\mathbf{S}_x^{\mathrm{tot}} = \mathbf{G}\mathbf{S}_y\mathbf{G}^T + \sum_i \mathbf{G}\mathbf{S}_y^i\mathbf{G}^T \tag{2.27}$$

and that each independent systematic error component is fully correlated (i.e. $\mathbf{S}_y^i = (\delta\mathbf{y}^i)(\delta\mathbf{y}^i)^T$), so that

$$\mathbf{S}_x^{\mathrm{tot}} = \mathbf{G}\mathbf{S}_y\mathbf{G}^T + \sum_i (\mathbf{G}\delta\mathbf{y}^i)(\mathbf{G}\delta\mathbf{y}^i)^T \tag{2.28}$$

where $\delta \mathbf{y}^i$ are 'Error Spectra', representing the systematic errors. These spectra are calculated by perturbing the parameter in the forward model by the appropriate uncertainty and calculating the resulting difference from the unperturbed model result. As a result, covariances are not calculated, but this approach is much more efficient and simpler to implement.

2.2.4 Defining a Figure of Merit

Let us define $H^{'}$ as some scalar parameter that represents the overall effectiveness of the microwindow for its target, so that it may be maximised in an iterative microwindow selection. Building on the information theory concepts presented earlier (Equation 2.15), $H^{'}$ could be expressed in 'bits', as

$$H^{'} = -\frac{1}{2} \ln M \tag{2.29}$$

where M is some scalar function of the retrieval covariance. We could consider M to be the ratio of determinants of the retrieved over a priori covariances, which would result in $H^{'}$ being the information content, already discussed. Instead only the diagonal elements are used in order to minimise the variance of each profile element consided in isolation, rather than a full calculation of the information content which allows for off-diagonal correlations. The resulting functional form used may be written, after Dudhia (2000),

$$M = \frac{\Pi_j (S^{\mathrm{tot}}_{xjj} + 2S^{\mathrm{sys}}_{xjj})}{\Pi_j S^{\mathrm{tot}}_{ajj}} \tag{2.30}$$

where $\mathbf{S}^{\mathrm{tot}}_a$ is the a priori uncertainty (usually 100%) and the factor of two increases the weighting of the systematic errors. The overall selection procedure iteratively maximises this figure of merit depending on various selection constraints such as the maximum number of points.

2.2.5 Spectral Masks

The result of the selection procedure, which 'grows' each microwindow by adding adjacent points to a good initial candidate point, is a set of microwindows defined by boundaries in both the tangent altitude and wavenumber domains. There are two approaches to this process, which continues until any additional points in a microwindow result in a decrease in the figure of merit. 'Edgewise' growth ensures that every point within the microwindow boundaries are used in the retrieval – resulting in *rectangular microwindows*. 'Pointwise' allows the exclusion of individual points within the microwindow – *masked microwindows*. All the microwindows used in this thesis make use of this second approach during their selection. The masking of microwindow points is very useful as it allows the selective removal of systematic errors whilst maximising the sensitivity to the target species. Due to the high resolution of MIPAS, it is possible to selectively remove single measurement points within the microwindow that are strongly correlated with interfering species.

2.2.6 Accounting for Atmospheric Variability

Microwindows selected for one climatological assumption about the atmospheric state may not perform well if applied to observations of a very different state. For example, the polar winter conditions are characterised by low temperatures and low concentrations of some species, so the resulting microwindow selection will be biased towards good *precision* (signal-to-noise). If these same microwindows are applied to measurements at other latitudes or seasons, it is likely that improved *accuracy* would be a preferred characteristic as the signal-to-noise will no longer be the limiting case. In this work, a weighted mean set of the various seasonal and latitudinal atmospheres was used to generate a single microwindow set per species. This is in line with the

operational approach which aimed to minimise retrieval-induced discontinuities.

2.3 Retrieval Codes

The use of an optimal estimation method for retrieval of atmospheric constituents is applied in a tool named OPTIMO ('Oxford Processor to Invert MIPAS Observations') developed at Oxford (Jay, 2000). A more advanced tool, MORSE ('MIPAS Orbital Retrieval using Sequential Estimation') has been more recently released, allowing more complex retrieval strategies (Dudhia, 2005). Many of the suggestions, modifications and improvements made to the OPTIMO codebase have been incorporated into the default MORSE program, which has more advanced configuration options. This allows retrieval ideas to be explored without always necessitating a recompilation of the program code.

2.3.1 Comparing OPTIMO and MORSE

The first 18–24 months of the thesis work was performed using OPTIMO. A large amount of the work involved validation of microwindows and the general retrieval consistency, although little appears in this work. As a result of this validation work, on changing to MORSE, a set of test comparisons was created in order to check that the end result of the retrievals was the same to within the numerical accuracy of the host computer. This was generally the case, but there are some areas of numerical sensitivity that have been identified. These cases can be identified by looking at the retrieval diagnostics, so do not form a problem.

2.4 Cloud

One of the central problems faced in limb retrievals is contamination of the lower views with cloud. If a set of naive retrievals are performed over an entire orbit, it becomes obvious where thick cloud is located. There are large divergences and associated non-convergence of the optimal estimator, mainly over the equatorial regions. There is a strong correlation between these scans and high continuum in the spectra, which is indicative of cloud.

Detecting Cloud

Two methods for the detection of cloud have been suggested. The first, by Spang et al. (2004), relies on the ratio between the radiance of two small regions of the spectrum within a band. In our case, the ratio is within band A for the ranges 788.20–796.25 cm^{-1} and 832.30–834.40 cm^{-1}. A threshold value for this ratio has been defined by external validation. As a result, all ratios falling below 1.8 are flagged as cloudy. The second method (D. Grainger, *pers. comm.*) looks at a single point at 960.7 cm^{-1} and defines an absolute radiance cutoff of 125 nW/(cm^2 sr cm^{-1}) below which the spectrum is nominated as cloud free. A significant point to note is the use of arbitrary thresholds in cloud detection methods, as there is a continuous gradient of cloud optical thicknesses from zero to infinity. It is necessary to choose the point at which the damaging influence of cloud contamination on the retrieval is low enough to be accommodated by the continuum retrieval, whilst maximising the number of low-altitude profile points retrieved. For example, the cloud ratio threshold can be set as high as 4.0 if significant sensitivity to thin cirrus or high altitude polar stratospheric clouds is expected. The continuum retrieval is a single state vector element per microwindow, that is only used below 30 km, which attempts to fit a simple

continuum-type feature to the measured radiance. This enables the forward model to better represent the remaining radiance. It is discussed in more detail in the MORSE documentation, Dudhia (2005).

Masking Cloud

When the threshold test for cloud is failed for an altitude, the retrieval does not attempt to fit the contaminated level and the associated radiance is removed. The profile value at the cloudy level is still able to vary in order to best fit the remaining measurements, but rarely does so. As a result, these cloudy levels tend to retain their initial values. Because of this, the presence of the cloud is recorded along with the retrieval diagnostics so that the combination of retrievals to generate zonal and other means does not have a low or high concentration bias caused by a priori values.

2.5 Summary

A key development as applied to the MIPAS instrument has been in the automation of the selection of microwindows. The automation has both improved the quality of the microwindows selected and removed the human subjective element from their selection. An additional benefit has been a full error analysis that is created as a consequence of the selection process.

The application of optimal estimation techniques to retrieval problems has become an established technique. It is perhaps interesting to note that recent work on SF_6 profile retrieval from IR spectral data (Rinsland et al., 2003) made use of an optimal estimator as a part of the retrieval whereas the same author in the early 1990s (Rinsland et al., 1993) did not. Optimal estimation has many advantages that originate in the solid mathematical framework that underlies the inverse problem which allows the detailed

tracking of errors, e.g. Rodgers (1990), through the retrieval.

Chapter 3

Coaddition

One of the consequences of the investigation of species near to the random noise limit of MIPAS is frequent recourse to coaddition of data to improve the signal-to-noise. This is possible at many points between measurement and final product. Conceptually, there are three distinct areas for coaddition:

- Before the first forward model calculation — coaddition of radiance (or, indeed, interferograms).

- During the retrieval – performing some combination on intermediate radiances, profiles or residuals.

- After the final forward model calculation – coaddition of retrieved profiles.

Each of these approaches has its own benefits and problems. These are discussed below.

3.1 Radiance

Taking the mean of a set of radiances before retrieval is conceptually the simplest noise reduction method and is already performed, to some extent, on board the instrument where the radiation striking the detectors is integrated over the time between interferometer fringes. On ground, one can take it a step further and perform the retrieval on a mean radiance vector calculated from an arbitrarily long set of measurements. In practice, the choice of spectra that make up the average would be based on prior physical knowledge and assumptions of the sampled atmospheric states. The aim would usually be to combine measurements from similar atmospheric volumes where the associated state parameters do not greatly differ. This is due to the inherent assumption of linearity made when taking the mean. There are few changes to the atmospheric state vector that result in purely linear differences in radiance.

The error on the retrieved state ($\delta\hat{x}$), that arises from the propagation of non-linear state terms into the mean radiance, is quantified in this section. It is defined as the difference between some combination of retrievals ($\overline{\hat{x}}$) from n measurements and the true mean state of the same set of n atmospheres ($\bar{x}$). We assume a scalar retrieval and measurement for simplicity.

Following the notation of Rodgers (2000), consider a measured radiance, y, composed of a *forward function,* f, acting on the true state of the atmosphere, x and a measurement random error, ϵ. The function f is *not* the same as the forward model, but is the 'real' physical manifestation of a certain state that gives rise to the quantity that is actually measured. As a result, it allows us to investigate the effects purely due to non-linearities and not forward modelling errors.

We have already seen in the previous chapter that we may write an expression for

a measured radiance in terms of the atmospheric state as

$$y_i = f(x_i) + \epsilon_i \tag{3.1}$$

where y_i is the i^{th} measurement in a set of measurements of i different states. A Taylor expansion of f about the mean state, $\bar{x}$, yields,

$$f(x_i) = f(\bar{x}) + \frac{\partial f}{\partial x}(x_i - \bar{x}) + \frac{1}{2}\frac{\partial^2 f}{\partial x^2}(x_i - \bar{x})^2 + \dots \tag{3.2}$$

We may then form a general expression for the mean of the n radiances, $\bar{y}$

$$\begin{aligned}
\bar{y} &= \frac{1}{n}\sum_{i=1}^{n} y_i \\
&= \frac{1}{n}\sum_{i=1}^{n}\left(f(\bar{x}) + \frac{\partial f}{\partial x}(x_i - \bar{x}) + \frac{1}{2}\frac{\partial^2 f}{\partial x^2}(x_i - \bar{x})^2 + \epsilon_i\right) && (3.3)\\
&= f(\bar{x}) + \frac{1}{2}\frac{\partial^2 f}{\partial x^2}\sigma_x^2 + \bar{\epsilon} && (3.4)
\end{aligned}$$

Where we have identified $\frac{1}{n}\sum(x_i - \bar{x})^2$ as σ_x^2, which is the variance of the atmospheric state about the mean. The mean of the noise is $\bar{\epsilon}$. Making the resonable assumption that the noise distribution is Gaussian, the magnitude of $\bar{\epsilon}$ should be, on average, $\sqrt{n}$ times smaller than the noise on an individual measurement, ϵ_i. This is the intended benefit of the averaging.

The radiance that would be observed from the true mean of the atmospheric states, $\bar{x}$, is $y_{\bar{x}} = f(\bar{x})$. So an expression for the difference in radiance, δy, from these two approaches is

$$\begin{aligned}
\delta y &= \bar{y} - y_{\bar{x}} && (3.5)\\
&= \bar{\epsilon} + \frac{1}{2}\frac{\partial^2 f}{\partial x^2}\sigma_x^2 && (3.6)
\end{aligned}$$

This is a useful quantity that relates the 'true' radiance associated with the mean of the states to the mean of the radiances. The sensitivity is determined by the second derivative of the forward function and the atmospheric variance about the mean state. In summary, $\bar{\epsilon} < \epsilon_i$ is the intended advantage of radiance averaging, while the $\frac{\partial^2 f}{\partial x^2}$ term is the undesireable non-linearity contribution.

3.1.1 Retrieving from Mean Radiance

By considering a transfer function (also known as a retrieval function), R, which defines our whole observing system, a retrieved state vector ($\hat{x}_i$) can be expressed as

$$\hat{x}_i = R(y_i) \tag{3.7}$$

So, the retrieval from the mean radiance is given by expanding R to first order about the radiance associated with the true mean, $y_{\bar{x}}$, and then substituting our expression for δy,

$$\begin{aligned} \hat{x}_{\bar{y}} &= R(\bar{y}) && (3.8)\\ &= R(y_{\bar{x}}) + \frac{\partial R}{\partial y}(\bar{y} - y_{\bar{x}}) && (3.9)\\ &= \bar{x} + \frac{\partial R}{\partial y}\bar{\epsilon} + \frac{\partial R}{\partial y}\frac{1}{2}\frac{\partial^2 f}{\partial x^2}\sigma_x^2 && (3.10) \end{aligned}$$

where we have ignored second and higher order expansion terms.

Our measure of the error from retrieving from coadded radiances relative to the radiance associated with the true mean state vector, $\delta\hat{x}$, for this case is given by

$$\begin{aligned} \delta\hat{x} &= \hat{x}_{\bar{y}} - \bar{x} && (3.11)\\ &= \frac{\partial R}{\partial y}\bar{\epsilon} + \frac{1}{2}\frac{\partial R}{\partial y}\frac{\partial^2 f}{\partial x^2}\sigma_x^2 && (3.12) \end{aligned}$$

We are able to use the same arguments for the equivalent calculation taking into account the whole state vector, $\mathbf{x}$ and radiance vector, $\mathbf{y}$. The partial derivatives of f and R are identified with $\mathbf{K}$ and $\mathbf{G}$, respectively. For example, the initial expansion using the forward model instead of the forward function becomes

$$\mathbf{F}(\mathbf{x}) = \mathbf{F}(\bar{\mathbf{x}}) + \mathbf{K}(\mathbf{x}-\bar{\mathbf{x}}) + \nabla_x \left[\mathbf{K}(\mathbf{x}-\bar{\mathbf{x}})\right](\mathbf{x}-\bar{\mathbf{x}}) + ... \tag{3.13}$$

where $\nabla_x = \frac{\partial}{\partial \mathbf{x}}$. The resulting expression for the error due to a non-linear forward function is (after Equation 3.12)

$$\delta\hat{\mathbf{x}} = \hat{\mathbf{x}}_{\bar{\mathbf{y}}} - \bar{\mathbf{x}} \tag{3.14}$$

$$= \mathbf{G}\bar{\boldsymbol{\epsilon}} + \mathbf{G}\nabla_{\mathbf{x}} \left[\mathbf{K}(\mathbf{x}-\bar{\mathbf{x}})\right](\mathbf{x}-\bar{\mathbf{x}}) \tag{3.15}$$

3.2 Retrieved Profiles

This approach is as conceptually simple as using the mean radiances. The results of a set of retrievals can simply be coadded and the associated random error should reduce in line with standard Gaussian statistical assumptions.

For a particular true state, x_i, with associated radiance y_i the retrieved state, $\hat{x}_i$, may be written, after Equation 3.7, as

$$\hat{x}_i = R(y_i) \tag{3.16}$$

$$= R(f(x_i) + \epsilon_i) \tag{3.17}$$

$$= x_i + \frac{\partial R}{\partial y}\epsilon_i + \frac{1}{2}\frac{\partial^2 R}{\partial y^2}\epsilon_i^2 \tag{3.18}$$

where we have expanded about the true state. This retrieval non-linearity, neglected for the radiance case previously, represents large oscillations in ill-conditioned matrix

inversions attributed to the effect of the random noise.

If we take the mean of n retrievals corresponding to the previous set of n radiances, y_i, with a mean of their associated atmospheric states of $\bar{x}$ then we may write

$$\begin{aligned} \bar{\hat{x}} &= \frac{1}{n}\sum_{i=1}^{n}\hat{x}_i & (3.19)\\ &= \frac{1}{n}\sum_{i=1}^{n}\left(x_i + \frac{\partial R}{\partial y}\epsilon_i + \frac{1}{2}\frac{\partial^2 R}{\partial y^2}\epsilon_i^2\right) & (3.20)\\ &= \bar{x} + \frac{\partial R}{\partial y}\bar{\epsilon} + \frac{1}{2}\frac{\partial^2 R}{\partial y^2}\sigma_\epsilon^2 & (3.21) \end{aligned}$$

where the standard deviation of the noise is given by σ_ϵ. The corresponding δx is given by

$$\begin{aligned} \delta\hat{x} &= \bar{\hat{x}} - \bar{x} & (3.22)\\ &= \frac{\partial R}{\partial y}\bar{\epsilon} + \frac{1}{2}\frac{\partial^2 R}{\partial y^2}\sigma_\epsilon^2 & (3.23) \end{aligned}$$

and in the general vector case, this can be expressed as

$$\delta\hat{\mathbf{x}} = \mathbf{G}\bar{\boldsymbol{\epsilon}} + \nabla_{\mathbf{y}}[\mathbf{G}\boldsymbol{\sigma}_\epsilon]\boldsymbol{\sigma}_\epsilon \quad (3.24)$$

where the first part of this expression is identical to that of retrieving from the mean radiance (Equation 3.12). It corresponds to the mapping of noise on the measurement into the retrieval domain.

In the linear case, both $\nabla_{\mathbf{y}}\mathbf{G}$ and $\nabla_{\mathbf{x}}\mathbf{K}$ are zero and so the expressions for $\delta\hat{\mathbf{x}}$ are equivalent.

For the non-linear case, $\nabla_{\mathbf{x}}\mathbf{K}$ — the derivative of the Jacobian — can be thought of as the non-linear sensitivity to differences between members of the set of atmospheres sampled. $\nabla_{\mathbf{y}}\mathbf{G}$ is the non-linear sensitivity to the random noise in the radiance domain.

3.3 Intermediate Steps – Residuals

Unfortunately, there are few methods to improve the performance of a radiance coaddition approach, as the key problem lies in the non-linear response to atmospheric variability. Improvements to the signal-to-noise and hence the random error on the measurement are generally hardware, design time and operations-planning driven.

For an existent dataset, it may be possible to use prior retrievals of dominant species in region of interest. These would be used to refine the selection of radiances to a subset that share high degrees of atmospheric similarity. These could then be coadded and a full retrieval performed. This has the effect of reducing the variance and associated quantities. The non-linearity of $f(x)$ is still a problem but by reducing the variance, the non-linearity decreases in importance.

Extending this idea of using information from a retrieval to improve the coaddition of radiances, consider the residual radiance from a retrieval of non-target state parameters, such as temperature. The major cause of the non-linearity is generally the effect of temperature and pressure, which may not themselves be poorly retrieved as their signal is strong. By retrieving such parameters first for a set of measurements, a major non-linear component can be mostly removed.

Let $\mathbf{x}$ contain just two components – the temperature t and our target species VMR, v. Equation 3.1 becomes

$$y_i = f(t_i, v_i) \tag{3.25}$$

where we have neglected the random error ϵ_i component for clarity — its contribution is expected to be as in the previous sections. A Taylor expansion of y_i about $\bar{t}$ and $\bar{v}$ gives

$$f(t_i, v_i) = f(\bar{t}, \bar{v}) \quad + \quad \frac{\partial f}{\partial t}(t_i - \bar{t}) + \frac{\partial f}{\partial v}(v_i - \bar{v}) + \frac{1}{2}\frac{\partial^2 f}{\partial t^2}(t_i - \bar{t})^2 + \frac{1}{2}\frac{\partial^2 f}{\partial v^2}(v_i - \bar{v})^2$$

$$+ \quad \frac{1}{2}\frac{\partial^2 f}{\partial t \partial v}(t_i - \bar{t})(v_i - \bar{v}) + \frac{1}{2}\frac{\partial^2 f}{\partial v \partial t}(v_i - \bar{v})(t_i - \bar{t}) + \ldots \quad (3.26)$$

Using a similar approach to Equation 3.3 by taking the average of the set of n radiances, $f(t_i, v_i)$,

$$\begin{aligned}
\bar{y} &= \frac{1}{n}\sum_{i=1}^{n} f(t_i, v_i) \\
&= \frac{1}{n}\sum_{i=1}^{n}\left(f(\bar{t},\bar{v}) + \frac{\partial f}{\partial t}(t_i - \bar{t}) + \frac{1}{2}\frac{\partial^2 f}{\partial t^2}(t_i - \bar{t})^2 + \frac{\partial f}{\partial v}(v_i - \bar{v}) + \frac{1}{2}\frac{\partial^2 v}{\partial v^2}(v_i - \bar{v})^2 \right) \\
&= f(\bar{t},\bar{v}) + \frac{1}{2}\frac{\partial^2 f}{\partial t^2}\sigma_t^2 + \frac{1}{2}\frac{\partial^2 f}{\partial v^2}\sigma_v^2 \qquad (3.27)
\end{aligned}$$

where we have neglected higher order terms and seen that the mean of the cross terms is zero, i.e. $\sum_{i=1}^{n} \frac{\partial^2 f(\bar{t},\bar{v})}{\partial t \partial v}(t_i - \bar{t})(v_i - \bar{v}) = 0$. Subtracting $y_{\bar{x}} = f(\bar{t},\bar{v})$ from Equation 3.27 will give an equivalent result to our previous expression for δy, Equation 3.5, but where x is split into components associated with t and v.

$$\delta y = \bar{\epsilon} + \frac{1}{2}\frac{\partial^2 f}{\partial t^2}\sigma_t^2 + \frac{1}{2}\frac{\partial^2 f}{\partial v^2}\sigma_v^2 \qquad (3.28)$$

Repeating the argument from Equations 3.7 to 3.12 we way write an expression for the error on this retrieval,

$$\delta\hat{x} = \frac{\partial R}{\partial y}\bar{\epsilon} + \frac{1}{2}\frac{\partial R}{\partial y}\frac{\partial^2 f}{\partial t^2}\sigma_t^2 + \frac{1}{2}\frac{\partial R}{\partial y}\frac{\partial^2 f}{\partial v^2}\sigma_v^2 \qquad (3.29)$$

Now consider performing a set of ideal temperature retrievals, such that $t_i = \hat{t}_i$. The 'residual' radiance for each measurement after the retrieval of the temperature, z_i,

is expressed as

$$z_i = f(t_i, v_i) - f(t_i) + \epsilon_i \tag{3.30}$$

The mean of these residuals, $\bar{z}$, along with the mean of the temperatures, $\bar{t}$, is used to form the radiance associated with our best estimate of the target, $y_{\hat{v}}$. Calculating the mean removes all $(t_i - \bar{t})$ terms in Equation 3.26. As a result, following the same approach as before, we are left with

$$y_{\hat{v}} = f(\bar{t}, \bar{v}) + \frac{1}{2}\frac{\partial^2 f}{\partial v^2}\sigma_v^2 + \bar{\epsilon} \tag{3.31}$$

Using this result, we write the error on the retrieval as before,

$$\begin{aligned} \delta\hat{x} &= R(y_{\hat{v}}) - R(\bar{y}) && (3.32)\\ &= \frac{\partial R}{\partial y}\bar{\epsilon} + \frac{1}{2}\frac{\partial R}{\partial y}\frac{\partial^2 f}{\partial v^2}\sigma_v^2 && (3.33)\\ &\leq \frac{\partial R}{\partial y}\bar{\epsilon} + \frac{1}{2}\frac{\partial R}{\partial y}\frac{\partial^2 f}{\partial x^2}\sigma_x^2 \end{aligned}$$

In other words, if the temperature is well retrieved, the $\frac{\partial^2 f}{\partial t^2}\sigma_t^2$ term can be eliminated leaving only the term in v. This term is smaller than the sum of both terms and as a result the retrieval of the temperature before coaddition acts to improve the error on the retrieval ($\delta\hat{x}$). This result shows that it is possible to improve on the non-linearity errors associated with coadding radiances. In practice, there is a small uncertainty on the temperature retrieval. The result is still an improvement over the mean radiance case because the retrieval has the effect of reducing the apparent temperature variance within the residuals. Temperature and pressure are essential candidates for prior retrieval because the radiance non-linearity associated with these terms is large.

3.4 Prior Information Biases

As shown in Equation 2.9 for a single retrieval, the final retrieved state ($\hat{\mathbf{x}}$) contains contributions from both the atmospheric state ($\mathbf{y}$) and the a priori ($\mathbf{x}_a$). The atmospheric contribution is related to the noise of the measurement relative to the uncertainty of the prior information ($\mathbf{S}_\epsilon$ to $\mathbf{S}_a$). As a result, for low signal-to-noise measurements, there can be a significant bias in the mean of a set of profiles.

Let us consider the simple case of a scalar retrieval. We may write after Equation 2.12,

$$\hat{x}_i = x_a + A(x_i - x_a) + G\epsilon_i \tag{3.34}$$

$$= x_a + \frac{\partial R}{\partial y}\frac{\partial f}{\partial x}(x_i - x_a) + \frac{\partial R}{\partial y}\epsilon_i \tag{3.35}$$

using our previous notation. Up to now, this chapter has made the implicit assumption that $\mathbf{A} = \mathbf{I}$. In other words, we have been performing a least squares type retrieval and neglecting the a priori. Indeed, if we set $A = 1$ in the above expression, we find we reach the relation given in Equation 3.18, neglecting the higher order term. In the optimal estimation approach, the final state is the weighted mean of the prior and measurement information, where A is the weighting parameter.

Now, consider taking the mean of a set of profiles described by Equation 3.34.

$$\bar{\hat{x}} = x_a + A(\bar{x} - x_a) + G\bar{\epsilon} \tag{3.36}$$

$$= (1 - A)x_a + \bar{x} + G\bar{\epsilon} \tag{3.37}$$

This shows that the relative weights of the a priori and the result are not changed by coaddition. The calculation of $\delta\hat{x}$ for this result gives the same expression as before for the mean of profiles (Equation 3.23), but there is the addition of a constant bias

term of $(1 - A)x_a$.

In vector notation this expression for $\bar{\hat{x}}$ may be simply written as

$$\bar{\hat{\mathbf{x}}} \;=\; (\mathbf{I} - \mathbf{A})\mathbf{x}_a + \bar{\mathbf{x}} + \mathbf{G}\bar{\epsilon} \tag{3.38}$$

Remembering that $\mathbf{A}$ contains contributions from both $\mathbf{S}_\epsilon^{-1}$ and $\mathbf{S}_a^{-1}$, both these uncertainties are equally reduced when taking the mean. The relative weights of $\mathbf{x}$ and $\mathbf{x}_a$ are unchanged, but the effective strength of the prior constraint has decreased by $\sqrt{n}$, just as the random error component has decreased. The effect is similar to setting the a priori uncertanity to 10% instead of 100%, but using an instrument with ten times better noise characteristics. The problem with the increased constraint lies in the use to which the resulting mean of the profiles is put. The reduction in $\mathbf{S}_\epsilon$ will give more confidence in the result — better precision. The bias from the a priori is unchanged, however, and so the accuracy for the measurement is not improved. In order to improve accuracy, the a priori bias must be removed. The a priori can dominate the mean because its value does not vary, only its contribution. Thus it cannot average to 'zero' as we are hoping the random noise will.

3.4.1 Removing Prior Information

It is possible is some cases to remove the a priori information used in the retrieval after $\hat{\mathbf{x}}$ has been calculated. A simple version was applied in Burgess et al. (2004), that made use only of the diagonals in the covariance matrix to reduce the influence of the a priori.

A more rigorous method is used in this thesis. It considers the whole covariance matrix instead of just the diagonals (Rodgers, 2000). As $\mathbf{S}_a$ tends to $\mathbf{O}$ for the least squares approach, which contains no priori information, the maximum likelihood so-

lution is

$$\hat{\mathbf{x}}' = [\mathbf{K}^T\mathbf{S}_\epsilon^{-1}\mathbf{K}]^{-1}\mathbf{K}^T\mathbf{S}_\epsilon^{-1}[\mathbf{y} - F(\mathbf{x}) + \mathbf{K}\mathbf{x}] \quad (3.39)$$

$$= [\mathbf{S}_{\hat{\mathbf{x}}}^{-1} - \mathbf{S}_a^{-1}]^{-1}(\mathbf{S}_{\hat{\mathbf{x}}}^{-1}\hat{\mathbf{x}} - \mathbf{S}_a^{-1}\mathbf{x}_a) \quad (3.40)$$

Unfortunately, this only works if the problem is overconstrained, otherwise $\mathbf{K}^T\mathbf{S}_\epsilon^{-1}\mathbf{K} = \mathbf{S}_{\hat{\mathbf{x}}}^{-1} - \mathbf{S}_a^{-1}$ is singular.

An improvememnt to this method is to replace the a priori with one closer to the true state ($\mathbf{x}_b$), which we should have a better estimate of than we did before the retrieval. Now $\mathbf{K}^T\mathbf{S}_\epsilon^{-1}\mathbf{K}$ being singular is less of a problem.

$$\hat{\mathbf{x}}'' = (\mathbf{S}_{\hat{\mathbf{x}}}^{-1} - \mathbf{S}_a^{-1} + \mathbf{S}_b^{-1})^{-1}[\mathbf{S}_{\hat{\mathbf{x}}}^{-1}\hat{\mathbf{x}} - \mathbf{S}_a^{-1}\mathbf{x}_a + \mathbf{S}_b^{-1}\mathbf{x}_b] \quad (3.41)$$

Complete Removal

A more complete discussion on the use of retrievals which contain a priori information can be found in Rodgers (2000). In essence, the problem must be reformulated with a hard constraint instead of the soft constraint provided by the prior information.

3.5 Summary

The coaddition of data to improve signal-to-noise is non trivial. The difference between the true mean and the retrieved mean can be quantified in terms of derivatives of the forward and retrieval functions. Each approach has its own problems, however, in both deviation from the true mean and in numerical (computational) complexity. A consequence of using optimal estimation is the presence of priori information in the final result, which is more pronounced for weak signals. Coaddition does not remove

this, and actually has the effect of increasing the apparent strength of the constraint. Methods exist to remove the prior information a posteriori, but none of them are ideal. These methods are applied to real data in the following chapters.

Chapter 4

Carbonyl Sulphide

In this chapter we make use of MIPAS retrievals to quantitatively determine the distribution of carbonyl sulphide in the Upper Troposphere Lower Stratosphere (UTLS) region. From a measurement point of view it is an unusual species in that its strongest emissions are in the D band of the MIPAS instrument.

4.1 Introduction

The high quantities of sulphate aerosol that are injected into the stratosphere by major volcanic events have been shown to have a significant impact on atmospheric temperature and chemistry (Seinfeld and Pandis, 1997). Even in the absence of these dramatic volcanic events, a perennial sulphate aerosol layer remains in the stratosphere, influencing a variety of chemical processes. This layer is distributed from the tropopause up to 30 km, with a maximum at around 20 km. Above this, the sulphuric acid aerosols are thought to enter the gas phase and undergo photolysis in the increased UV flux.

The origin of this Stratospheric Sulphate Aerosol (SSA) has been a subject of debate since it first attracted attention in the middle of last century (Junge et al., 1961).

Despite advances in in-situ and remote sensing, the origins of these aerosols are still not well known (Leung et al., 2002; Moller, 1995; Chin and Davis, 1995). Mechanisms for the formation of SSAs through stratospheric oxidation of precursors such as SO_2 and H_2S have been suggested, but these species are very susceptible to tropospheric oxidation. Consequently, although they do contribute significantly to the mass of SSAs, the incoming flux of these precursor species from the upper troposphere is low. In addition, uncertainty remains as to the anthropogenic influence on atmospheric sulphur, especially as aerosols (Rodhe, 1999; Lelieveld et al., 1997).

Carbonyl Sulphide (OCS) is relatively unreactive in the troposphere, so is available to enter the stratosphere in significant quantities and has consequently been proposed as the major source of SSAs by Crutzen (1976). More recently, however, this almost exclusive assignment of the origin of SSAs to OCS has come into question (Chin and Davis, 1995). Recent analyses have shown deep convective events can transport large quantities of OCS through the tropical tropopause into the stratosphere (Notholt et al., 2003). Here it is susceptible to oxidation by hydroxyl radical attack and to ultraviolet photolysis (Barnes et al., 1994). Large uncertainties in the atmospheric sulphur budget compound the problems associated with in-situ measurement of background SSAs and makes an exact assessment of the OCS contribution extremely difficult (Watts, 2000; Kettle et al., 2002a). In fact, models suggest that under 50% of SSA particles originate from OCS, the remaining sources of sulphate being an almost equal split between upward transport and SO_2 oxidation (Timmreck, 2001; Pitari et al., 2002). A common observation by these authors, of special relevance to this work, is the scarcity of globally distributed profile information for both OCS and SO_2, making the validation of model predictions difficult. The solution to this problem is ideally suited to satellite measurements, with their excellent spatial coverage.

4.1.1 Chemistry

The most abundant sulphur-containing gases in the atmosphere are carbon disulphide (CS_2), carbonyl sulphide (OCS), dimethyl sulphide (DMS or SMe_2), hydrogen sulphide (H_2S) and sulphur dioxide (SO_2). They are all subject to oxidation by a variety of species, such as ozone and hydroxyl radicals, and are also directly photolysed. Mechanisms exist for the production of OCS from the more reduced species in both the troposphere and stratosphere, although the relative contribution of each is dependent upon atmospheric conditions. For example, laboratory studies by Barnes et al. (1994) have shown that OCS is a product of DMS oxidation by OH radicals, at low NO_x concentrations. Another significant pathway to OCS formation involves the methyl sulphide ($CH_3S^{\cdot}$) radical, formed from cleavage of DMS and its reaction with molecular oxygen. Carbon disulphide is also a significant precursor, undergoing direct reaction with the OH radical to produce OCS (Barnes et al., 1994). Diurnal and seasonal variations in OCS, as a result of the oxidation of these precursor species, have been reported at the surface by Griffith et al. (1998). The thermodynamic end-point of all these oxidative reactions is the sulphate ion (SO_4^{2-}), which is the major constituent of tropospheric and stratospheric sulphate aerosols.

OCS undergoes very little photolysis in the troposphere, due to the low UV flux below 290 nm (Chin and Davis, 1995). The chemical lifetime of OCS in the troposphere is the longest of the sulphur gases, approximately 17–25 years, based on typical oxygen and hydroxyl radical abundances (Pitari et al., 2002). With an absorption maximum around 223 nm, photolysis becomes a very significant loss mechanism in the stratosphere, especially above the ozone maximum. Approximately 71% of the OCS loss is due to photolysis, with 22% from reaction with atomic oxygen and 7% from hydroxyl radicals (Seinfeld and Pandis, 1997).

The tropospheric lifetime of OCS is shorter than the purely chemical consideration

implies, mainly due to ocean-surface processing. For example, Barnes et al. (1994) state a tropospheric lifetime of 2.5 years. Griffith et al. (1998), by considering variability in existing measurements, calculate a minimum of 2.8 years and an alternative estimate, based on dividing the total atmospheric mass of OCS (approximately 5 Tg) by the estimated OCS source strength is 4.3 years (Chin and Davis, 1995).

Regardless of the variation in estimates, a free tropospheric lifetime measured in years results in a well mixed species giving a significant abundance of OCS at the tropopause. This makes it available for transport into the stratosphere where oxidation to sulphate occurs (Barnes et al., 1994). These lifetimes also mean that diurnal variations are unlikely to be present in the well-mixed, free troposphere.

The rapid increase in radical concentrations in the stratosphere accounts for the majority of non-photolytic loss above the tropopause. An estimate of total stratospheric lifetime, considering a simple 1D chemical model, is approximately 10 years. This is twice its global atmospheric lifetime and has implications for significant OCS transport back in to the troposphere and subsequent sinking at the surface (Chin and Davis, 1995).

The volume mixing ratio of OCS is fairly constant in the troposphere, as its lifetime is significantly longer than vertical transport timescales. Literature values of the order of 500 pptv (parts per trillion by volume) are common ranging from a minimum of 480 ± 13 pptv reported in the Southern Hemisphere to 525 ± 17 pptv reported at a Northern Hemispheric location by Sturges et al. (2001) and Griffith et al. (1998) and references therein. Localised, elevated measurements up to 600 pptv, associated with biomass burning, have been reported in deep convective events near the tropical tropopause by Notholt et al. (2003). Some authors argue that no large trend in concentration has occurred over the last 25 to 50 years (Rinsland et al., 1992b; Sturges et al., 2001). Measurements from the ATMOS instrument on the space shuttle around

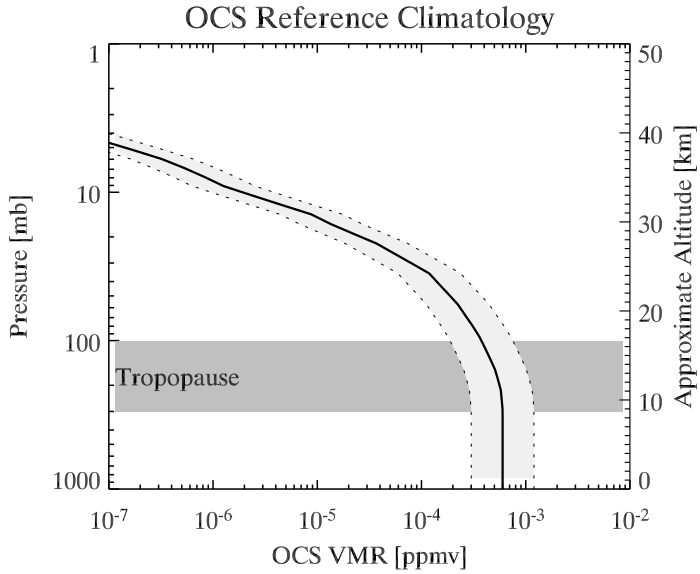

Figure 4.1: Climatological carbonyl sulphide profile and its associated 1-σ uncertainty, based on work on MIPAS reference atmopsheres by Remedios (1999). The approximate location of the tropoause is shown by the shaded region and both pressure and corresponding altitude are shown on the vertical axes.

30°N in 1985 and 1994 showed no clear trend (0.1±0.4% yr^{-1}) (Rinsland et al., 1996). More recently, small decreases in column amounts have been reported: 0.28±0.08% yr^{-1} by Mahieu et al. (1997), 0.45±0.09% yr^{-1} by Zander and et al. (1988) and 0.25±0.04% yr^{-1} by Rinsland et al. (2002). These trends have been observed in the Northern Hemisphere and are attributed to the decline of the viscose-rayon industry (a source of CS_2), and the observation that anthropogenic CS_2 production has shifted from Europe to Asia over the last 30 years — away from well-used measurement stations. On longer timescales, polar firn air data from both hemispheres covering the last century have shown little variation from modern values (Sturges et al., 2001). However, Antarctic ice core data, dated to the 1600s, gives values around 370±40 pptv, implying that the current anthropogenic contribution to OCS is approximately 25% (Aydin et al., 2002). A global mean reference climatology used as a baseline OCS

distribution is shown in Figure 4.1.

Of interest to the modeller is the isotopic fractionation processes that occur in the atmosphere as a result of the subtly different energy landscapes within which the isotopomers exist. As a result, it is possible to trace the origin of the OCS within a volume of air based on a ratio of two isotopomers (Leung et al., 2002; Goldman et al., 2000). Unfortunately, this isotopic fingerprinting relies on small changes in the ratio between two isotopomers and, as ^{34}S is only 5% as abundant as the major isotope ^{32}S, the OC^{34}S spectral features will be more than an order of magnitude below the instrument noise, before the small enrichment/depletion has taken place. As a result, it is not thought feasible to retrieve OCS isotopic ratios at this time.

4.1.2 Sources and Sinks

Of the sulphur-containing gases, the major anthropogenic emissions are in the form of SO_2, whereas the dominant biogenic emissions consist of (mainly oceanic) DMS (Seinfeld and Pandis, 1997; Chin and Davis, 1995) and CS_2 (Watts, 2000). However, due to its lifetime OCS accounts for more than 80% of gas phase sulphur in the upper troposphere (Leung, 2003; Notholt et al., 2003).

OCS is directly emitted from the oceans as a by-product of both biological and photochemical reactions (Weiss and Andrews, 1995; Zepp and Andrae, 1994). The presence of dissolved organic matter can significantly enhance the production and emission of OCS. It is also formed in the atmosphere from several precursor species, notably DMS and CS_2, as previously discussed. Several studies have shown OCS flux sensitivity to season and light levels (Ulshofer et al., 1995; Hobe et al., 2002). Soils act as both sources and sinks of OCS depending on their reducing nature (‘oxic’ or ‘anoxic’ soils). Plants, notably boreal forests, act as a net sink of OCS (Watts, 2000).

Another surface source of OCS lies in anthropogenic activities, such as biomass

burning and rice cultivation. OCS originating from biomass burning shows good correlations to both CO concentrations and to certain geographical regions, such as south-east Asia (Nguyen et al., 1994). Rice cultivation shows a very strong seasonal variation in OCS and DMS emissions, peaking in August and being almost zero for the period October to May as discussed by Yang et al. (1998). Aluminium products have also been highlighted as a previously unnoticed source (Harnisch et al., 1995; Watts, 2000). As a result, it is possible to assign a direct anthropogenic contribution (source) term of approximately 15%, similar to but independently derived from the 25% (direct and indirect) OCS anthropogenic source estimated from ice core data by Aydin et al. (2002), above.

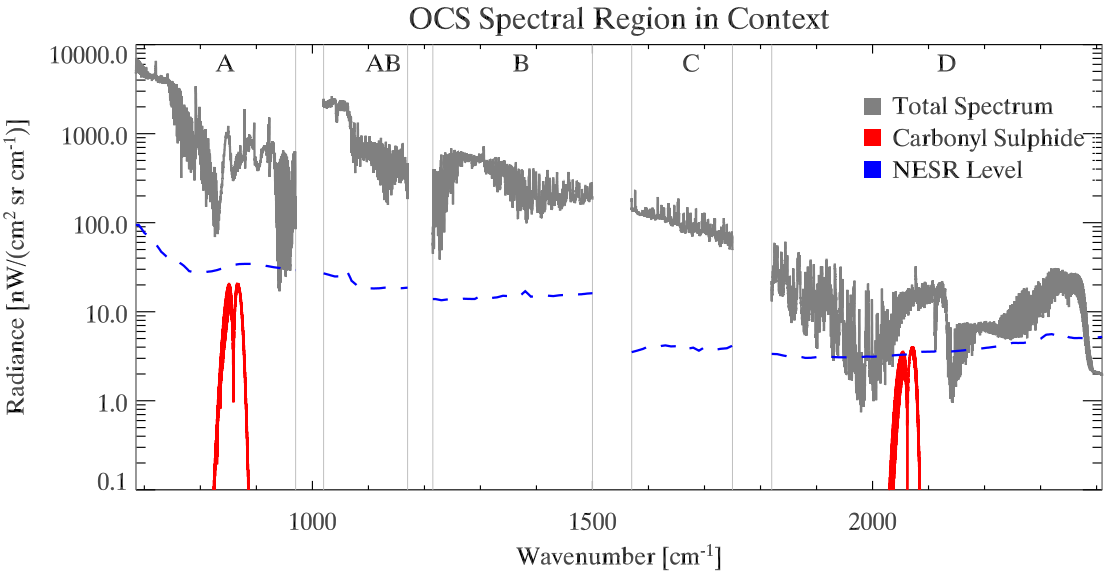

Figure 4.2: A radiative transfer simulation of the relative intensity of carbonyl sulphide features compared to the total radiance for a 12 km tangent altitude, based on climatological abundances. The instrument noise level (NESR) is shown as the dashed line. For the linear triatomic OCS the two main emission bands are the ν_1 and ν_3 around 860 cm^{-1} and 2062 cm^{-1}, with the latter being about 70 times stronger with respect to the noise level.

Collating the known source and sink terms, and applying seasonal variability has allowed the derivation of OCS integrated flux for both hemispheres and the whole

globe. The interesting conlusion is that both hemispheres are approximately ‘in phase’, showing maximum source terms in November to February and minimum source terms (possibly a net sink) around July and August (Kettle et al., 2002a). Problems still exist in ‘closure’ of the cycle (Chin and Davis, 1995, 1993), though balance has recently been achieved, to within large errors on all the terms, by Watts (2000).

There is some evidence for a tropospheric Northern Hemisphere to Southern Hemisphere VMR ratio of 1.0 – 1.3 from Griffith et al. (1998). Other studies quote values as large as 1.6 – 2 pptv per degree latitude of northward movement (Barnes et al., 1994; Johnson, 1981). A simple box model has led to the suggestion that there is a steady-state OCS flux into the Southern Hemisphere, although biases are likely to exist from the locations of time series sampling stations (Kettle et al., 2002b). There seem to be no discussions of stratospheric interhemispheric ratios in the literature and, based on lifetime and trend considerations, they would be expected to be small.

In summary, there are a variety of competing lifetime estimates for OCS in the atmosphere. The global free tropospheric abundance of OCS is virtually constant with time at approximately 500 pptv. Once in the stratosphere the abundance has decreased to around 5 pptv by 30 km.

4.2 Considerations

By considering the climatological abundance shown in Figure 4.1 the Oxford radiative transfer code (RFM), can be used to calculate the radiance contribution from OCS at the position of the satellite. Figure 4.2 shows this contribution along with the instrumental noise level and the total emitted radiation, for an observation limb tangent altitude of 12 km. The OCS contribution is greater than the instrumental noise for several regions of lines in the D band.

OCS is almost unique amongst the MIPAS observable species in that all of its selected microwindows make use of the D band (the other non operational species are carbon monoxide and nitrogen monoxide). It was thought at design time that some operational species would make use of this region, but the selection of optimised microwindows leans heavily towards the higher radiances in the longer wavelength bands due to sigal to noise considerations. The D band is on the tail of the Planck curve and consequently this OCS work has enabled some validation of the bands' calibration that was previously lacking, Burgess and Dudhia (2003).

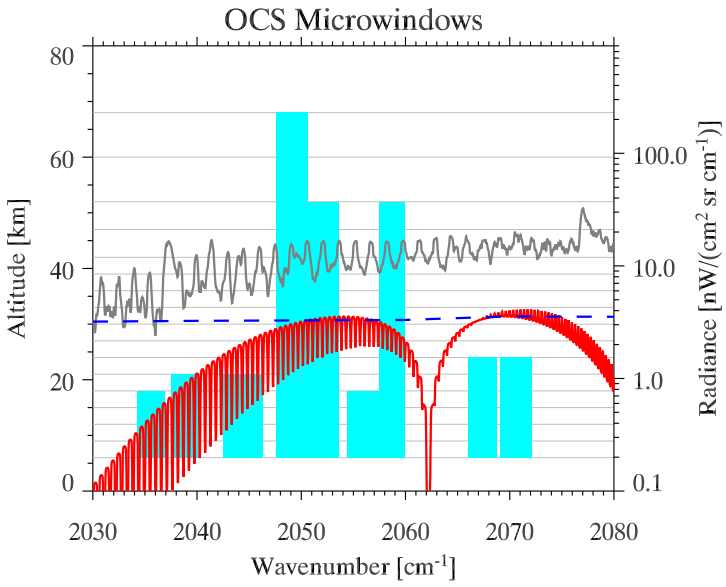

Figure 4.3: Plot indicating the position and altitude range (shaded blocks) of the selected microwindows, overplotted with the total radiance (right axis) within the significant spectral region for a 12 km tangent height. The lowermost red line shows the radiance contribution from OCS to this total radiance. The MIPAS nominal measurement altitudes are shown as pale horizontal lines (left axis).

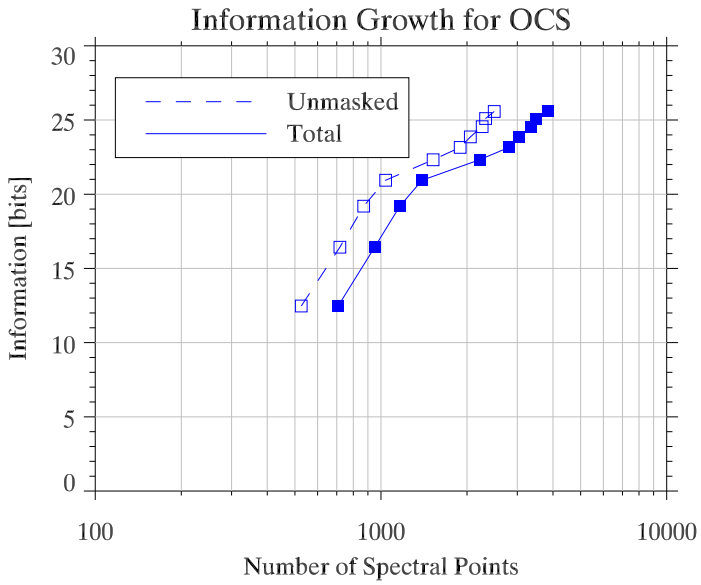

Figure 4.4: The information gain is plotted against the number of points required, on a logarithmic scale. As the number of spectral points contained in the set of microwindows increases, so does the total information retrieved on the target species. This is limited by the width of the spectral feature. For OCS a set of ten microwindows was chosen, giving a theoretical maximum of 25 bits, shown here. In general there is no clear optimal number of points, the limiting factor is computational resources. Making the assumption that all altitudes and the whole band of OCS (60 cm^{-1} wide) are used, the total number of points is approximately 20,000. Extrapolating from the plot, this corresponds to an estimated absolute maximum of 37 bits of information, based on the 100% initial estimated uncertainty.

4.2.1 Microwindow Selection

The chosen microwindows are shown in Figure 4.3 and their details listed in Table 4.1. The selection tool, MWMAKE, was run with a constant OCS profile that is both latitudinally and seasonally invariant. Pressure, temperature and other major species were given reasonable physical ranges and uncertainties that for simplicity were also invariant during the selection procedure. The operational MWs were an optimised trade off between number of spectral points (computing resources required) and information gain (bits). However, the much lower signal strength of OCS required as many MWs as possible and the selection cutoff was determined by an information gain per MW of

less than 1 bit. The selection procedure has been described in more detail in Section 2.2 and in a generalised manner by Dudhia et al. (2002a). The number of bits gained for an increasing number of MWs against the number of spectral points used is shown in Figure 4.4. By considering the climatological (1-σ) uncertainty and the number of retrieved levels, the net gain in information from performing a retrieval on simulated data is approximately 25 bits (Figure 4.4), or 10 bits from a full retrieval with realistic noise and fewer levels. This is as expected from Equation 2.15, which shows how the information content is a function of the prior and retrieval covariances, where the latter contains a random error term.

Table 4.1: The ten best carbonyl sulphide microwindows.

Microwindow	Band	Spectral Range (cm^{-1})	Altitude Range (km)
OCS_0101	D	2050.650 – 2053.575	6 – 52
OCS_0102	D	2034.275 – 2036.925	6 – 18
OCS_0103	D	2054.425 – 2057.425	6 – 18
OCS_0104	D	2043.975 – 2046.325	6 – 21
OCS_0105	D	2047.625 – 2050.625	6 – 68
OCS_0106	D	2057.450 – 2059.875	6 – 52
OCS_0107	D	2037.475 – 2040.025	6 – 21
OCS_0108	D	2066.025 – 2068.800	6 – 24
OCS_0109	D	2042.475 – 2043.900	6 – 21
OCS_0110	D	2069.150 – 2072.150	6 – 24

4.2.2 Errors

The errors propagated through MW selection allow us to determine the dominant terms, as shown in Figure 4.5. This highlights the sensitivity of our retrieval to parameters other than our target species. There are three areas of consideration:

Firstly, systematic errors. These were discussed in Chapter 2 as part of the microwindow selection theory section. Systematics include terms such as radiometric

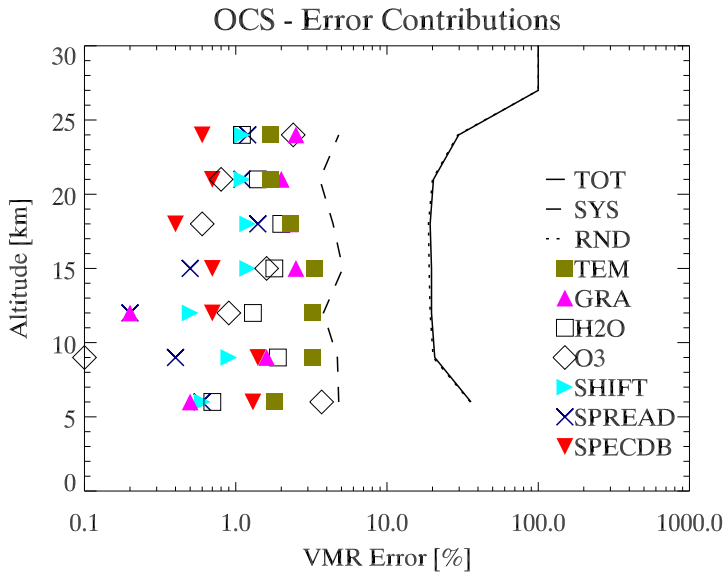

Figure 4.5: Assignment of various error sources to the final error budget as calculated during microwindow selection. The total error is shown (solid line) together with the random error component (dotted line) based on the instrument NESR. The total of the systematic error contributions is also shown (dashed line). The full list of possible error terms was given in Chapter 2. It is also worth noting that non-LTE (local thermodynamic equilibrium) effects do not appear, which is unusual for short wavelengths, but no non-LTE model for OCS is available.

calibration and the incorrectly known (and modelled) concentrations of other 'interfering' species whose emission region overlaps that of the target species.

Secondly, the random errors. This is the dominant error term (the dotted line) for a MW selection based on retrieving a single profile. Fortunately, we can combine measurements to reduce this error term. The necessary considerations were discussed in Chapter 3 and results of coaddition as applied specifically to OCS are discussed later in this chapter. In addition, it is also possible to include the pressure and temperature retrieval errors as random instead of systematic.

And finally, the spectral accuracy. The 'SPECDB' term, also a systematic error, is cause for concern because it is only an estimate of the overall uncertainty in the line parameters. Its contribution to the MW validation from simulated data (Section 4.3) is

zero, so it is difficult to quantify its effect on the result. In addition, it is hard to assess the accuracy of the error estimate, relying on often incomplete HITRAN parameters. A summary of spectrocopic parameters for the MIPAS mission was performed by Flaud (2003) and a more general discussion may be found in Flaud et al. (2003). The OCS IR data included in the commonly used HITRAN2K (HITRAN, 2003) spectral database is based on a consistent set of calculations and observations. As a result, for the fundamental ν_1 and ν_3 bands, an absolute accuracy of 3 – 5% was expected. Unfortunately, more recent work has cast serious doubt on the quality of the line intensities, estimating that the ν_3 line intensities may be too low by about 12.4%, Regalia-Jarlot et al. (2002). The MIPAS spectral database, based on an older version of HITRAN, was updated in 2003 to be an average of the HITRAN2K values and this recent work. This corresponds to multiplying the HITRAN2K values by 1.13 for the ν_3 band, giving an estimated accuracy of 5 – 8%. It is difficult to assess the accuracy of other parameters, such as air broadening and temperature dependence as these figures have no references within the HITRAN database.

It is also worth nothing that if the uncertainty is purely a line strength error then it converts to a simple scaling factor in the retrieved VMR, with no other consequences for the retrieval. This is in contrast to the line width and position errors.

4.3 Microwindow Sensitivity

The aim of this internal validation section is to show that the selected MWs have good sensitivity to the target species by using a carefully controlled simulated environment. The RFM was used to simulate a set of 17 spectra corresponding to the MIPAS sampling intervals for a benign mid latitude day atmosphere. Nominal climatological profiles were used for all species in the first instance, and the retrieval and simulation

parameters were chosen to be as similar as possible. Then, variations in these parameters were made to assess the sensitivity of the retrieval and microwindows towards perturbation. The only retrieved parameter in all cases was OCS, along with continuum and offset terms. All others were set in the retrieval to match the simulation.

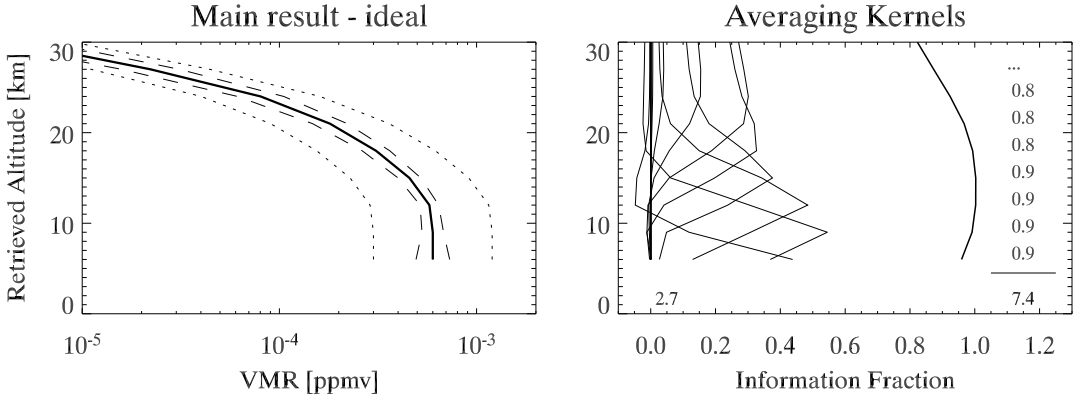

Figure 4.6: Idealised retrieval from simulated data for OCS. This is the ideal case where the initial forward model parameters most closely resemble the retrieval parameters and the a priori and initial guess were set to the 'true' simulated value. The a priori uncertainty was set to 100%. Diagnostic information, including the averaging kernels, is shown on the right. The degrees of freedom in this profile, of nine levels considered, are shown on the bottom left, the Shannon information gain for this retrieval is shown bottom right, with a level by level breakdown above. The χ^2 vlues for this retrieval were all below 1. There is no significant prior information contribution until above 25 km and it does not reach 50% until 33 km (random error greater than 72% or information fraction below 0.5). The information fraction is defined as the contribution of any level to the final retrieval at that level, with the solid rightmost line showing the totals (which should be close to 1 for an ideal retrieval with no residual a priori information).

4.3.1 The Ideal Case

The resulting retrieved profile and its associated averaging kernel for this ideal case are shown in Figure 4.6. Although no random noise was added, a nominal value of 3.5 nW/(cm^2 sr cm^{-1}) was assigned to the spectra so the resulting diagnostics were realistic. The averaging kernels for this retrieval are also shown and the vertical width of these kernels is a measure of retrieval resolution.

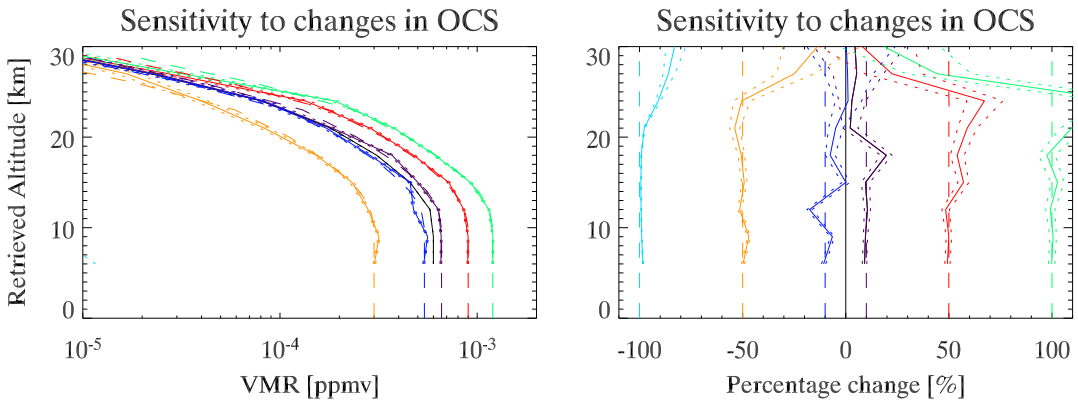

Figure 4.7: Sensitivity of the OCS microwindows to changes in simulated VMR. [Left] Profile deviations, ppmv. [Right] Percentage deviations. The deviations from the 'true' RFM modelled VMR values are indicated by the dashed lines. The same retrieval parameters were used throughout, with the same a priori and an initial uncertainty of 100%. The pale blue curve is outside the leftmost plot range as it corresponds to a profile of zero ppmv.

4.3.2 Variable OCS

A similar approach was used to determine the sensitivity to OCS variability. Figure 4.7 shows the result for the same retrieval parameters, a priori etc. used on a set of differing simulated atmospheres. A set of six profiles were used: no OCS, −50%, −10%, +10%, +50% and +100% of the climatological profile. The results show the sensitivity of the microwindows to changes in the amount of OCS in the atmosphere. As one would expect from looking at the averaging kernels in the previous figure, there is good sensitivity at low altitude, but by 30 km the a priori becomes the dominant contribution to the final retrieved state.

4.3.3 External Validation

An alternative 'blind test' dataset was obtained as part of work performed for the AMIL2DA project, (AMIL2DA, 2003). These files underwent the standard retrieval scheme, as applied to operational data, and the resultant profiles compared with the profile information initially used to create the simulated spectra but kept unknown to

the retrieval code. The comparison showed good convergence to the desired result.

4.3.4 Simulated Noise on the Measurements

The random noise must be added to the spectra synthetically, of a magnitude corresponding to that of the instrument channel. However, due to the processing performed between observation of an interferogram and the level 1B spectra, the noise must contain a degree of correlation. This is most easily achieved by forming a unit normalised noise vector with a Gaussian distribution about zero. This is Fourier transformed in line with the instrument processing, apodised (Norton-Beer strong) and then Fourier transformed again. After linear scaling by the appropriate noise value, 3.5 nW/(cm^2 sr cm^{-1}) in the case of OCS, the correlated noise vector is added to the simulated spectra. The results of retrieving from these noisy spectra are as would be expected. The noisy retrieved profiles are generally within the error bound of the ideal case, even though each individual profile contains some variability.

4.4 Initial Retrievals

The OCS MW error analysis in Figure 4.5 highlighted the key interfering species (water and ozone) that must be retrieved prior to OCS in order to improve the overall error. A mid-latitude day atmospheric scan, free of cloud (using a ratio threshold of 1.8) to 6 km was chosen based on its geolocation. The exact scan (arbitrarily) chosen was from August 2003, orbit number 07469 scan number 15. Pressure, temperature, water vapour and ozone were retrieved in sequence using MORSE with the default operational ESA initial guess atmosphere for the appropriate latitude band. Finally, OCS was retrieved using its nominal climatology as both the initial guess and the a priori, with an uncertainty of 100%, in line with the MW selection parameters. The result is

shown in Figure 4.8 and for these good observing conditions gives a retrieval in line with expectations based on the previous simulations. The retrieval diagnostics are also shown as before. These diagnostics are influenced by the temperature, OCS VMR and measurement NESR, so show some variability.

The same retrieval parameters, with an initial guess for the major species that changes for each of six latitude bands (90–65°, 65–20°, 20–0°) gives rise to a whole orbit retrieval shown in Figure 4.9. This latitudinally variable Initial Guess (IG) for contaminant species is in line with the operational MIPAS retrieval procedure. The OCS initial guess is constant with latitude and the development of smooth latitudinal structure is a good indicator of sensitivity to small changes in OCS. This appearance of latitudinal structure is also a useful piece of internal validation, especially as the structure is uncorrelated with the latitude bands where the IGs change. An additional test was performed using invariant contaminant IGs, and the observed OCS structure remained (see later discussion about the carbon monoxide bias).

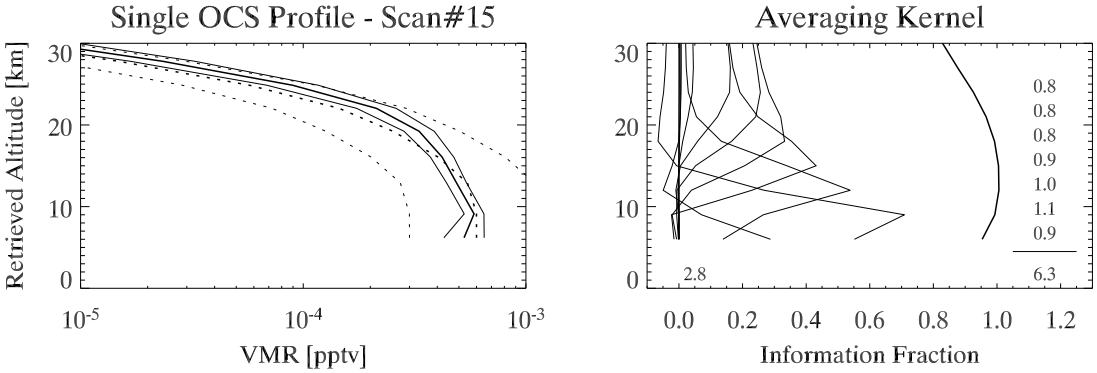

Figure 4.8: Results of retrieving, in sequence, pressure and temperature followed by water vapour, ozone and finally OCS from a single scan in orbit 07469 taken during August 2003. The layout is the same as Figure 4.6. At 6 km, an overestimate of continuum or very thin cloud not detected by the cloud threshold give rise to a lower VMR and AK contribution. In effect, the continuum retrieval term absorbs a small fraction of the radiance associated with the OCS. The drop in VMR would not generally be expected in the well mixed free troposphere.

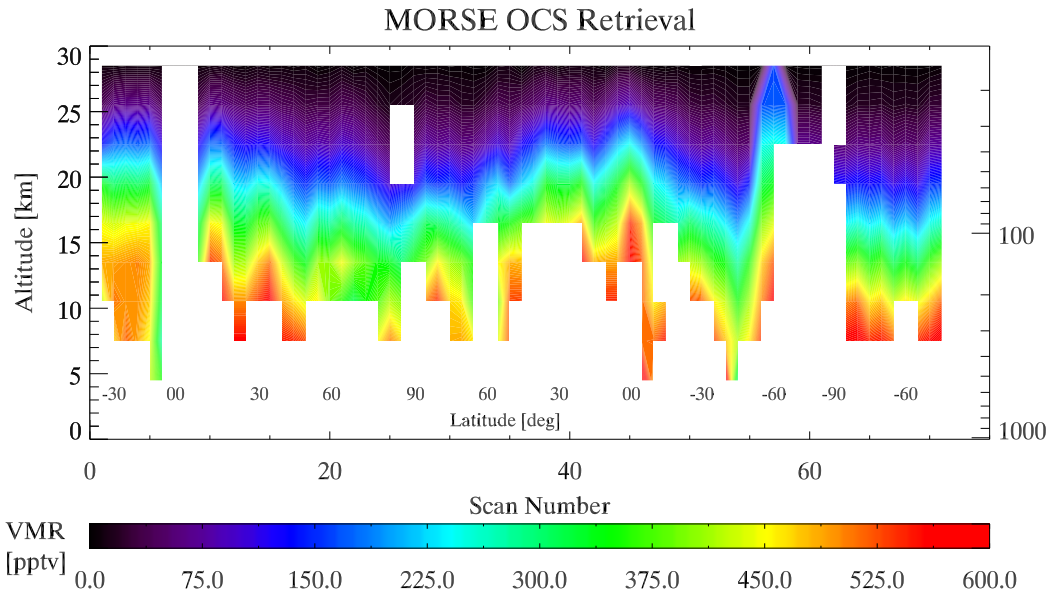

Figure 4.9: Plot of OCS for the remainder of orbit 07469 in August 2003, using the same method as the profile retrieval in Figure 4.8. Correlation length was 3 km and the cloud ratio threshold was set to 1.8.

4.4.1 Validation Against Other MIPAS Retrievals

Complementary work performed by Alpaslan (2004) in response to our initial OCS feasibility study enables an independent validation of the MIPAS OCS retrievals. The Istituto Fisica Applicata Carrara (IFAC) group makes use of an independent time-optimised retrieval code that is the precursor to the operational ESA processor, Ridolfi et al. (2000). This is known as the 'Optimised Retrieval Model' (ORM). For their study, a series of 'meso-windows' were manually selected in the ranges 860–870 cm^{-1} (middle of band 'A') and 2040–2070 cm^{-1} (band 'D'). A basic retrieval was performed for the MIPAS Quality Working Group 'reference' orbit 2081 (July 2002). The results of this study are compared with our own results for the same orbit in Figure 4.10. The main discrepancies, as expected, are in regions of thin cloud and at high altitude.

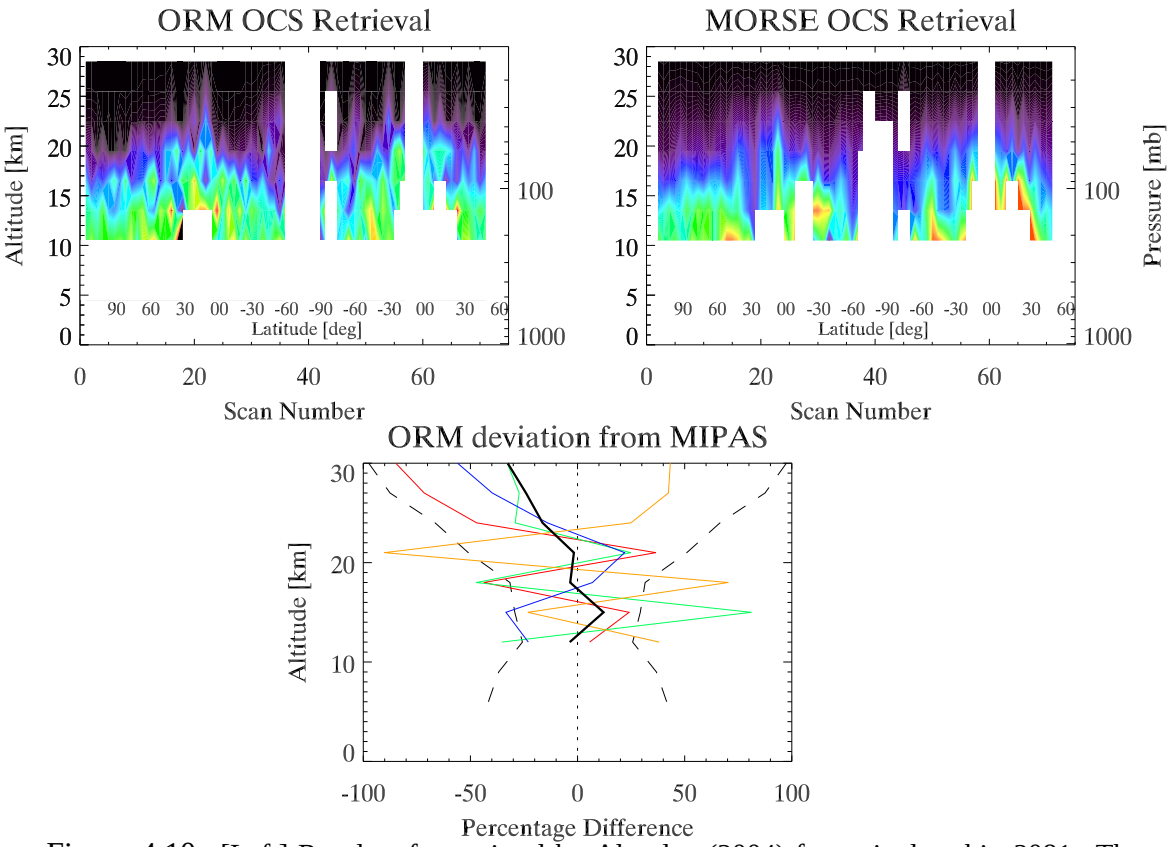

Figure 4.10: [Left] Results of a retrieval by Alpaslan (2004) for a single orbit, 2081. The ORM retrieval scheme uses no prior information. In addition, the microwindows were selected by hand and make use of both 'A' and 'D' spectral regions. [Right] Result from using MORSE on the same dataset, with the microwindows described at the beginning of this chapter. The colour scale is the same as the previous figure. [Bottom] Percentage difference between the two methods (ORM-OPTIMO) for scans 1, 15, 30, 45 (coloured lines) and their mean (black). The random error bounds are shown by the dashed lines. The ORM retrievals seem to be lower than the OPTIMO method at higher altitudes. However, this effect is well within the random error bar.

4.4.2 Envisat Validation Campaigns

Ideally some of the targeted Envisat validation campaigns would have measured OCS in-situ simultaneously with MIPAS. OCS is very much an 'experimental' species – it was not really expected to be successfully retrieved, and unfortunately no time and space coincident data are available. As previously mentioned, there is also a general lack of prior real-world measurements of OCS profile information, especially with

good spatial distribution. However, point profile measurements exist, and provide the opportunity for validation of the retrieval. It is possible to make use of previous measurements by taking advantage of the negligible reported OCS trend and comparing profiles for similar conditions and seasons. Care must be taken with this approach, and the results are not as definitive as targeted in-situ measurements.

4.4.3 Multiple Orbits

A useful external validation of the results can be performed for retrievals over the latitude range for which in-situ measurements, discussed in the introduction to this chapter, have been made. Figure 4.11 shows a comparison of 135 MIPAS scans from mid latitudes against similarly geolocated balloon data as summarised by Chin and Davis (1995). There is good general agreement between the two profiles, and little evidence of a significant annual trend. This is in line with literature expectation (Rinsland et al., 2002). For example, the 1996 mid latitude tropospheric mean around 9 km was 510 pptv and the mean tropospheric value of the data shown in the figure is 522 pptv, excluding systematic biases. The trends or variability in OCS over the duration of the MIPAS mission — both from month to month and from week to week — as well as the small hemispheric difference suggested in the introduction will be discussed later in this chapter. Importantly, however, the range of measurements from MIPAS extends above the majority of balloon altitudes. Even this initial MIPAS data set constrains the shape of the mid stratospheric OCS profile whereas previously this part of the profile was extrapolated from the 20 km region. The nature of the fall-off in OCS with altitude is important in constraining the stratospheric sinks and lifetime for the species. Tropospheric measurements are useful for constraining the location and balance of sources and sinks.

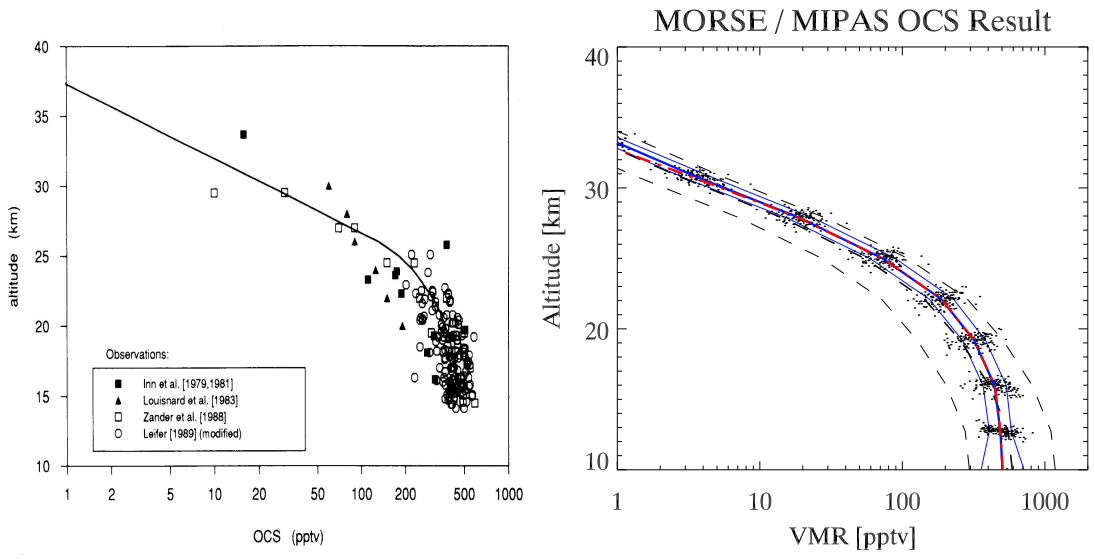

Figure 4.11: [Left] Collated balloon data from Chin and Davis (1995). [Right] A scatter plot showing the a priori and its uncertainty (dashed lines) together with the logarithmic mean and standard deviation (blue lines) of 135 retrieved profiles from August 2003. The scattered points show the individual cloud free profiles in the restricted latitude range 35° to 45° N and -30° to 30° W, giving a representative mid latitude atmosphere. Although the two figures are difficult to compare, the key points are the significantly lower MIPAS VMRs above 30 km, whereas both the tropospheric values and the scatter are very similar. The red line shows the small effect of detrending the mean profile to remove cumulative a priori influence, discussed in Section 4.4.5.

4.4.4 Confidence

Figure 4.8 showed an increasing standard deviation (uncertainty) in the results with altitude. This is expected because the absolute amount of OCS is greatly reduced as a combination of decreasing pressure and a decreasing proportion (ppmv) relative to air. As a result, the contribution to the observed radiance is much lower and around 30 km it drops below the noise 'floor' of the instrument. Below this altitude, the random error is very significant as shown in the microwindow error analysis in Figure 4.5, and this maps directly into the retrieval uncertainty.

For an isolated retrieval, an individual level is generally only useful if 50% or more of the final value originates from the measurement (the remainder is the a priori). This

corresponds to a random error of about 72%, and this ‘cut-off’ occurs just above 30 km in the case of OCS for a good individual profile.

4.4.5 A Priori Detrending

As discussed in Chapter 3, the addition of profiles obtained by the optimal estimation approach will contain a bias from the prior information, the significance of which increases as more profiles are combined. As the retrieved OCS profiles are close to the a priori, the first order correction outlined in Equation 3.39 can be applied. Removal of the a priori results in similar behaviour to a least squares retrieval. As there is no strong constraint on our system, individual profiles are prone to instabilities and strong oscillations when the least squares approach is used. For this reason, the prior information is removed after the mean profile has been calculated. The result of this approach was shown along with the unprocessed result in Figure 4.11. The correction is very small, even above 25 km. However, by 30 km — even though the correction remains small — the information contribution from MIPAS is small. As a result, even though the a priori is removed, the result will tend to remain unchanged if it contained little measurement information in the first place. A possible high bias was observed against the ORM results shown previously, which do not use an a priori (Figure 4.10). However, both these MIPAS retrievals point to a lower OCS value at 30 km than has previously been estimated though extrapolation from balloon measurements.

4.5 Global Retrievals

As the limiting factor in our retrievals is the random noise, it makes sense to attempt to reduce this by coaddition in order to improve the signal-to-noise and therefore the precision of our answer. The trade-off between precision and coverage is easier to

make in the case of MIPAS due to the large number of measurements (72 by 14 by 30, or about 30,000 scans per month). There will be a loss in the fine structure that can be resolved.

The month of August 2003 was initially chosen due to early presence of a good availability of recalibrated level 1B data, although a significant number of the 30,000 profiles were missing. In addition, it contains the 'worst case' atmosphere — the end of the Southern winter with highly perturbed chemistry and extreme temperatures. The same approach as in the previous section was used, performing a prior pressure, temperature and interfering species retrieval. The same set of retrieval parameters, such as climatological OCS profile, a priori uncertainty (100%) and correlation length (3 km) were used throughout. The only variations between profiles should originate from the variability between radiance spectra themselves. After the identification and removal of anomalous profiles, identified by unphysical values ($\pm$1000 times the a priori) and excessive oscillation between multiple levels about 15,000 geolocated OCS profiles remained. Each profile has 11 levels, possibly containing 'cloud masks' and covering the altitude range from 6 to above 30 km. The cloud masking is required to prevent un-retrieved levels from biasing the mean result towards the a priori — in effect it removes these levels from consideration in all further processing. The points are then 'binned' to a regular latitude, longitude and altitude grid. Statistical parameters, such as the standard deviation of profile levels within each grid box are also recorded before the logarithmic mean is taken to reach a mean VMR value for each element. Other constraints, such as a maximum random error on a profile point, can also be applied before the mean is taken.

A type of probability density function (PDF) is shown in Figure 4.12 showing the range of retrieved VMR values at each level, after the constraints and filters discussed above are applied.

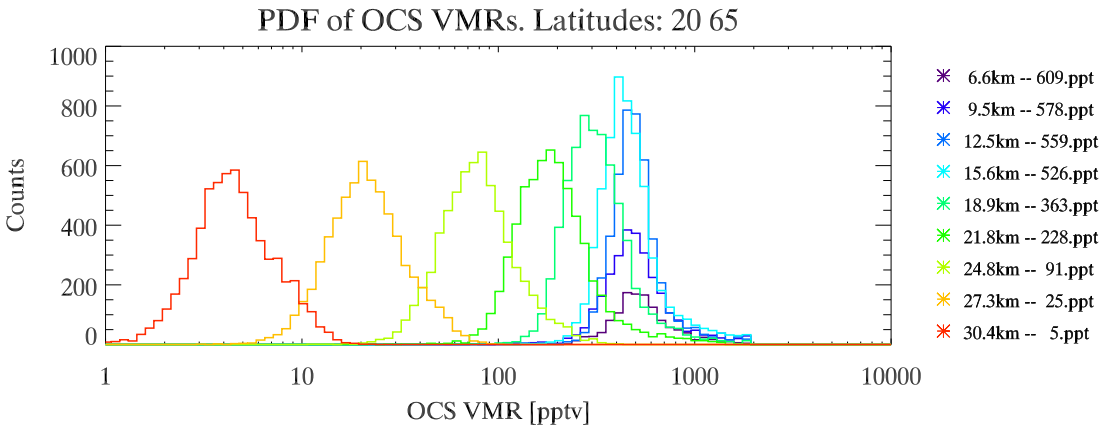

Figure 4.12: Distribution of retrieved VMRs after removal of spurious values, showing that no distortions have been introduced in the underlying statistics. In addition, it highlights the large number of lowermost levels that are lost due to cloud (area under the curves). The width of the individual distributions is a measure of their standard deviation, directly attributable to random error.

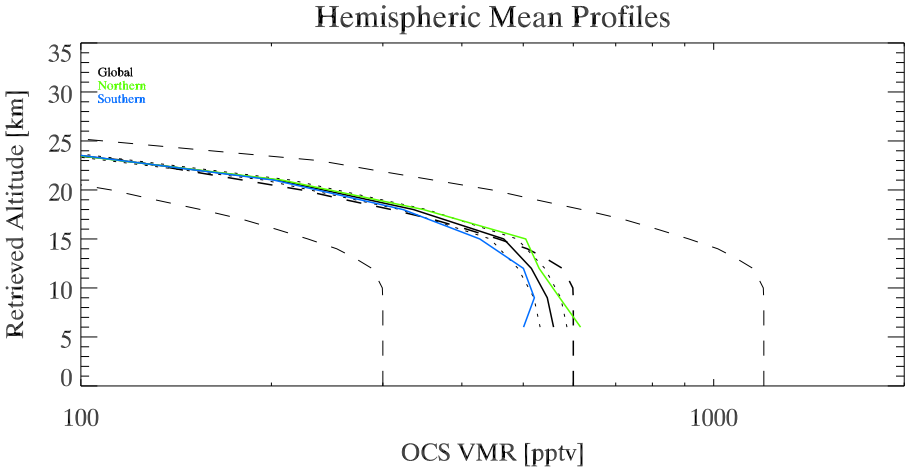

Figure 4.13: This figure shows the global mean profile for August 2003 (black line, uncertainty as dotted lines) and the hemispheric means (NH: green line, SH: blue line). The a priori and its uncertainty are shown by the dashed lines. There is a small hemispheric difference in the troposphere. The overall shape of the global mean agrees well with the climatology (dashed black line).

4.5.1 Hemispheric Mean Profiles

Figure 4.13 shows the mean global and hemispheric retrieved profile data from August 2003. There is little expected variability between the hemispheres, although the

Northern hemisphere should be slightly higher due to anthropogenic sources. This is what is observed. The carbon monoxide bias discussed in the next section has been corrected in this figure.

4.5.2 Zonal Means

The result of binning the results to an altitude/latitude grid and taking the logarithmic mean is shown in Figure 4.14 and the associated retrieved temperature structure in Figure 4.15. The OCS field shows a good degree of smoothness implying internal consistency between profiles. In addition, there is the appearance of latitudinal structure from a featureless a priori. A seasonal asymmetry about the equator is visible, associated with the underlying atmospheric structure. There initially appeared to be problems from 65°S to the pole, with values seeming unreasonably large at lower altitudes. It was suggested that this could be the effect of thin Polar Stratospheric Clouds (PSCs) that do not trigger the operational cloud threshold ratio value of 1.8, but there was no obvious correlation to be found between cloud index and VMR in the Antarctic region. The positioning of the start of the anomalous values at 65°S seems to coincide with one of the latitudes at which the initial guess files change. Figure 4.16 shows the result of the same retrieval procedure as before, but with the carbon monoxide (CO) IG invariant for all latitudes. On further inspection, the Southern polar winter CO initial guess contained a clear error, with a sharp spike in the profile around 12 km. The result is much improved, and the temperature field as well as the standard deviation of this second result are also shown.

Observed Features

The high OCS VMRs around the tropical tropopause has been previously reported by Notholt et al. (2003), although the high variability, shown by the areas of high standard

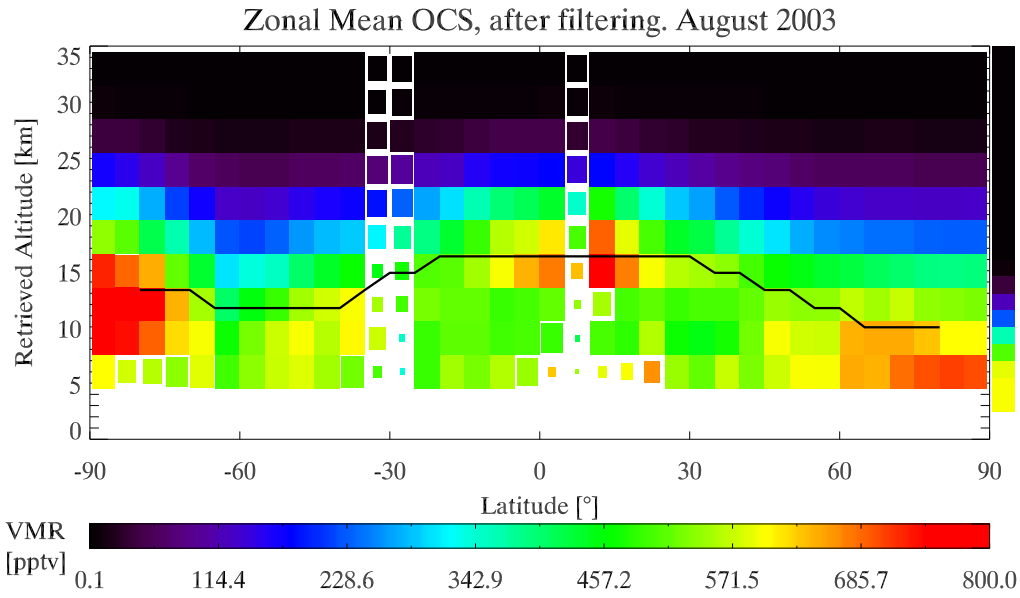

Figure 4.14: OCS zonal mean for August 2003. The data was gridded to a 5° latitude by 3 km altitude grid. The black line shows an approximate climatological tropopause. The incompletely filled 'boxes' represent a shortage of data (less than 100 points). The high values around the South pole are from an unrealistic CO profile in the initial guess.

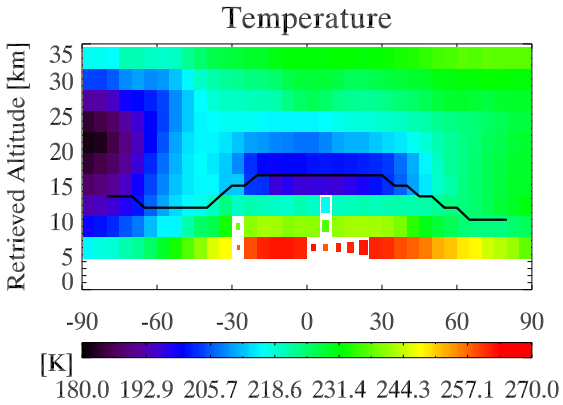

Figure 4.15: The retrieved MIPAS temperature field for August 2003, showing expected seasonal structure.

deviation, is new to this work. Their explanation was based on biomass burning and deep convection and one of their figures is reproduced in Figure 4.17 for comparison. However, simulations of the sensitivity of MIPAS to fine atmospheric structure indicates that there is a susceptibility in the tropical tropopause region to oscillation. If

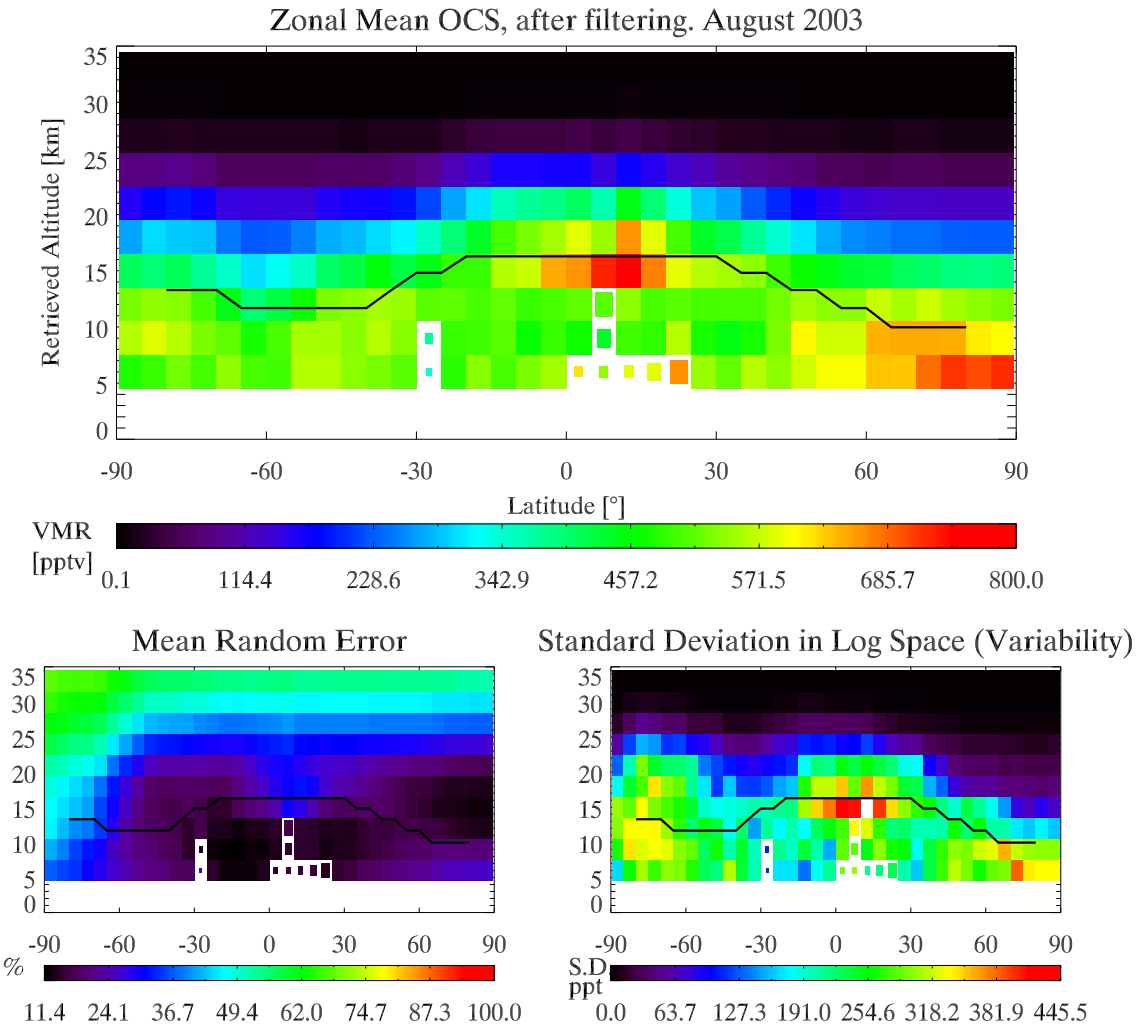

Figure 4.16: [Top] OCS zonal mean for August 2003, plotted in the same manner as the previous figure. A global mean value for CO was used as a contaminant in this retrieval. [Bottom] The random error field outlining the areas of highest and lowest confidence in the retrieval, and the standard deviation of the retrieval in log space showing areas of high and low variability. The areas of highest variability are the tropical tropopause, Southern polar winter night and some of the 6 km level that probably retains residual thin cloud contamination.

subsequently damped by the rapid falloff in VMR with altitude, this would be interpreted as a localised enhancement in the absence of any variability in the underlying chemical profiles. The explanations are not mutually exclusive, but this observation is an example of remote sensing problems.

The enhancement over the Southern winter pole remains, to a much smaller extent,

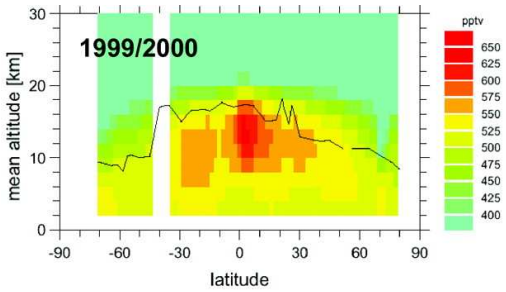

Figure 4.17: External validation from data published by (Notholt et al., 2003) to be compared against the observed zonal mean shown previously in Figure 4.16. In this plot, tropical enhancement is observed by a combination of ship and satellite (ATMOS) measurements. The authors assign it to deep convective events transporting biomass burning products to high tropospheric altitudes.

after the CO bias has been removed. Kettle et al. (2002a) discusses the hydroxyl radical OCS loss rate, and this — together with the UV flux — is virtually zero at the winter pole, allowing tropospheric-type values to be found up to 15 km.

Internal Validation

There are two simple internal validations to test for consistency. The first is consistency between weeks. One would only expect a weak difference between the two halves of the month, mainly due to the rapid change occurring around the Southern Polar regions at the beginning of its spring. The second is to split the data by solar zenith angle, and examine the diurnal variability. This should also give a negligible difference. The OCS loss mechanisms in the stratosphere are weighted towards the daytime, but OCS has a long stratospheric lifetime and so should exhibit little diurnal change. The biogenic source and sink variability over the daily cycle should be well damped by mixing by the 6 km altitude level and should also be virtually undetectable. The results of these tests are shown in Figure 4.18. The diurnal variability test is especially important as non-LTE effects in the D-band are much larger for the shorter wavelengths. This was potentially a large source of error, as there was no non-LTE model for OCS in the

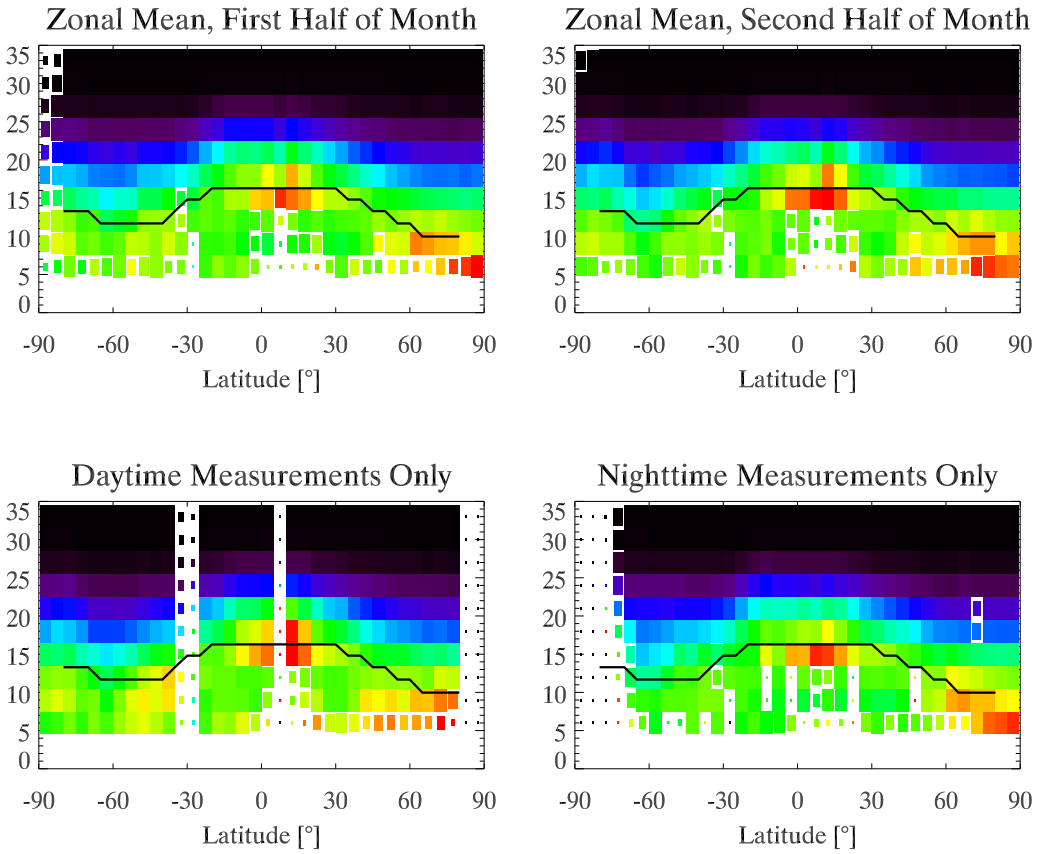

Figure 4.18: Diurnal and monthly variability as internal validation. The colour scale is the same as Figure 4.16. It is interesting to note the decrease in magnitude of the tropical tropopause error (high values) at night-time. This is probably caused by a less severe temperature gradient at night in this region. There is also a limited low altitude (at 6 km only) diurnal difference for the Northern mid latitudes, probably caused by very thin cloud. Convection is strongly diurnal and the propagation from the source in the planetary boundary layer is likely to reach the tropical tropopause by this diurnally asymmetric method.

forward model. These results indicate for the first time that non-LTE is much less significant for OCS than for the other D-band species, CO and NO. However, there is still some diurnal variability, especially over the tropical tropopause, but this can equally be assigned to very thin cloud arising from strong convection. There is insufficient OCS to draw any conclusions about non-LTE effect in the upper stratosphere.

External Validation

There are the usual possibilities of validation (or at least comparison) against a model (Section 4.6.1) and of validation against in-situ measurements. Due to scarcity of external correlative data, the only real measurements for comparison are of mid latitudes, as already shown. Validating the lowermost levels against point OCS measurements in the literature is possible with the greater global coverage from the enlarged dataset. Comparing measurements of the lower atmosphere, with published data from both hemispheres (Notholt et al., 2003) with similarly geolocated MIPAS measurements gave good agreement

Direct comparison with $CFCl_3$ and CF_2Cl_2 profile data has been suggested by Engel and Schmidt (1994), but our knowledge of OCS from MIPAS is more accurate than the variability in the measurements of these species. As an alternative, a plot of OCS against the operationally retrieved age proxy N_2O is shown in Figure 4.19. This highlights the significant loss term in the stratosphere (curvature of the plot). Independently, Rinsland et al. (2005), shows tight linear correlations between the various CFCs (lifetime of order 100 years) and N_2O, justifying our use of N_2O here. Additionally, in the next chapter the same ESA operational N_2O retrievals are favourably compared with the (almost) ideal age proxy, SF_6.

4.5.3 Global Means

If the longitude information is also considered, then a three-dimensional global field of OCS VMR distribution for August 2003 can be constructed. Obviously, the number of elements per box (and hence the reduction in the random error) is reduced, but due to the immense number of profiles and excellent geographic coverage there remain 50 – 100 measurements in most boxes. A representation of the results is shown in

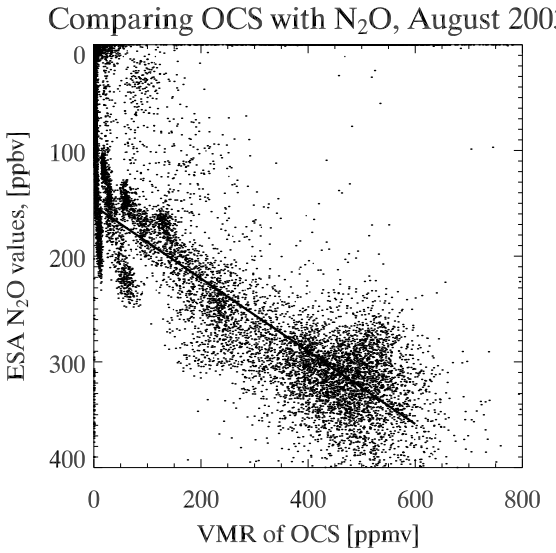

Figure 4.19: A plot of OCS against the operationally retrieved age proxy N_2O. The deviation from a straight line is indicative of the differences in loss rate between N_2O and OCS in stratosphere. The absolute falloff is related to the OCS stratospheric lifetime.

Figure 4.20. This single set of results alone massively improves the knowledge of the abundance and distribution of OCS, especially in remote areas. This global coverage is the advantage of satellite remote sensing.

4.5.4 Cloud Coverage and Contamination

There are several localised features of interest in Figure 4.20. The inter-tropical convergence zone (ITZ), an area of very strong ascent, can be seen over the Indonesian region as an area of poor coverage, for example the 12 and 15 km levels. This is directly attributable to cloud formed by the ascent obscuring the lower layers. Figure 4.21 shows the August monthly mean cloud coverage over the globe from a model. The figure highlights good correlation with the poorly covered areas of the lowermost altitudes in Figure 4.20. Above these cloudy areas, especially Indonesia, there are regions of enhanced OCS, thought to be indicative of strong ascent, in agreement with recent literature observations, Notholt et al. (2003). In addition, the enhancements may

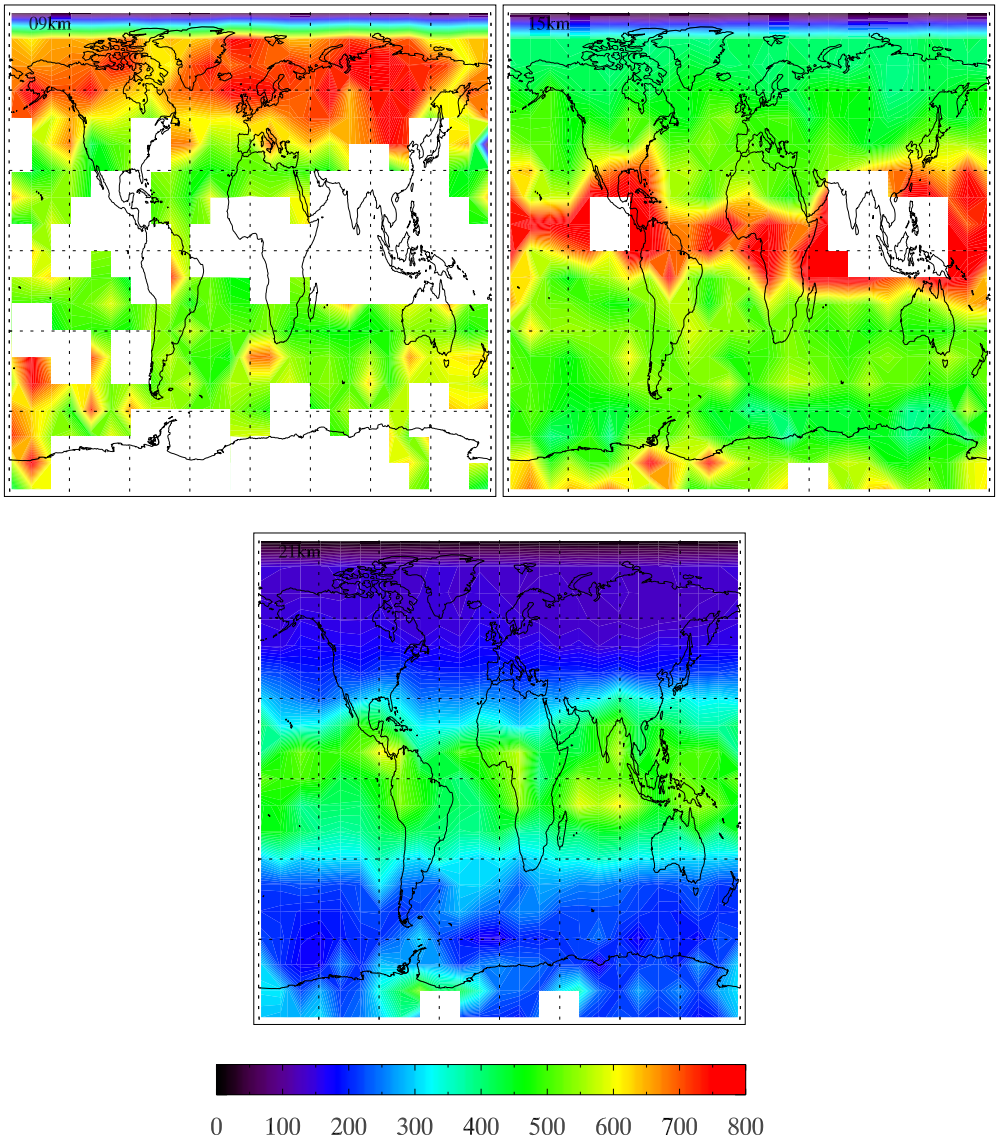

Figure 4.20: Some of the retrieved altitude layers for OCS showing VMR as a function of geolocation. The colour scale is the same as Figure 4.16. The top left box highlights the poor coverage at 9 km, mainly due to cloud in the tropics and low temperatuers giving rise to high random errors at low altitude over the Antarctic. This is followed by samples at 15 and 21 km from the retrieved volume, giving an indication of the global 3D nature of the monthly mean field.

be direct observations of biomass burning plumes, and this would be an interesting area for further investigation.

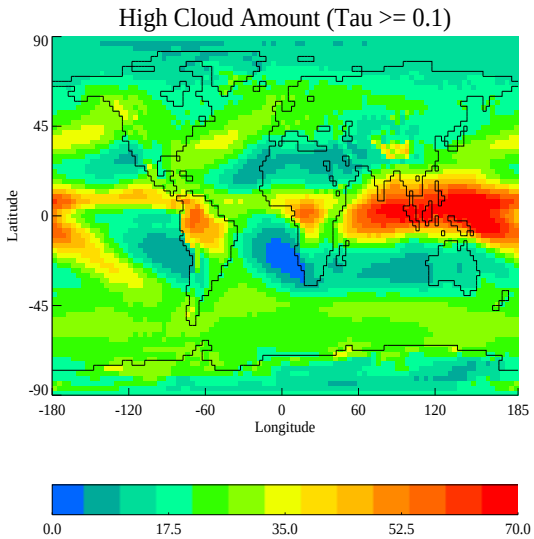

Figure 4.21: Model cloud fraction for August 2003, Dean et al. (2005). The regions of high cloud coverage, up to 70%, correlate very well with MIPAS observations of cloud. The cloud in the MIPAS observations prevents successful retrieval and leads to areas – especially at low altitudes in the tropics – where there is very poor coverage and high variability in the few retrievals that are 'successful'. The large amount of cloud highlights the need for improvements in the way that cloud is handled in limb retrievals, so it is possible to obtain some form of retrieval even from a cloud contaminated spectrum.

4.5.5 Lifetime and Mass budgets

As noted in Figure 4.13, the lower OCS VMR observed by MIPAS in the middle stratosphere (25 – 35 km) is significant for determining the stratospheric lifetime of OCS.

The average stratospheric VMR, χ_{s}, is given by

$$\chi_{\mathrm{s}} = \frac{\sum_z \chi_{\mathrm{s}}(z) M(z) \Delta z}{\sum_z M(z) \Delta z} \tag{4.1}$$

where $M(z)$ is the number density (in molecules cm^{-3}) at vertical ordinate z that ranges over the stratosphere. A similar expression applies for the troposphere. This value can be easily calculated from the zonal mean fields of pressure, temperature and VMR. It is also possible to retain sensitivity to latitude, which has previously been

impossible from the limited set of measurements.

From this average VMR, the total mass of OCS in the atmosphere, W^{OCS}, is given by

$$W^{\mathrm{OCS}} = \left(\frac{W_{\mathrm{t}}^{\mathrm{air}} \chi_{\mathrm{t}}}{\mathrm{RMM}^{\mathrm{air}}} + \frac{W_{\mathrm{s}}^{\mathrm{air}} \chi_{\mathrm{s}}}{\mathrm{RMM}^{\mathrm{air}}} \right) \mathrm{RMM}^{\mathrm{OCS}} \tag{4.2}$$

which can be broken into tropospheric ($W_{\mathrm{t}}^{\mathrm{OCS}}$) and stratospheric values ($W_{\mathrm{s}}^{\mathrm{OCS}}$). The mean Relative Molecular Mass (RMM) of air is 28.9 g mol^{-1} and that of OCS is 60 g mol^{-1}. Appropriate masses of air for the troposphere ($W_{\mathrm{t}}^{\mathrm{air}}$) and stratosphere are 4.56×10^{21} g and 7.20×10^{20} g respectively. The results of these calculations are shown in Table 4.2

Table 4.2: Global mean mixing ratios and masses of OCS for August 2003.

		MIPAS August 2003	Chin and Davis (1995)
Mean Global VMR (χ)	pptv	499±74	(485)
Mean Stratospheric VMR	pptv	353±81	380
Mean Tropospheric VMR	pptv	522±78	500
Total mass (W^{OCS})	Tg	5.47±0.75	5.20
Stratospheric mass	Tg	0.52±0.12	0.57
Tropospheric mass	Tg	4.94±0.74	4.63

There are a selection of global source estimates for OCS at the surface that range between 1–2 Tg yr^{-1}. As no significant trend in OCS has been reported, it is reasonable to assume that the source term is balanced by sink terms. For example, Watts (2000) gives a source term of 1.31±0.25 Tg yr^{-1} and a sink term of 1.66±0.79 Tg yr^{-1}. Therefore, dividing the total atmospheric mass of OCS obtained above by the source strength gives an estimate for the global atmospheric lifetime of OCS of 4.17±0.24 years. This is comparable with other estimates, such as 4.3 years by Chin and Davis (1995), based on a source estimate of 1.2±0.5 Tg yr^{-1}.

Following the method of Chin and Davis (1995), the loss rate of OCS in the stratosphere due to photochemical processing can be calculated from the mean stratospheric VMR. The thermodynamic end point of these reactions is sulphur dioxide. The stratospheric loss rate of OCS at an altitude z, $L(z)$, in molecules cm^{-3} yr^{-1} may be written as,

$$L(z) = (J_1(z) + k_2(z)[\mathrm{O}(^3\mathrm{P})](z) + k_3(z)[\mathrm{OH}](z))M(z) \tag{4.3}$$

J_1 is the photo-dissociation rate and k_2 and k_3 are the first order rate constants for the reactions of OCS with oxygen and hydroxyl radicals respectively. The concentrations of these species, denoted by the square brackets, also have a latitudinal variability. Although beyond the scope of this thesis, it would be a simple additional step to generate a zonal source term for OCS derived SO_2.

This loss rate allows us to estimate an annual mass loss of OCS in the stratosphere,

$$M_{\mathrm{s}}^{\mathrm{loss}} = \sum_{z}^{\mathrm{strat}} L(z)\chi(z)M(z) \tag{4.4}$$

Based on loss rate values from Chin and Davis (1995), we calculate $M_{\mathrm{s}}^{\mathrm{loss}}$ to be 5.20$\pm$1.19 $\times 10^{10}$g yr^{-1} for our MIPAS OCS VMRs. In contrast, rates of 5.6, 4.7–11.2 and 3.75 $\times 10^{10}$g yr^{-1} have been given by Chin and Davis (1995), Engel and Schmidt (1994) and Weisenstein et al. (1997) respectively.

The stratospheric photochemical lifetime, τ_{s} is given by

$$\tau_{\mathrm{s}} = \frac{1}{L_{\mathrm{s}}} = \frac{\text{Stratospheric mass}}{\text{Stratospheric loss}} \tag{4.5}$$

$$= \frac{0.52 \pm 0.12 \times 10^{12}\mathrm{g}}{5.2 \pm 1.19 \times 10^{10}\mathrm{g\ yr}^{-1}} \tag{4.6}$$

$$= 10.0 \pm 0.31\mathrm{years} \tag{4.7}$$

This is in contrast to the global lifetime calculated previously.

Let us make the assumption of total flux of OCS into the stratosphere to be a function of the VMR at the tropical tropopause. For August 2003 this value ranged between 510 and 580 pptv. The troposphere stratosphere exchange has been estimated at 6.5×10^{20} g yr^{-1} by Rosenlof and Holton (1993). This gives a total mass of OCS entering the stratosphere of 0.33–0.38 Tg yr^{-1}. However, we have already calculated that only 0.052 Tg is lost, and this value must correspond to the net flux into the stratosphere. As a result, approximately 0.3 Tg yr^{-1}, or 90 % of OCS must return from the stratosphere for destruction at the surface or re-circulation.

4.6 Climatologies

The same approach used to create the data used in the zonal and global means (Sections 4.4 and 4.5) was applied to the equinox and solstice months for which sufficient data is present. Figure 4.22 shows a summary of these results, with each monthly zonal mean containing approximately 15,000 profiles. There is a clear seasonal tropospheric variation, concentrated in the Northern hemisphere. This is in line with biomass development, as discussed in the introduction. These results have the potential to be an important resource for the calculation of source, sinks, atmospheric sulphur loading, and fluxes. In addition OCS provides one route to the validation of the modelling of the hydroxyl radical in chemical transport models.

4.6.1 Model Validation

The result of model calculations (C. Timmreck, *Pers. Comm.*) can be compared against the zonal means shown in Figure 4.22. The colour scale has been modified to attempt to match the model data and the results are shown side by side in Figure 4.23.

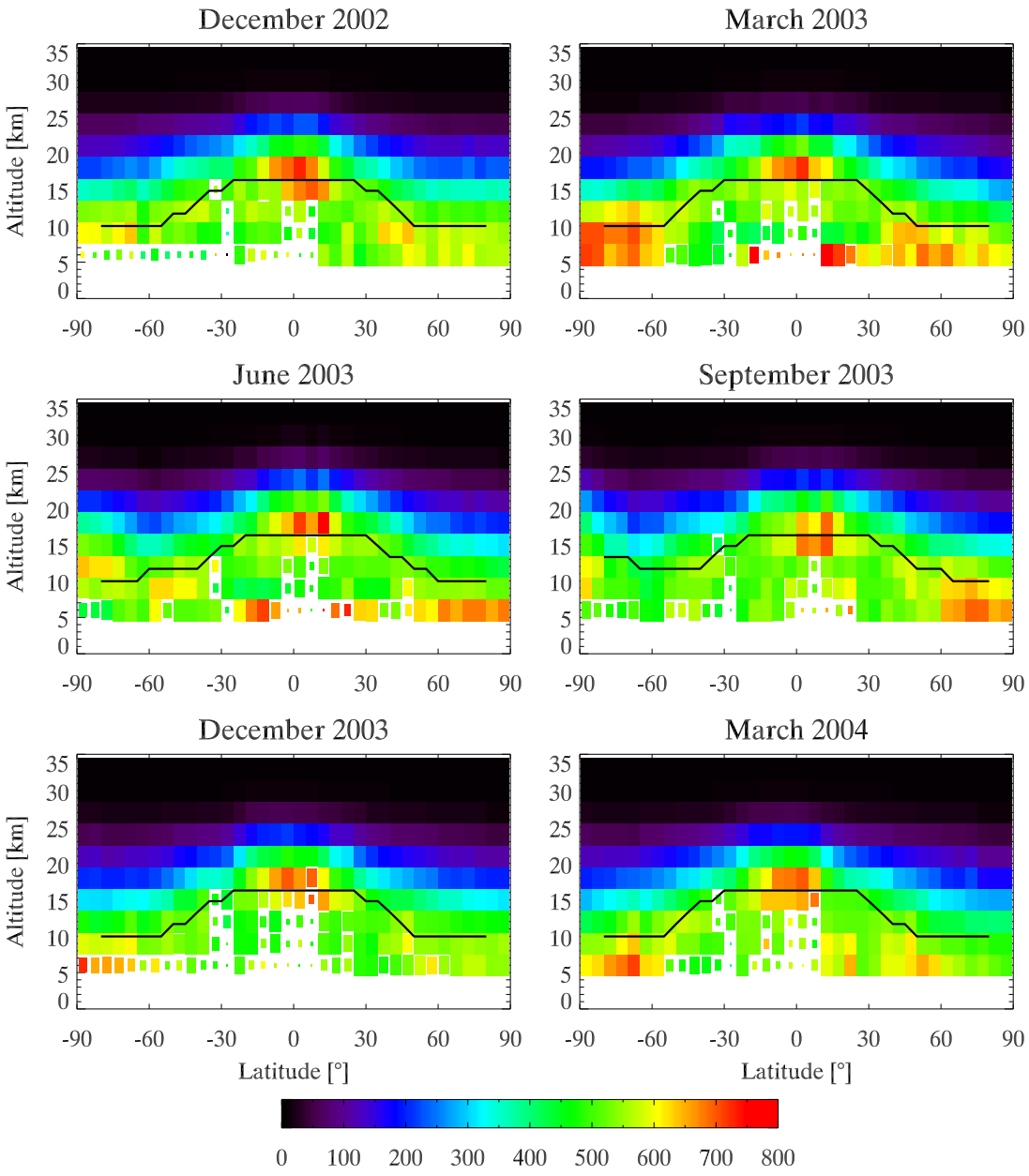

Figure 4.22: Zonal means for equinox and solstice months, December 2002 to March 2004. These allow the investigation of interannual variability (consistency of gross features) and seasonal trends (month-to-month variability).

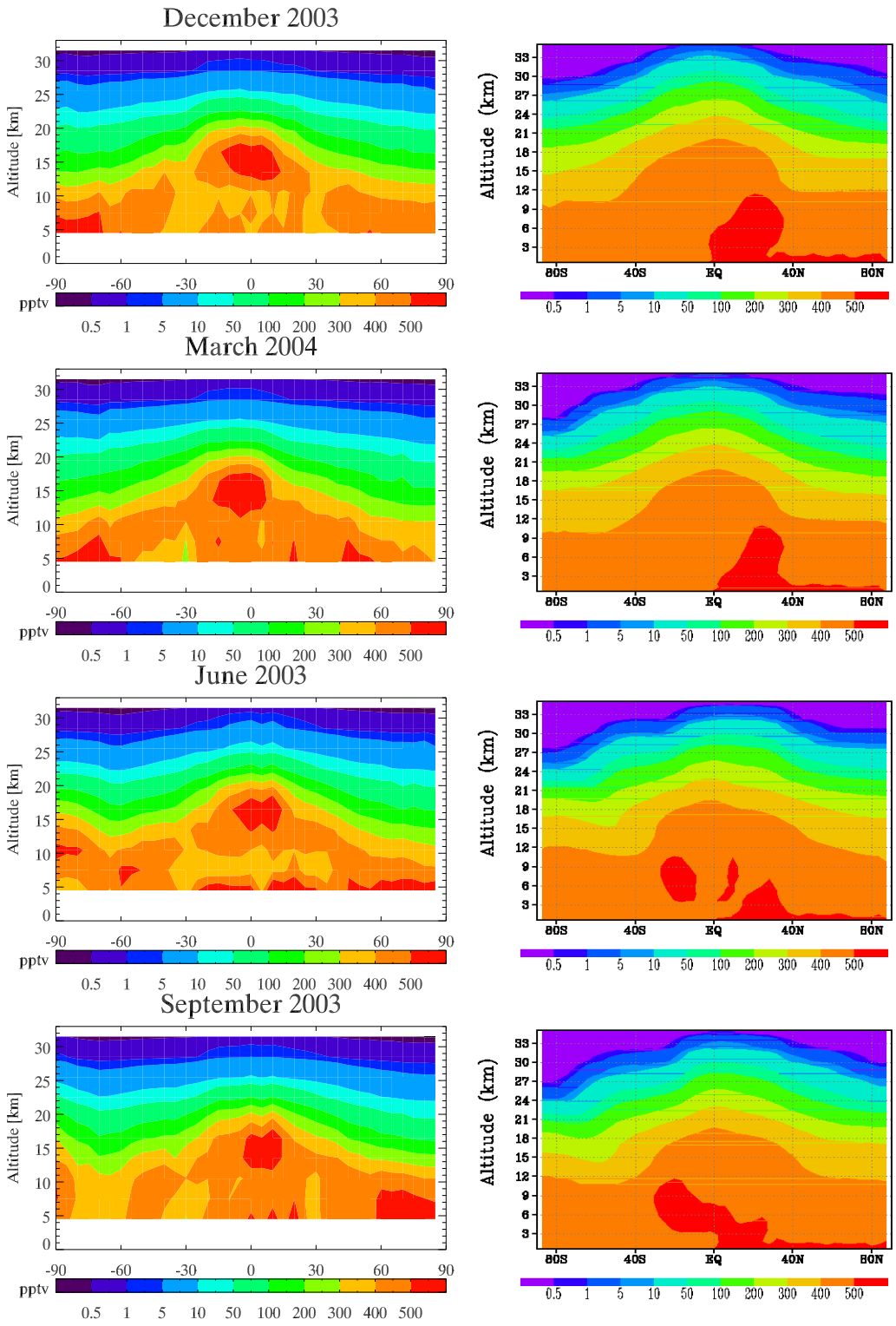

Figure 4.23: Comparison of the equinox and solstice month MIPAS retrieved zonal means with model OCS fields for the same seasons. There is good agreement in general structure. More subtle features, such as the motion of the centre of the tropical tropopause through the year is also visible.

4.6.2 Trends

The influence of time-dependent systematic errors on the calculation of trends is a significant problem. For the case of OCS, however, the only impact is likely to be on the accuracy of the internal validation (null) test for an annual trend. Hemispheric mean values for the solstice and equinox and solstice months are shown in Table 4.3. As noted with the zonal means, a tropospheric seasonal cycle appears to be present, but the other months would need to be analysed to have greater confidence. Unfortunately, the dataset is not long enough to determine any interannual tend. High accuracy measurements have been made at a single point for over 20 years as reported by Rinsland et al. (2002). Their analysis gave a 2–10 km mean value at mid latitudes (32° N 116° W) of 530 pptv, with a seasonal cycle of 1.28±0.4% about this mean value. This is certainly in good agreement with this trend data.

Table 4.3: Hemispheric and seasonal trends and variability in OCS VMR in both the troposphere and stratosphere.

Month	Troposphere			Stratosphere		
VMR (pptv)	NH	**Gbl**	SH	NH	**Gbl**	SH
December 2002	517	**507**	494	365	**365**	365
March 2003	519	**532**	541	352	**364**	375
June 2003	516	**516**	514	381	**366**	348
September 2003	540	**513**	484	380	**357**	332
December 2003	499	**499**	497	357	**354**	349
March 2004	484	**500**	510	328	**346**	362

4.7 Conclusions

There has previously been a serious lack of a well sampled (temporally and spatially) global OCS profile data. One application of these retrievals has been in tightening the

constraints applied to the lifetime of OCS in the atmosphere. The alternative application of the data would be further constraining the source and sink processes that govern OCS distribution in the atmosphere.

A second application of the work is in calculating the global sulphur budget. We have used MIPAS observations to calculate a new value for the total mass of OCS in the atmosphere. Combined with measurements of other species, we can better quantify the role of OCS in global sulphur chemistry and in the formation of SSAs.

The zonal distribution of OCS in the stratosphere has allowed the calculation of an updated stratospheric lifetime and flux, as well as better quantifying the OCS SO_2 source term.

Another application of this work is in both initialisation/forcing and validation of newer 3D chemical and transport models that seek to investigate more complex atmospheric phenomena. Certainly, model comparisons will form a key part of the validation of the work, as global distributions are not accessible by any other method.

Most of the features of the zonal means can be explained by our current understanding of the processes that influence OCS. The only region of uncertainty is the tropical tropopause enhancement, where this thesis has offered two explanations — strong ascent or unresolved tropopause structure.

Significantly, the diurnal validation performed gives significant evidence that the non-LTE effect for OCS in remote sensing is much less dominant than for other short wavelength species, NO and CO.

MIPAS observations and the retrievals in this chapter have backed up the previous observations that OCS has little significant annual trend, although the scatter is greater than would be expected and there is the potential for further work in this area.

Finally, the shape of the retrieved profiles has allowed updated estimates of the stratospheric lifetime of OCS, based on other literature assumptions.

We have tried to give an impression of both the significance and difficulty of carbonyl sulphide retrievals, along with a demonstration of the current progress that has been made. It is thought that the global OCS distribution will aid the understanding of aerosol formation and the interaction of this species in the atmospheric sulphur cycle.

4.7.1 Further work

From a retrieval point of view, OCS has the potential to become an 'operational' species, using the approach described in this chapter. It would greatly benefit from a dedicated ground validation campaign, to try and assess the significance of various systematic errors, especially the spectral database inaccuracies. In addition, as newer satellite instruments come online, seasonal comparisons will be useful.

A second area of further work would be trying to increase the altitude range of the retrieval, being very careful to avoid the introduction of a priori biases in the areas of very low signal. It is around 30 km that the exact OCS value is useful as it will heavily constrain the lifetime and hydroxyl radical abundance.

Chapter 5

Sulphur Hexafluoride

This chapter describes the retrieval of SF_6 profiles from nominal MIPAS data. It continues with the theme of retrieving trace gases with unusual features. In this case, a non line-resolved band feature in the MIPAS 'A' region. The procedure is complicated by high sensitivity to temperature, due to its position on the Planck curve, as well as significant spectral overlap with water vapour. As a result, 'joint' retrievals are investigated.

5.1 Introduction

Sulphur Hexafluoride (SF_6) is a highly symmetric octahedral molecule, point group O_h. Its main vibrational-rotational transitions in our region of interest are centered around a single ν_3 Q branch at 947.9 cm^{-1}, with band limits 915-960 cm^{-1} (Flaud, 2002; Rinsland et al., 1992a; Varanasi et al., 1992). This intense spectral feature gives rise to a strong radiative effect, with SF_6 being three times stronger as a 'greenhouse gas' than an equivalent volume mixing ratio of CFC–11 or a thousand times that of CO_2, making it one of the most efficient greenhouse gases, Ko et al. (1993). The

contribution of SF_6 to radiative forcing is small because its current atmospheric concentration is less than five parts per trillion by volume (Rinsland et al., 2003; Maiss et al., 1996; Maiss and Levin, 1994; Zander et al., 1991).

Sources, Sinks and Distribution

The sources of SF_6 are almost entirely anthropogenic (Ko et al., 1993), as its inertness and electrical properties make it an ideal choice for the exclusion of air in magnesium smelting and for use in electrical switchgear. A very minor natural source from fluoritic rocks has been suggested by Harnisch and Eisenhauer (1998). The main loss mechanism in the atmosphere is electron capture and subsequent removal of fluorine by hydrogen (radicals). A similar dissociation is also caused by high energy photons. Both these processes only become significant in the mesosphere (Reddmann et al., 2001).

As the atmospheric lifetime of SF_6 is of the order of several thousand years (Patra et al., 1997) there is the potential for the gas to slowly accumulate in the atmosphere and to become a significant contributor to radiative forcing. In addition, this longevity and persistent long term increase in emission allows SF_6 to be used as a tracer for determining the age of stratospheric air (Harnisch et al., 1996; Waugh and Hall, 2002).

Previous trend estimates concerning the change in its atmospheric abundance give an increase of 5% – 8% per year (Krieg et al., 2005; Maiss et al., 1996; Geller et al., 1997; Rinsland et al., 1993), corresponding to 0.15 – 0.35 pptv yr^{-1} at the time of their publication. However, there is evidence to suggest that the rate of increase in emission, if not production, has slowed in the past few years due to better containment and greater awareness (Dervos and Vassiliou, 2000; Maiss and Brenninkmeijer, 1998). Attributed to dynamical effects, a mean tropospheric interhemispheric variation of the order of 5–10% (0.27 ± 0.2 pptv) has also been reported Geller et al. (1997). This

corresponds to an interhemispheric exchange time of just over one year, although it has been based on measurements at only a handful of locations.

An estimated mean atmospheric profile, lying between polar and equatorial values, is shown in Figure 5.1 and is based on the MIPAS reference atmospheres (Remedios, 1999). These in turn, were based on a very limited set of height-resolved SF_6 measurements. The profile shows uniformity due to good mixing with respect to its lifetime in the troposphere and an age-related falloff in the stratosphere, a consequence of the low chemical loss rate.

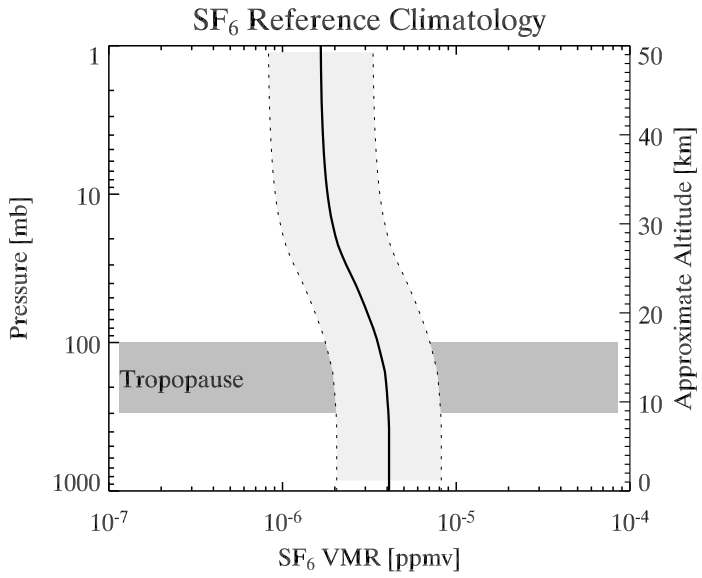

Figure 5.1: Climatological sulphur hexafluoride profile and its associated 1-σ uncertainty as defined in the MIPAS reference atmospheres. The approximate location of the tropopause is shown by the shaded region and both pressure and corresponding altitude are shown on the axes. This estimated profile is latitudinally and seasonally invariant.

Atmospheric Applications

As mentioned above, the high degree of inertness coupled with longevity and a very low natural emission allows SF_6 to be used as a tracer for determining the age of

stratospheric air. As such, the retrieval of profile data will be of value to modellers, the study of atmospheric dynamics, and groups interested in the radiative forcing influence of SF_6.

In summary, due to its observed trend, long lifetime and strong infrared properties, better knowledge of SF_6 looks to be of increasing significance in successfully modelling the radiative processes that govern our atmosphere and climate.

5.2 Feasibility and Microwindow Selection

Figure 5.2 shows the SF_6 contribution to the limb radiance for the lower stratosphere (12 km). The SF_6 signal exceeds the MIPAS NESR between about 944 and 951 cm^{-1}, suggesting that a retrieval is feasible. The spectral coverage of the best six microwindows is also shown, along with their altitude sensitivity. The exact microwindow parameters are listed in Table 5.1, below.

The error analysis resulting from the microwindow selection is shown in Figure 5.3. The selection was run to maximise the information content, with constraints on computational cost of using the microwindows relaxed. Masks were applied to improve the systematic errors.

5.2.1 Systematic Errors

From Figure 5.3, it can be seen that the dominant systematic error sources are prior temperature retrievals, spectroscopic calibration errors ('SHIFT', 'SPREAD') and unmodelled gradients in the field of view ('GRA'). Water vapour is also significant, mainly due to its strong gradient around the tropopause. Other systematic errors of significance include the spectral database, as discussed below. With the exception of

Table 5.1: The six best sulphur hexafluoride microwindows, in order of information contribution. Microwindow 105 is very narrow, filling in a gap left between 103 and 101, that is necessary because of the 3 cm^{-1} MW width limit. Even so, it contributes more information that the final microwindow, 106. In effect 101 – 105 cover the entire main SF_6 band between 939.950 and 952.650. cm^{-1}

Microwindow	Band	Spectral Range [cm^{-1}]	Altitude Range [km]
SF6_0101	A	946.625 – 949.625	6 – 42
SF6_0102	A	949.650 – 952.650	6 – 33
SF6_0103	A	942.975 – 945.975	6 – 33
SF6_0104	A	939.950 – 942.950	6 – 52
SF6_0105	A	946.000 – 946.600	6 – 33
SF6_0106	A	928.525 – 931.525	6 – 33

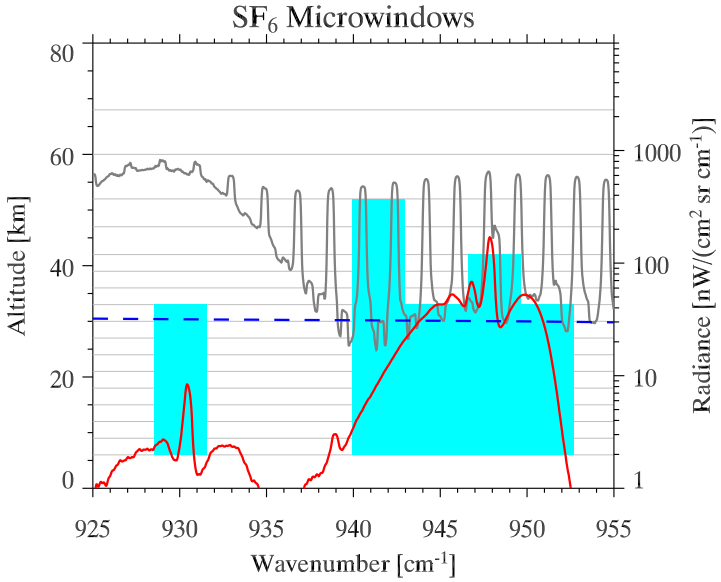

Figure 5.2: The region of the MIPAS spectrum containing the microwindows chosen for SF_6 retrieval and their altitude ranges (outlined by the shaded regions, left axis). The nominal instrument NESR (dashed line), SF_6 radiance contribution (lower line) and total atmospheric radiance (upper line) for a simulated 12 km view are also shown (right axis). The SF_6 molecule contains no other significant transitions within the MIPAS spectral range.

spectroscopic errors, most others would be expected to become decorrelated after a few days so are not problematic when considering trends across different months and

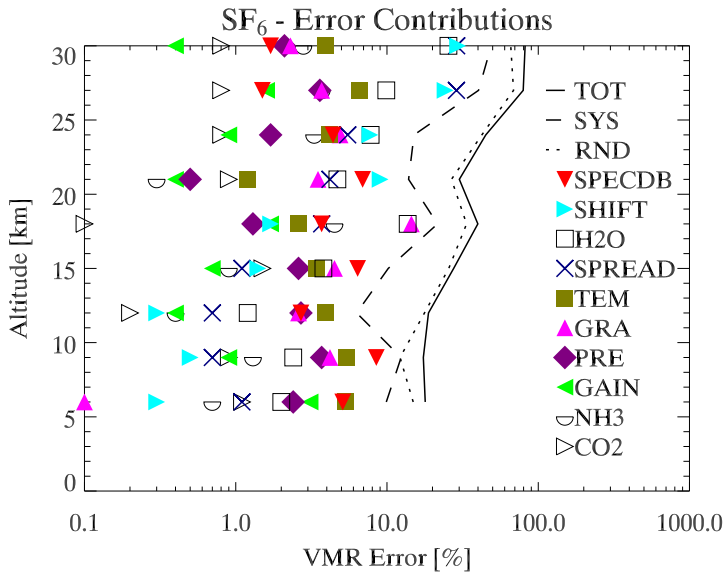

Figure 5.3: Plot showing random error (dotted line 'RND') to be the dominant error source in the retrieval, along with the systematic ('SYS') and total error budget. As discussed in the theory section, noise in the spectrum is mapped directly to random error through the microwindow selection process, and these results are based on the NESR of the instrument. A full list of systematic terms appeared in Table 2.1.

the subsequent generation of climatologies.

Spectral Accuracy

As discussed in Section 2.2, the microwindow error analysis is critically dependant on the accuracy of the error terms supplied. We have already seen that for interfering gases, the concentrations are generally known to within an order of magnitude, and much better for the more abundant gases that have a significant radiometric impact. Likewise, the instrument errors are well characterised. The spectral properties of commonly studied species are also well known, if only for the major transitions. Models and measurement are combined to give good estimates of their line parameters.

Unfortunately, very dense molecular spectra, such as that exhibited by SF_6, are difficult to model. As a consequence, it is necessary to use absorption cross-section

data in place of line parameters. These have to be measured in the laboratory for several pressure (abundance) and temperature ranges that span potential atmospheric conditions. In the case of the tabulated cross-section data for SF_6, shown in Figure 5.4, the temperatures range from 180 – 295 Kelvin and the pressures from 20 – 760 Torr, Varanasi et al. (1992). This cross-section data is then interpolated to match the calculated atmospheric state during the forward model step of the retrieval, which — along with the potential for significant uncertainties in the accuracy of the cross-section measurements — is a major disadvantage of using this type of data. A minor advantage over line parameterisation is the incorporation of various spectroscopic effects, such as line shapes, and this reduces some areas of systematic errors. The accuracy of the cross section data and other parameters used in this work has been discussed in both Flaud (2003) and Flaud et al. (2003), and for atmospheric conditions, the estimated error is 3-6% in the absolute band strength (Varanasi et al., 1992).

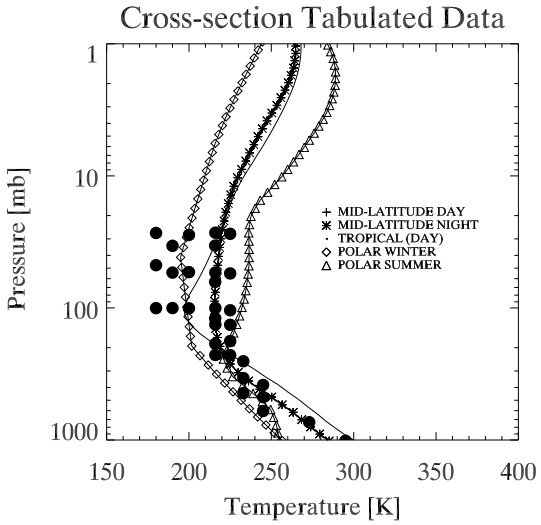

Figure 5.4: Plot showing the tabulated cross-section data for SF_6 as published by Varanasi et al. (1992). The lines on the figure outline the expected climatological atmospheric temperature and pressure distribution. The filled circles show the pT pairs where cross-section data has been taken. Interpolation occurs between these points and (unfortunately) extrapolation may also be performed for pT combinations outside these measurements.

5.2.2 Variations in Selected Microwindows

The compact nature of the spectral feature means that there are no alternative microwindow regions possible. Only the order of the microwindows can be changed (and to some extent, the boundaries). Neither of these variables should have a significant effect on the total information retrieved. Although up to ten microwindows can be found, the information gain is well below 0.1 bits per microwindow after the sixth, making it computationally wasteful for a minor (if any) gain. This is shown in Figure 5.5.

The maximum available radiance can be easily calculated from a simulation, and compared with the radiance used by the chosen microwindows. In effect, comparing the spectral resolving power of MIPAS against a SF_6 selective radiometer. The results are summarised in Table 5.2. The microwindow approach appears better than the radiometer approximation, especially when the effect of spectral masks are taken into account, removing a significant systematic component from interfering species.

Table 5.2: Comparing optimised microwindows against a broadband approach for a simulated day time atmosphere at 12 km. The signal is in units of nW/(cm^2 sr cm^{-1}) cm^{-1}, from calculating the total radiance over the region. Likewise, the noise is calculated by multiplying the 'A' band nominal noise level of 50nW/(cm^2 sr cm^{-1}) by the number of wavenumbers in the selected region.

		Points	[cm^{-1}]	Effective Noise	Signal	S/N
Broadband	[915-960]	1800	40.0	$2250/\sqrt{1800}$	462	8.3
MWMake	[6 MWs]	624	15.6	$780/\sqrt{624}$	441	14.2

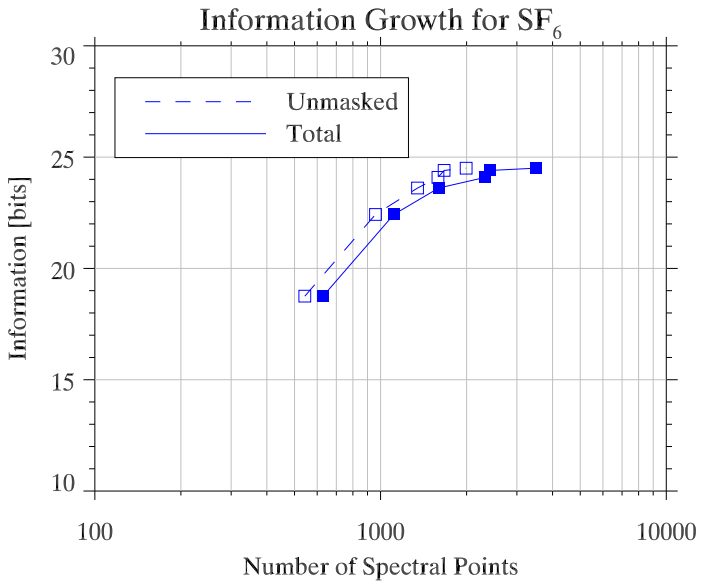

Figure 5.5: Information gain by adding additional SF_6 microwindows. Due to the limited extent of the band feature, all the major regions are selected. The total information possible is asymptotic towards 25 bits as additional MWs are added covering the whole band range.

5.3 Retrieval from Simulated Data

The RFM was used to create a series of spectra based on daytime climatological profiles. The core simulations were performed on the nominal 3 km retrieval grid and the computationally efficient low resolution field of view parameterisation. In addition, separate simulations were performed with an atmospheric profile resolution of 1 km, together with a high accuracy field of view parameterisation. These settings more accurately simulate the fine structure of the atmosphere that can not be resolved by MIPAS but can influence the retrieval. This is especially significant around the tropical tropopause, where there is a very strong temperature inversion.

The aim of the simulations is to ensure the microwindows chosen in the previous section are appropriately selective and sensitive to SF_6. All the following experiments were performed using the MORSE retrieval code and the optimal estimation approach.

The initial guess was set to be the a priori for all cases.

5.3.1 Ideal Radiances

For these microwindow validations, there was neither random noise nor cloud present in the simulated spectra. Although no random noise was present in the spectra, an unapodised value of 30 nW/(cm^2 sr cm^{-1}) — in line with MIPAS calibration values — was used in the retrieval so the resulting error bar is approximately the same as retrieving from single real measurements. Figure 5.6 shows the results of a sequential retrieval of pressure/temperature followed by water vapour and finally SF_6. Other diagnostic information, such as the averaging kernels, are also shown. We observe that the random error bound, shown previously in Figure 5.3, agrees with the retrieved random error. Subsequently, Figure 5.7 shows the sensitivity of the microwindows to changes in the simulated SF_6 abundance, by repeating the forward model simulations with different profiles, but applying the same retrieval and a priori settings as for the ideal test case.

Sensitivity to Parameters Outside the State Vector

Various retrieval settings influence the final result through the influence they have on the underlying simulation of the physics of the observation. This is more pronounced for SF_6 than it was for OCS. Figure 5.8 shows the influence of a selection of these parameters. The results highlight the sensitivity of the retrieval to systematic errors within the forward model representation of the atmosphere. If we more closely model the true structure, the effects of limitations in the observing system become apparent. Fine atmospheric structure is simply not resolved by the 3 km FOV of the instrument. This leads to incorrect modelling of the radiance. As expected, the best retrieval is achieved when the forward model parameters used by MORSE most closely match

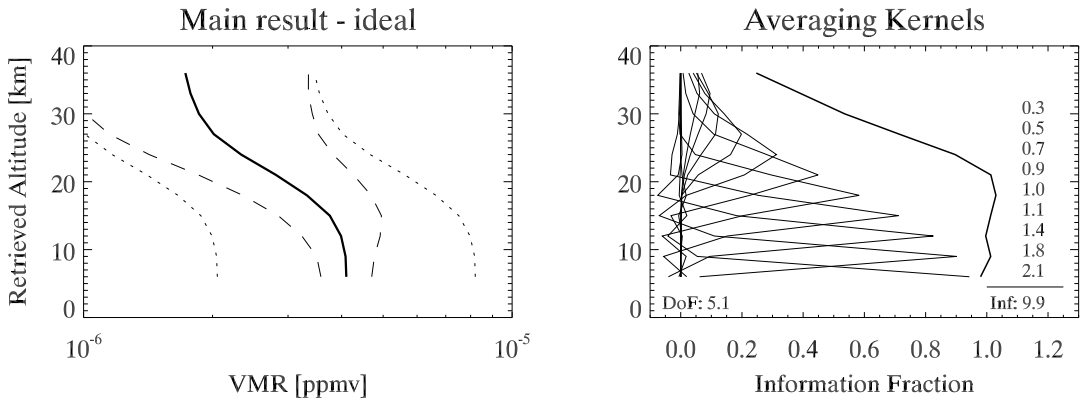

Figure 5.6: Results of retrieving, in sequence, pressure and temperature followed by water vapour and finally SF_6. This is the ideal case where the initial forward model parameters most closely resemble the retrieval parameters and the a priori and initial guess were set to the 'true' simulated value. The a priori uncertainty was 100%. Diagnostic information, including the averaging kernels, is shown on the right. There are just over 5 degrees of freedom in this profile, of nine levels considered. The Shannon information gain for this retrieval was 9.9 bits. There is significant prior information contribution above 24 km although it does not reach 50% until 30 km.

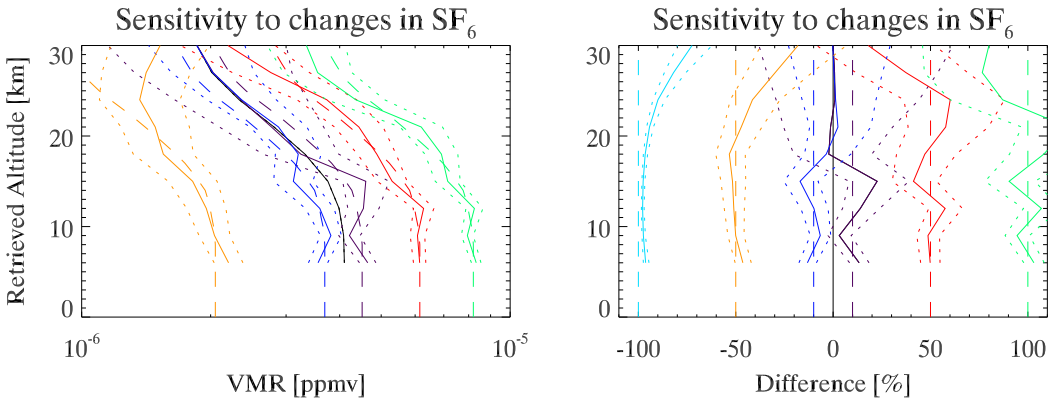

Figure 5.7: Deviations from the 'true' RFM modelled VMR values (dashed lines). [Left] Profile deviations, ppmv. [Right] Percentage deviations. The same retrieval parameters were used throughout, with the same a priori. A set of six profiles were used: no SF_6, -50%, -10%, +10%, +50% and +100% of the climatological profile. The results show the sensitivity of the microwindows to changes in the amount of SF_6 in the atmosphere. As one would expect from looking at the averaging kernels in the previous figure, there is good sensitivity at low altitude, but by 30 km the a priori becomes the dominant contribution to the final retrieved state. For the case of zero SF_6 (cyan), values of the order of 0.1–0.01 pptv are retrieved, due to the effects of retrieving in log space and the influence of the a priori.

those used in the initial RFM simulation. These parameters are not necessarily the best for the actual retrieval.

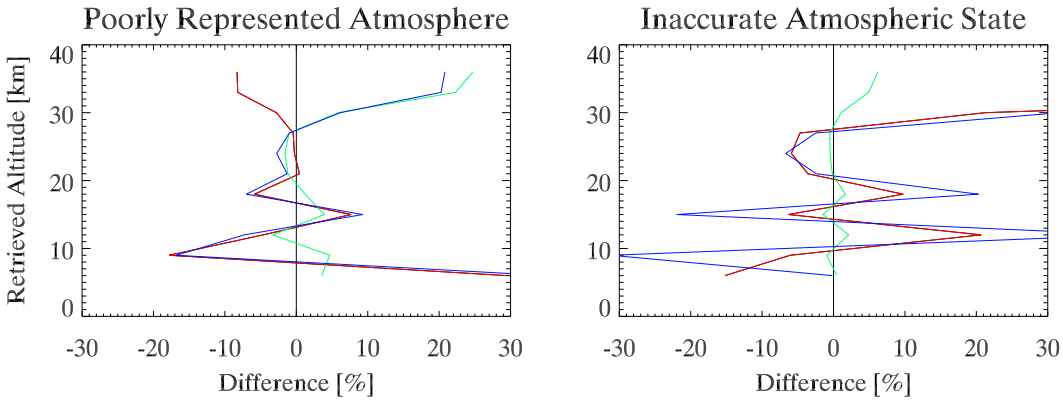

Figure 5.8: Sensitivity to parameters outside the state vector, specific to the case of SF_6.
[Left] The high resolution forward model cases – A more accurate field of view representation (red), modelling the atmosphere at a finer resolution (1 km) than the retrieval grid (green) and combining both these cases (blue).
[Right] Sensitivity to a 1 K increase in retrieved temperature (red), a 10% increase in water VMR (green) and combined (blue). Note how both tests induce an oscillation in the retrieval, which was also observed for many real profiles.

5.3.2 Joint Retrieval

Instead of varying one species during the retrieval, it is possible to increase the size of the state vector to allow a selection of species to be simultaneously retrieved. This is known as a joint retrieval. Using the joint retrieval approach for the same ideal simulated data used previously shows an improvement. It appears that the joint approach is less sensitive to failings in the forward model and observing system. This effect is most pronounced when the jointly retrieved species are all within a similar spectral region, as is the case for water, pT and SF_6. An illustrative result of a joint retrieval is shown in Figure 5.9, where appropriately scaled synthetic random noise vectors have been added to the ideal radiances for pT, water and SF_6 microwindows. Although one water microwindow is removed, due to overlap with SF_6, the total information gained from

the joint system is significantly better than for the sequential case. The information gains are summarised in Table 5.3, later in this chapter.

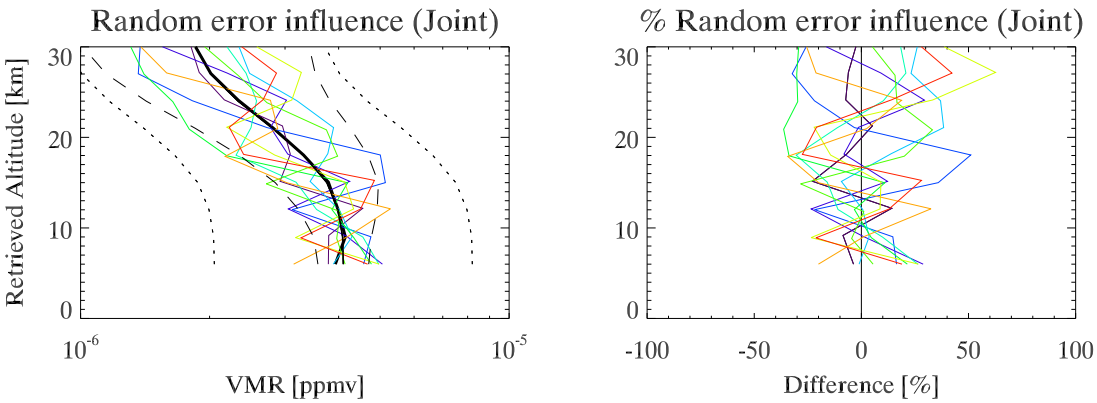

Figure 5.9: [Left] Results of performing a joint pressure and temperature, water vapour and SF_6 retrieval for a selection of noisy simulated measurements (coloured lines). The mean of these retrievals is also shown (heavy line). The scatter is of the order of the random error (heavy dashed lines), based on the simulated noise level of 30 nW/(cm^2 sr cm^{-1}). Representative diagnostic information shows 5.15 of 9 degrees of freedom for SF_6 and the Shannon information gain for this retrieval was 10.16 bits assigned to SF_6 from the first 9 levels.
[Right] The same results, but shown as percentage deviations from the ideal retrieval. The MW error analysis and Figure 5.8 have already demonstrated the high sensitivity to temperature, and the joint retrieval approach reduces this.

5.4 Retrievals

Simulating the noisy retrieval gives good indications of potential problem areas. Using real spectral data from August 2003, the same procedure was followed to give a first retrieval of SF_6.

A cloud-free mid latitude day scan was selected, using a cloud threshold of 1.8, as described in Chapter 2. Based on the results of the microwindow and retrieval validation in the previous section, a nominal 3 km atmosphere with a 12 point field of view was used in the retrieval forward model. Tests had shown that using higher resolution FOV and atmosphere had a large impact on the runtime, but improved accuracy.

Unlike for the problem of the unresolvable high resolution atmosphere, we have the ability to increase the accuracy with which the field of view is modelled. The a priori uncertainty was left at 100% (even though the climatological uncertainty is much smaller) to avoid over constraining the retrieval. Initially, a 50 km correlation length was used, providing a degree of smoothing. This large correlation length is at the expense of vertical resolution, so the final retrievals were performed using a variable correlation length that begins at 50 km in the troposphere and falls to 3 km by an altitude of 25 km. This prevents the upward propagation of information and subsequent biasing of the higher altitude values, where the information content of the measurements is low. Larger correlation lengths also act to dampen the oscillations about the tropical tropopause.

The resulting profile and averaging kernel is shown in Figure 5.10 for a sequential retrieval and Figure 5.11 for the corresponding joint retrieval. The resulting information gain for both the simulations and real retrievals is shown below in Table 5.3.

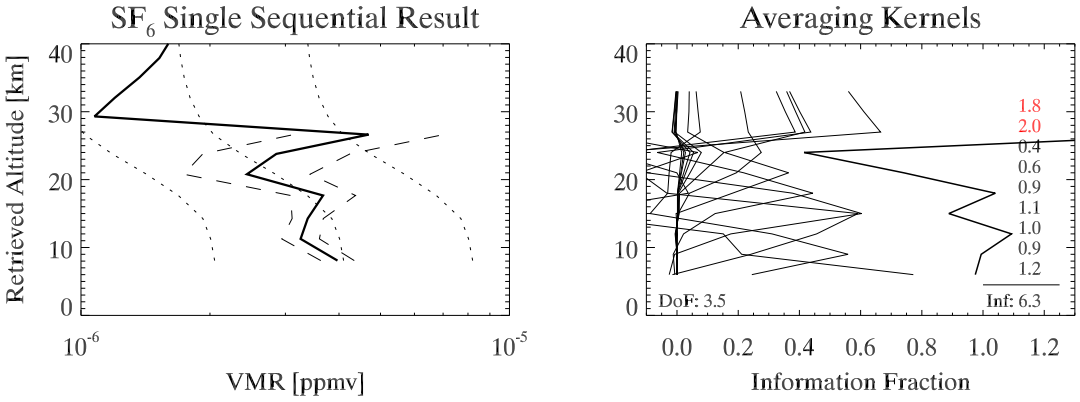

Figure 5.10: Results of retrieving, in sequence, pressure and temperature followed by water vapour and finally SF_6 from a single scan in orbit 07464 taken during August 2003 from about 55°S. The layout is the same as Figure 5.6, above. Although the spectral signature of SF_6 is not visible by eye above 30-35 km, the plot includes profile information up to 40 km to give an indication of the behaviour of the retrieval.

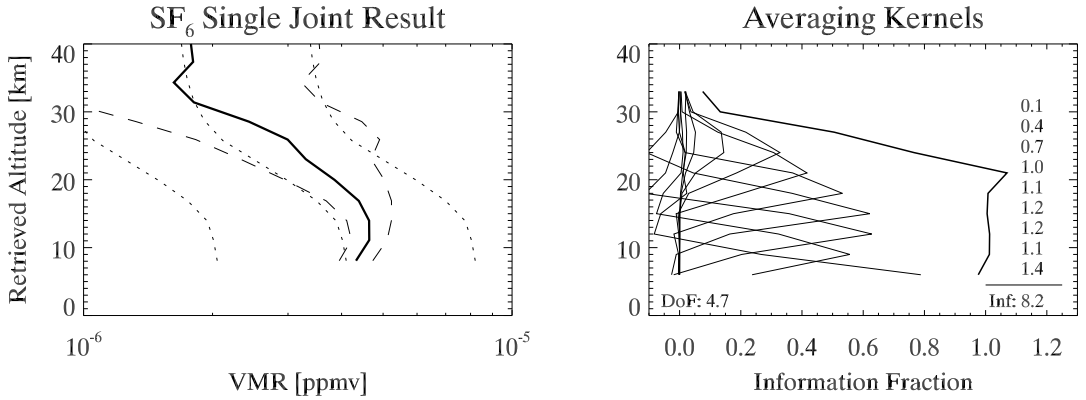

Figure 5.11: Results of jointly retrieving pressure and temperature, water vapour and SF_6 from the same scan as Figure 5.10. The smoother profile and better averaging kernels are indications that the joint approach gives better retrievals for the SF_6 retrieval.

Table 5.3: Comparison of information gain for real and simulated data (truncated to 33 km).

	p+T	H_2O	SF_6	Total (bits)	SF_6 Deg Freedom
Simulated Data					
Sequential	43.69	13.00	9.86	66.55	5.08
Joint	49.48	16.92	10.16	76.56	5.15
Real Data					
Sequential	42.28	13.01	6.34	61.63	3.51
Joint	47.72	20.03	8.22	75.97	4.74

5.4.1 Single Orbit

Figure 5.12 shows a set of 72 profiles from a single orbit with much low level cloud. The structure, as expected, shows higher VMRs at the equator. The southern pole shows evidence of low VMRs in the mid stratosphere, which is probably dynamical.

5.4.2 Latitude Bands

The global mean profile obtained from August 2003 is shown in Figure 5.13. It shows tropospheric (well mixed, little variability with altitude and latitude) and stratospheric

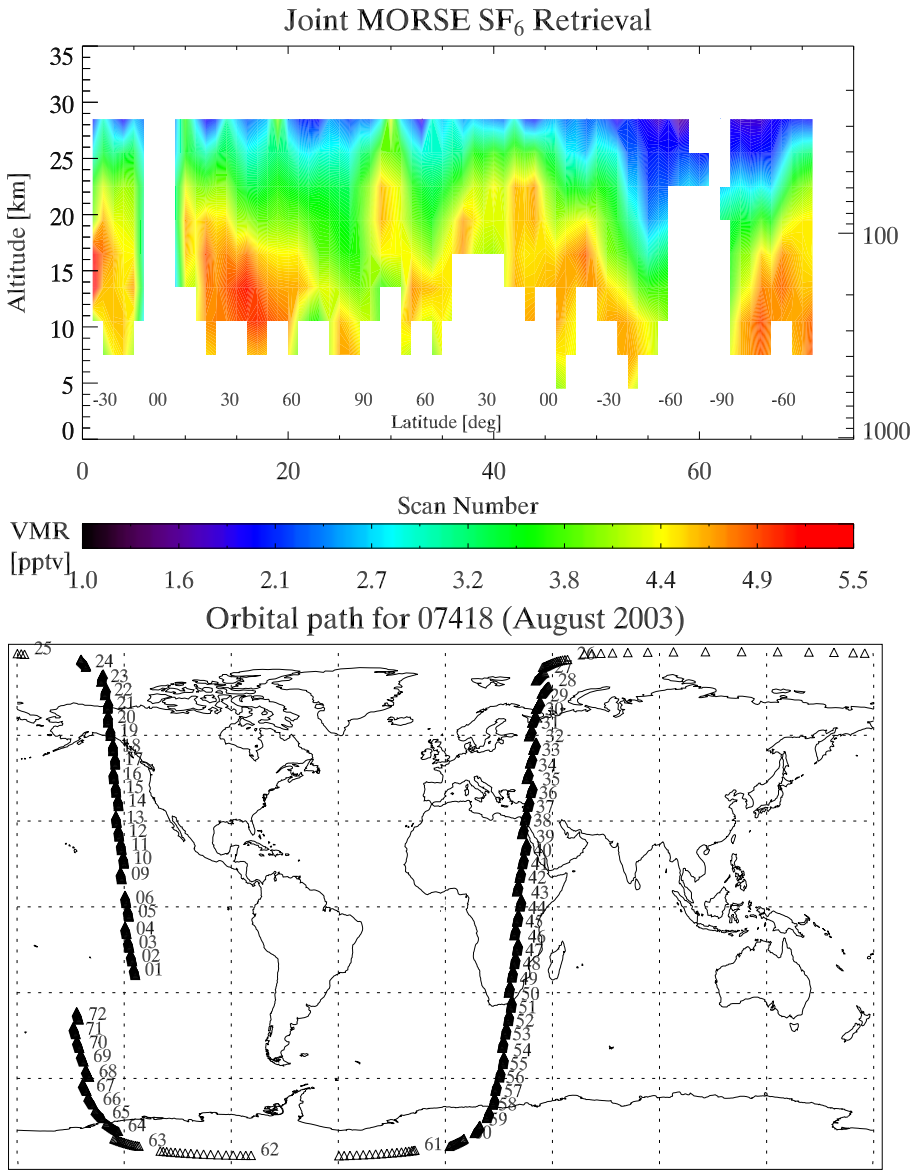

Figure 5.12: Curtain plot of SF_6 for a single arbitrary orbit in August 2003. Pressure, temperature and water were jointly retrieved. Cloud detection and correlation length were the same as before. The origin of the enhancement above the equatorial tropopause (20-25 km) is, based on simulations, related to high resolution tropopause structure. Correlation length was variable (troposphere: 50 km) and the cloud ratio threshold was set to 1.8.

regions. The decrease in VMR with altitude is attributed almost entirely to the increasing age of the air, as there is no significant loss mechanism for SF_6 in the troposphere

and stratosphere. There is poor coverage in the tropics for the 6 – 9 km levels due to cloud, and these levels are not shown. The 6 km level also shows a low bias due to significant CO_2 line broadening masking the SF_6 feature, so the sensitivity to changes in VMR decreases. By 12 km it is possible to see the decrease in VMR as the line of sight enters the stratosphere for the mid-latitude and polar measurements, but this effect does not occur until 15–20 km over the equator, as would be expected. Finally, by 30 km the younger equatorial air shows a higher VMR than mid-latitudes which, in turn, are greater than the polar air. There is also evidence in these profiles for temperature sensitivity.

In addition to the global mean, hemispheric means were taken. The number of cloud-validated northern hemispheric profiles was 6,130, similar to the 5,820 profiles for the southern hemisphere. This balance is helpful when considering the global mean, as there is a known interhemispheric variation in VMR due to industrialised anthropogenic sources in the northern hemisphere (Waugh and Hall, 2002). From these mean values, in the troposphere, a difference of about 0.17 ± 0.03 pptv is observed. This corresponds with the literature estimates of an inter-hemispheric transport time of the order of 6 to 12 months.

It was also possible to investigate latitudinal variability and the results are shown on the right of Figure 5.13. The latitude bands used are the same as those chosen for the climatologies, and do not necessarily emphasise the differing structures between different areas of the atmosphere. One feature that is missing from these figures is a strong tropopause signature, characterised by a sudden drop in VMR equal to the transport time from the troposphere at mid tropics to the mid latitude UTLS. This is briefly discussed by several authors (Patra et al., 1997; Ko et al., 1993). Its absence is simply due to the variation in tropopause height around the orbit and throughout the month, which causes a smoothing of this signature.

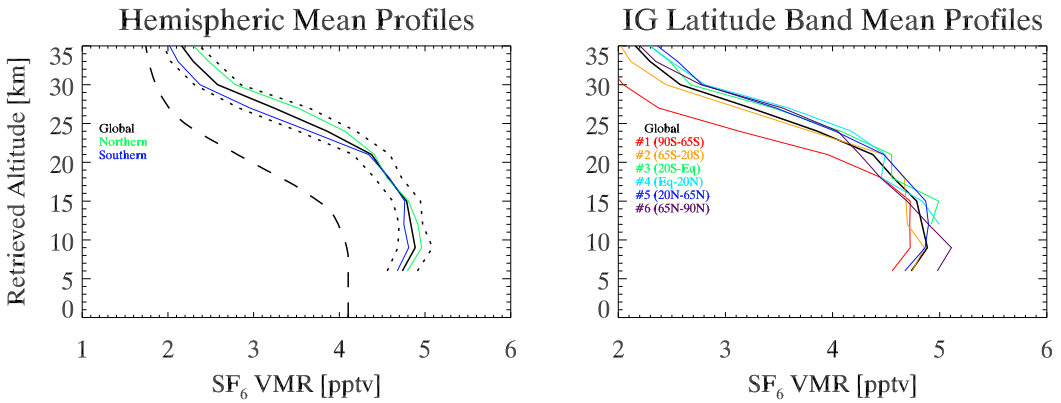

Figure 5.13: [Left] This figure shows the global mean profile for August 2003 (black line) and the hemispheric means (NH: green line, SH: blue line). The global uncertainty, based on the standard deviation of the measurements, is shown by the narrow dotted error bounds. There is a clear hemispheric difference in the troposphere, and at this time of year, the stratospheric SH mean is also clearly lower. [Right] The coloured lines correspond to the same data, split by the operational climatology latitude bands ($90-65°$, $20-65°$and $0-20°$). The southern polar line (red) is significantly different. August 2003 corresponds to the Antarctic winter with highly perturbed dynamicas and chemistry. Mesospheric descent of SF_6 depleted air is one possible explanation, although the effect has propagated as low as 20 km, where temperature retrieval inaccuracies may be invoked as an explanation.

5.4.3 Zonal Mean

A whole month of orbits can be combined after retrieval to greatly reduce the influence of random noise (and psuedo-random systematics like pT) on the retrieval. Figure 5.14 shows the result of combining 12,000 scans from August 2003. Features to note include the south polar winter mesospheric descent, hemispheric VMR difference and the overall smoothness of the zonal field. Each profile in the mean was wholly independant of the others and the a priori contained no latitudinal structure. As a result, the features purely originate from the SF_6 retrieval or persistent errors in the temperature or water fields (however, temperature is also shown in the figure and is smooth).

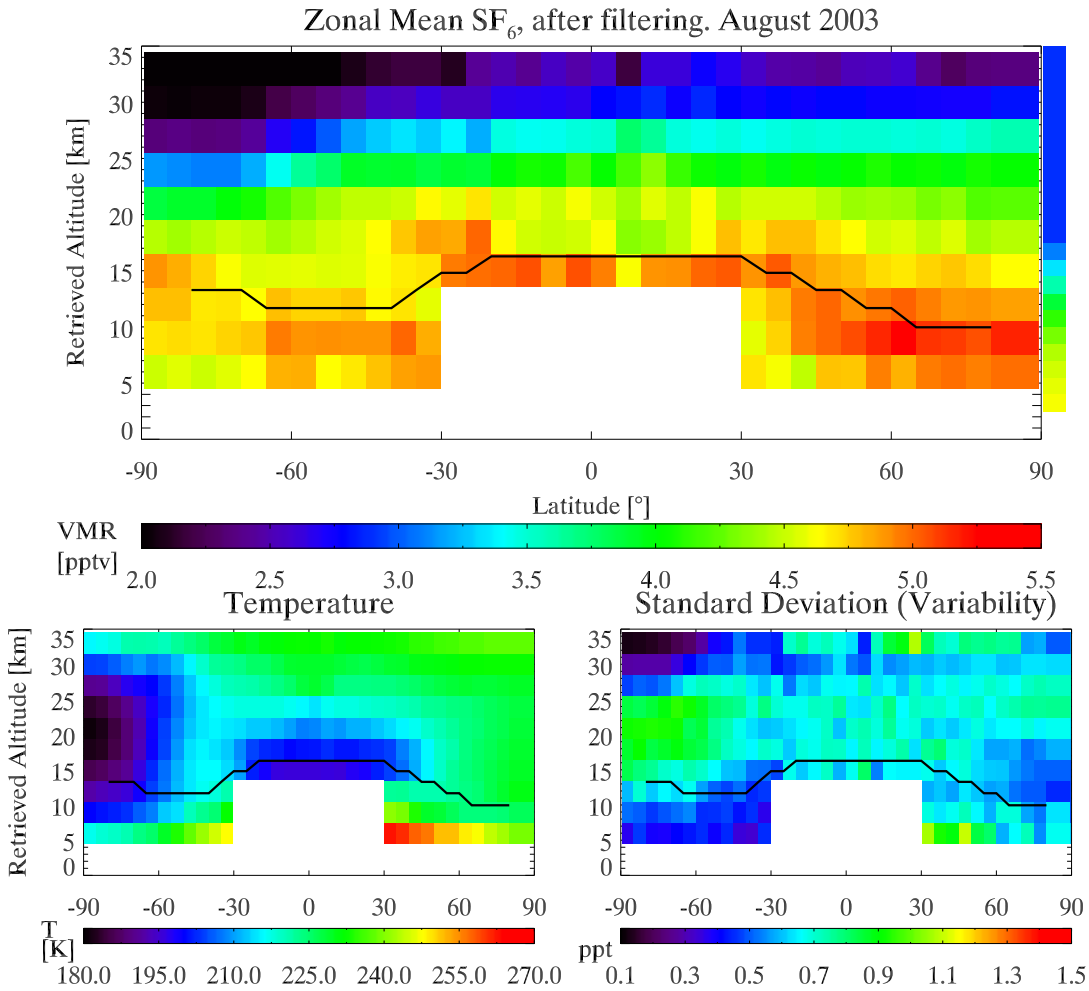

Figure 5.14: Jointly retrieved SF_6 zonal mean for August 2003. The data was gridded to a 5°latitude by 3 km altitude grid. The black line shows an approximate climatological tropopause. All sweeps marked as cloudy were removed, as were profiles containing retrieved values below 0.5 pptv and above 50 pptv. Subsequently, about 30% of tropical profiles were removed due to a strong oscillation around 18-21 km. Other latitudes were unaffected. The temperature field and the standard deviation (a measure of the variability when taken in log space) are also shown. The antarctic vortex region shows high variability, attributed to the perturbed chemistry and low temperature.

5.4.4 Global Field

Finally, the data may be shown as a function of altitude and both latitude and longitude. This reduces the number of measurements in each grid box, so the random error increases from that observed with the zonal means. Datasets like this are generally of

more use in a computer-readable format, but an example is shown in Figure 5.15 for completeness.

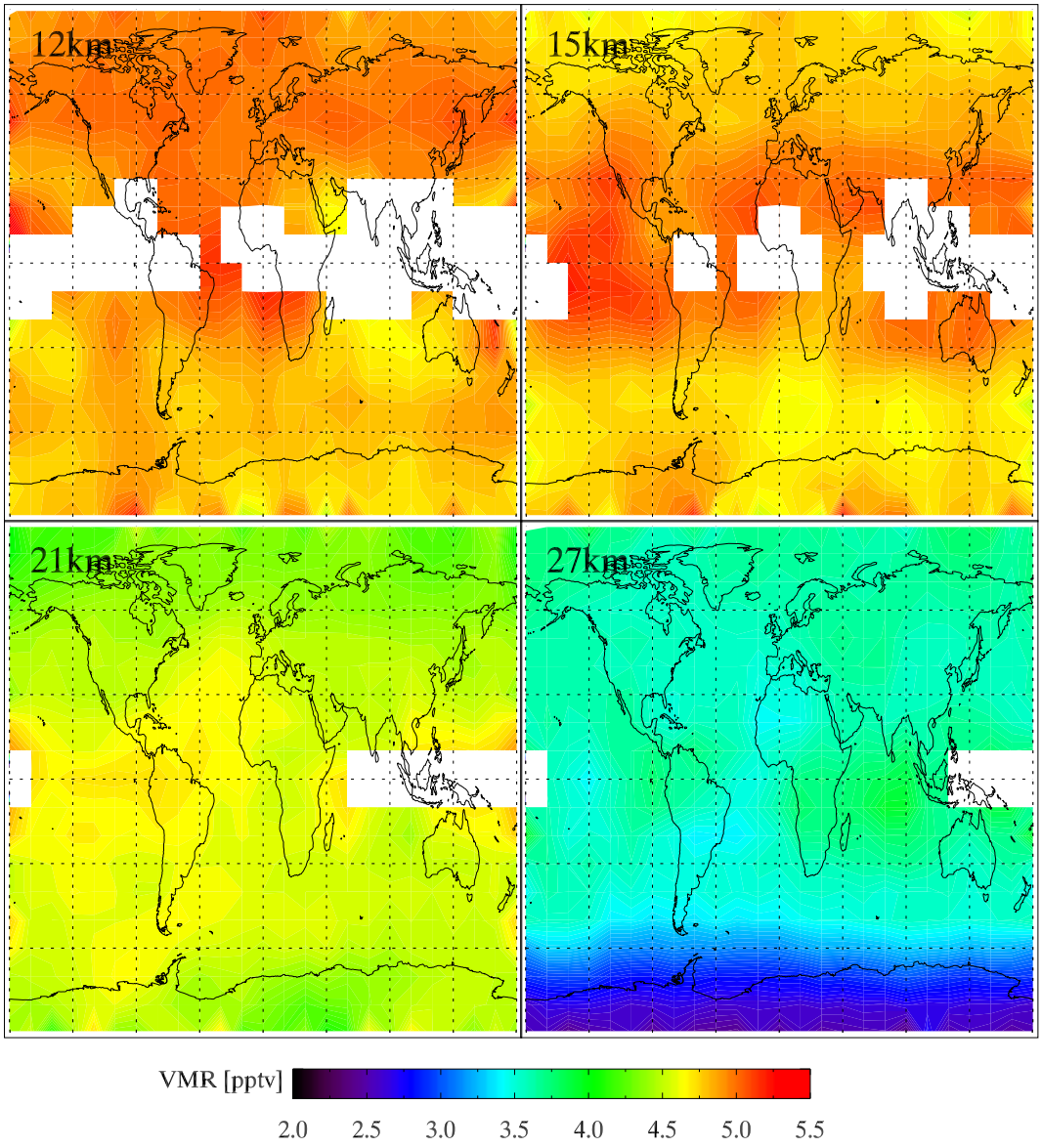

Figure 5.15: Each of the retrieved altitude layers for SF_6 showing VMR as a function of geolocation. The colour scale is the same as Figure 5.14. From top left, 12, 15, 21, 27 km. The top left box highlights the negative influence of cloud in the tropics, matching the areas of strong ascent shown in the previous chapter (Figure 4.21).

5.5 Validation

5.5.1 Internal

Figure 5.16 looks at the difference between first and second halves of the month and at the changes between day and night. For SF_6 there is no expected diurnal variation, and only a very small trend expected within the month. As a result, the high degree of similarity between these measurements is good evidence for internal consistency.

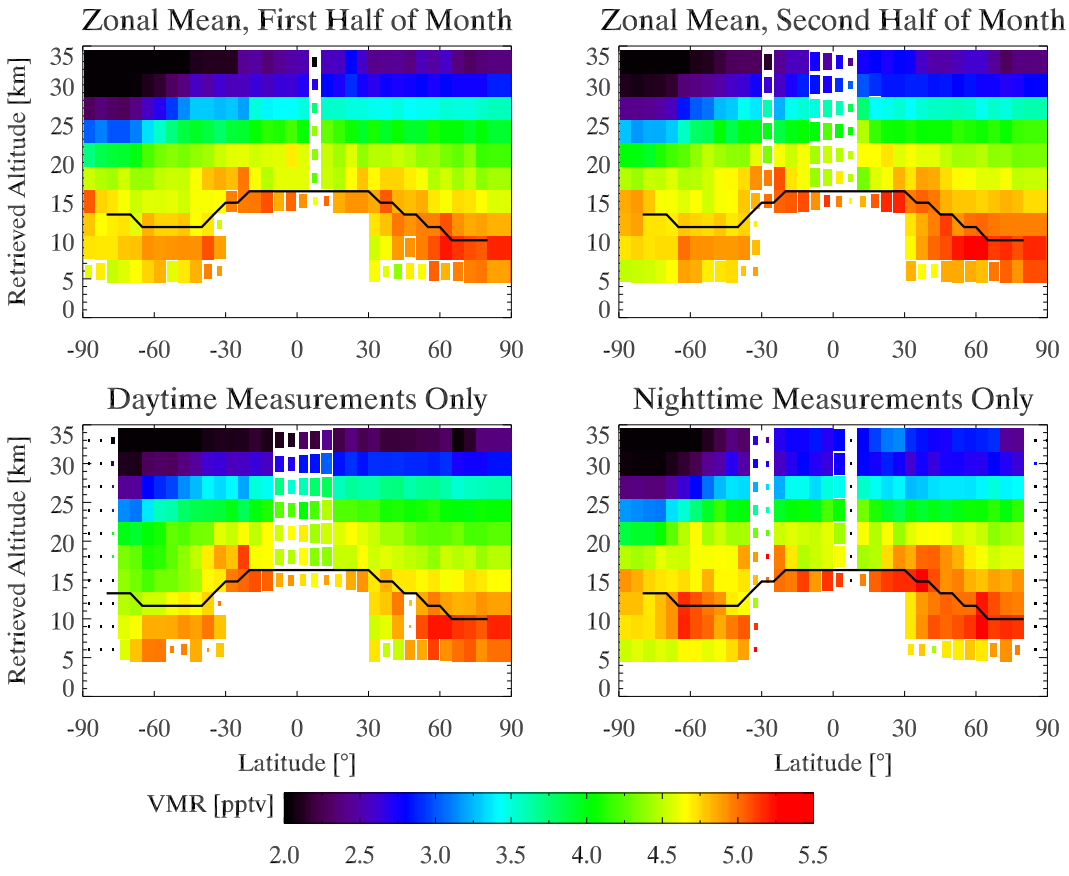

Figure 5.16: Diurnal and monthly variability as internal validation. The colour scale is the same as Figure 5.14.

5.5.2 Other MIPAS Retrievals

ISAC / CNR

The Institute of Atmospheric Sciences and Climate (ISAC) of the Italian National Research Council (CNR) group in Italy uses the same MIPAS data, but a different retrieval code and a single, wider microwindow approach (Dinelli et al., 2003). This allows us to investigate the relative performance of the two schemes. In the case of SF_6, both retrieval codes were applied to pre-release orbit number 2081 (July 2002), with preliminary radiometric calibration. Discounting scans that were cloudy, the remaining SF_6 profiles compared favourably, well within the error bars for a single scan (L. Magnani, *Pers. Comm.*). For example, a mean tropospheric value (first 10 scans, bottom three levels) for the Oxford group was 4.19 ± 0.28 pptv and for the ISAC group, 4.17 pptv (Burgess et al., 2004). Additional validation of the general performance of several retrieval schemes was made by blind test retrievals as part of the previously mentioned AMIL2DA project (AMIL2DA, 2003).

IMK

As with the initial results from this study, the work performed at the Institut fuer Meteorologie und Klimaforschung, Karlsruhe (IMK) also suffers from tropical tropopause enhancement. For a 1-week zonal average compared (21–27 October 2003), using IMK processing during August 2004, the basic zonal atmospheric SF_6 structure was very similar to our results (T. Steck, *Pers. Comm.*). For example, a mid latitude region unaffected by the tropical tropopause instability had values between the 4.5 and 5.0 pptv contours for the range 6–18 km. This is directly in line with the mid latitude results previously shown in Figure 5.13.

5.5.3 Correlations with Other Species

As the operational retrieval products are readily available, a comparison with other long-lived species is possibe. Following the approach by Strunk et al. (2000), Figure 5.17 shows the SF_6 VMR against both methane (CH_4) and N_2O. Each point corresponds to a matching geolocation. As expected, both show tight correlations and the leftward trend, especially at the lowest VMR values, is indicative of the shorter lifetimes of the two correlative species when compared with SF_6. (A rightward trend would indicate that the lifetime of SF_6 was shorter than these correlative gases.) The gradient is significant and can be used to infer the age profile of one species if the age profile of the other is known, although for long lived species this has a large associated error. Other authors, such as Volk et al. (1997) and Rinsland et al. (1996), have also made use of tracer:tracer correlations in both validation and for extrapolation of a known distribution of one species into an estimate of the distribution of another. However, Harnisch and Eisenhauer (1998) stated that there was no compact age relationship with N_2O, which was a core justification for the use of these correlations but their result has not prevented subsequent use of of this tracer as an age proxy in the literature. The compact relationships amongst multiple tracers tell us that tracer isopleths (lines of constant VMR) tend to move together. Therefore, these figures show that the tracers are dynamically controlled, as chemical control gives curved relationships (unless chemical loss rates of the two species are identical). The degree of compactness of the relationship arises from the rapidity of the mixing (and, of course, random noise on the measurements).

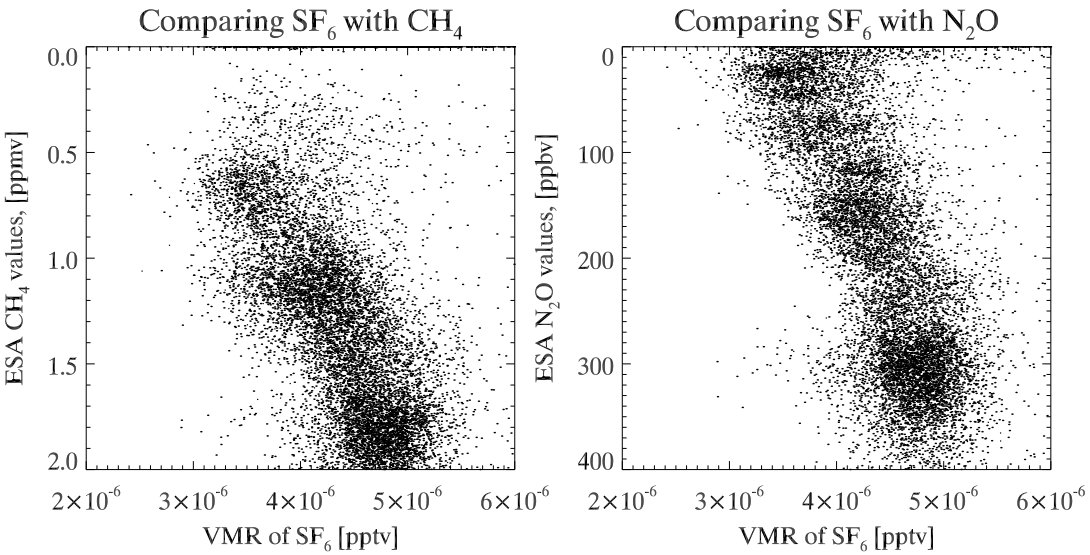

Figure 5.17: SF_6 correlations with ESA operational CH_4 and N_2O

5.5.4 Comparison against External Measurements

Observed vertical profiles of SF_6 from balloon (Patra et al., 1997), ATMOS (Rinsland et al., 1993) and recent ground-based measurements (Rinsland et al., 2003), give an indication of the expected vertical distributions. These are similar to our results to about 20-25 km. One such balloon measurement is shown in Figure 5.18. There is no prior global measurement; the best previous latitudinal coverage comes from ship campaigns (Geller et al., 1997). The ground-based measurements suffer from significantly broader weighting functions than the limb instrument offers, of the order of 10–15 km. Conversely, the limb instrument does not nominally measure below 6 km and is susceptible to cloud along its optical path.

Detrending

It is very clear from the previous figure that there is a strong bias towards the a priori at the topmost levels. This is entirely expected and manifests itself more strongly than for OCS due to the weaker nature of the SF_6 signal. As discussed in Section 3.4.1,

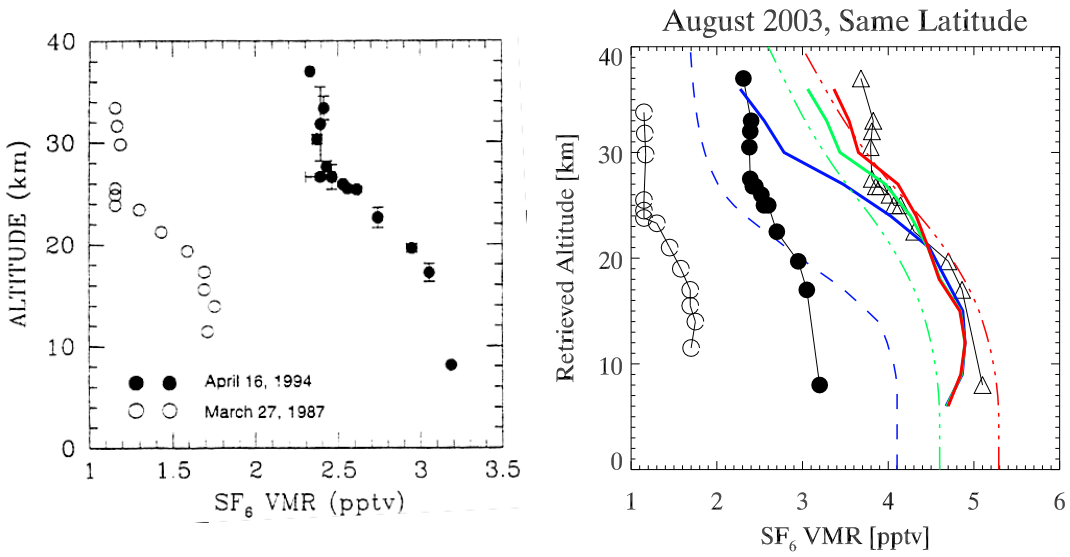

Figure 5.18: [Left] Two measured profiles for SF_6 in the atmosphere, showing the rapid increase in mixing ratio with time and the expected vertical structure into the stratosphere. These profiles were measured from a balloon, not a satellite instrument, Patra et al. (1997). [Right] The result of combining approximately 1,000 MIPAS measurements, from the same latitude / longitude region (17°N, 78°E). The literature values are repeated with the same symbols, and the 1994 profile is scaled by 6% yr^{-1} through to 2003 (hollow triangles). The heavy blue line shows the MIPAS result, with the dashed line representing the a priori. The effect of removing the prior information and replacing it with an a posteriori estimate (dashed lines) is also shown (green, red).

there are several ways to reduce or remove the influence of the a priori in the mean. One must be aware, however, that the implication of a high a priori contribution is that there is very little information in the measurement at these higher altitudes. In addition to validation, Figure 5.18 showed the effect of replacing the a priori used for the retrieval ($\mathbf{x}_a$) with an improved estimate ($\mathbf{x}_b$, green dashed line), using Equation 3.41. It is possible to construct this new a posteriori estimate using the results of an initial retrieval, and the red lines in the figure show the a priori profile that minimises the difference between mean result and a priori above 21 km, without changing any other parameters. It is also possible to have a latitudinally variable 'optimised' $\mathbf{x}_b$, but this has been rejected as being prone to inducing non-constant biases in the results. All subsequent figures contain data that has been detrended by use of this single new

$\mathbf{x}_b$ profile (and associated covariance $\mathbf{S}_b$). The most important point to note is that at low altitude, where there is a good amount of information from the measurements, the differing $\mathbf{x}_b$ values have almost no effect. The influence is almost exclusively in the regions of low information content.

5.6 Climatologies

One of the major uses of global SF_6 values is in model validation — such as Chemical Transport Models, Global Chemistry Models and Global Circulation Models. This is because SF_6 acts as an inert tracer that helps validate the dynamics. As a result, the generation of mean monthly atmospheres is necessary, and provides a valuable resource. These may be loosely thought of as climatologies, although based only on one year of measurement. The zonal mean fields for solstice and equinox months (December 2002 to March 2004) are shown in Figure 5.19.

The main features are dynamical – the change in the tropical tropopause 'centre', which is only centred over the equator for the equinoxes, and the descent of polar air. Some finer structure may also be resolved, such as the transport of tropospheric air into the stratosphere either side of the tropical tropopause, although the statistical significance of the measurements makes a firm conclusion difficult. There is also the year-on-year increase in the amount of SF_6 in the atmosphere, as already discussed. This is just visible by eye in the figures as the colour scale only covers a few pptv. Cloud contamination is a constant problem, and is shown by unfilled squares, especially in the lower tropical troposphere and around the southern winter pole.

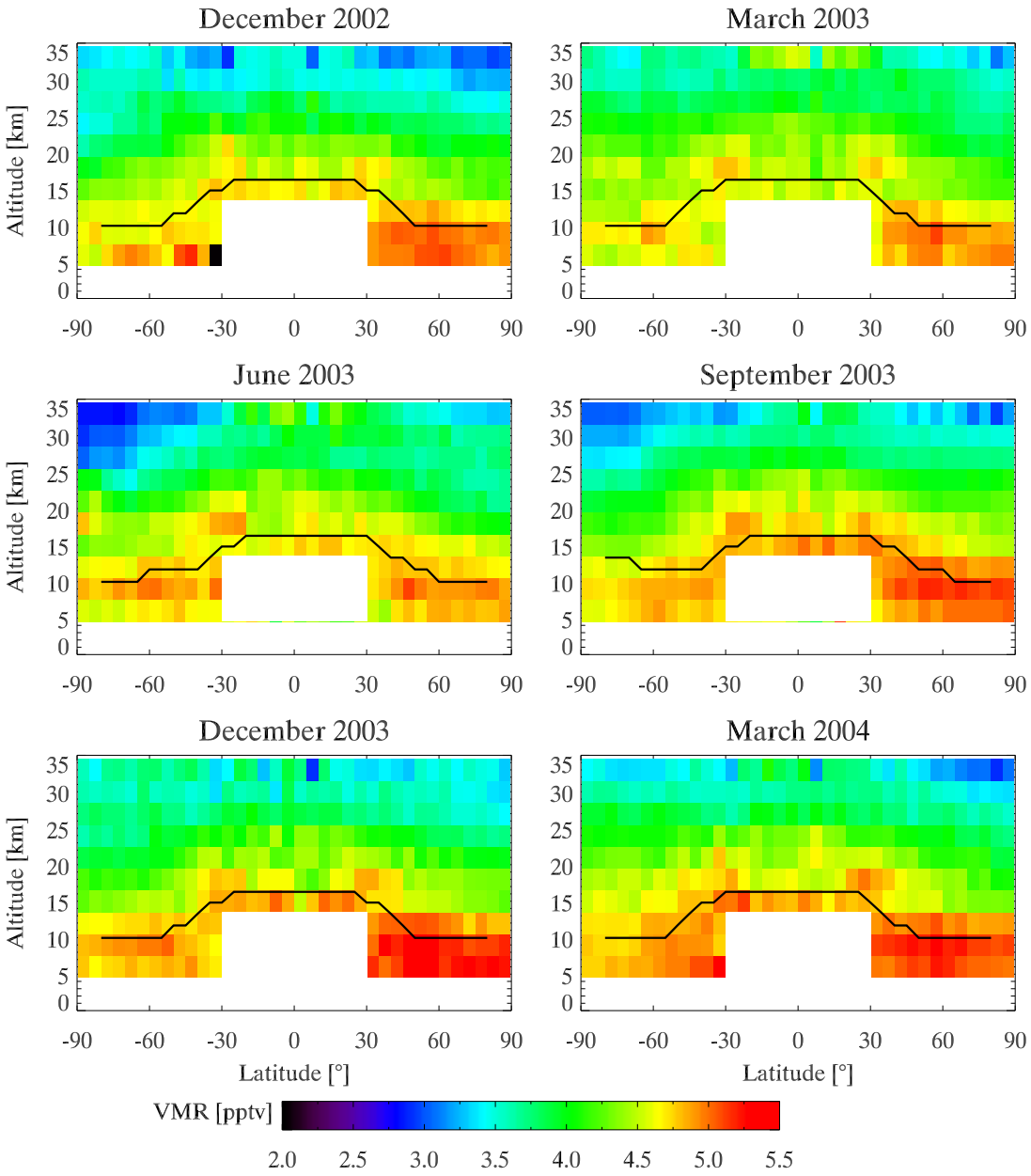

Figure 5.19: Zonal means for equinox and solstice months, December 2002 to March 2004. These allow the investigation of interannual variability (consistency of gross features) and seasonal trends (month-to-month variability).

5.7 Interannual Trend

The trend in the atmospheric VMR of SF_6, as outlined in the introduction, has been reported in many papers over the last 20 years. Making use of mean values from other

months, we estimate the trend from MIPAS measurements.

We looked at measurements up to 15 months apart, expecting an increase of the order of 0.5 pptv corresponding to previous trend estimates in the range 7–8% yr^{-1}, (Maiss et al., 1996; Rinsland et al., 1993). The variation within tropospheric values for a single orbit is approximately 0.5 pptv. Hence the means of multiple orbits were required to reduce the random component to less than 0.05–0.01 pptv — enough to be certain of distinguishing a trend with statistical significance.

The resultant mean tropospheric VMRs and calculated trend are shown in Figure 5.20, with data from the literature included. The global and hemispheric means for the MIPAS dataset are shown in Table 5.4. The standard deviations of the tropospheric monthly mean values are all less than 0.25 pptv, which includes the effects of both random error on individual measurements as well as global variability. The uncertainty on the means, due to the large number of measurements taken, is of the order 0.01 pptv in the stratosphere and 0.005 pptv in the troposphere.

Considering the global mean tropospheric VMR for monthly sets of orbits, we find a global minimum value for March 2003 (4.58 ± 0.001 pptv) and a maximum for December 2003 (4.82 ± 0.002 pptv). Other months, as expected, lie between these values in both data and mean VMR. A best fit linear regression of the six months sampled gives a trend of 0.30 ± 0.01 pptv yr^{-1}. This is shown in Figure 5.20. The absolulte mean values still contain spectroscopic systematic bias (Section 5.2.1), but as the spectral database was constant for all months, the trend estimate is unchanged.

We also observe a clear hemispheric difference, indicative of transport as already noted in the introduction, of between 0.1 and 0.2 pptv. This difference is only present in the troposphere. It is absent in the stratosphere, which is in line with our understanding of atmosopheric circulation and the entry of tropospheric air into the stratosphere through a well mixed region in the tropics.

Part of our observed trend may be due to the influence of systematic errors that were changed by one of several MIPAS processor upgrades upstream of our retrieval process between September 2002 and October 2003. However, during 2005 a concerted effort has been made to ensure that all available L1B data is consistently radiometrically calibrated. Nevertheless, the main systematic error components expected to affect the trend are those related to instrument calibration which might remain correlated for months. Fortunately, the MW error analysis (Figure 5.3) shows the dominant calibration error – 'GAIN' – to be a minor effect. There is good reason to believe that the resultant influence on the retrievals has been small, based on the observed consistency of MIPAS operational products routinely analysed at Oxford from July 2002. For example, the equivalent trend in retrieved methane (around 45°N) is $<$1% at 12 km over the same period. A long-term systematic error in the spectral radiances would be expected to perturb the retrievals of all species.

These values are lower than the older year on year trend estimates, but more in line with the most recent data from surface flask measurements by the National Oceanic and Atmospheric Administration (NOAA) Climate Monitoring and Diagnostics Laboratory (CMDL) of 0.24 pptv yr^{-1} (5% yr^{-1}) for the period 2000–2005 (Butler et al., 2005; Mondeel et al., 2003). Similarly, infrared spectroscopic measurements by Krieg et al. (2005) give trend values that range from 0.24–0.31$\pm$0.08 pptv yr^{-1} for various surface sites. It has been suggested that the rate of increase of emission has decreased over the last 5–10 years due to increased environmental awareness (Connell et al., 2000). As a result of this, attempting to fit a single trend that encompasses both the historic measurements from the early 1990s as well as current results may not be useful. This is explored in more detail in Chapter 8 which deals with using SF_6 as an inert tracer for calculating the age of stratospheric air.

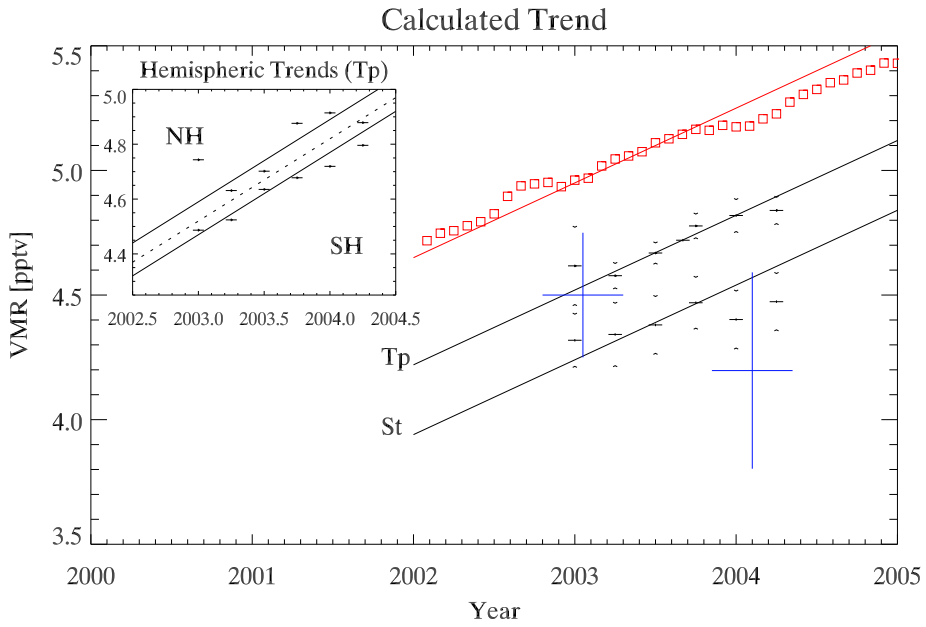

Figure 5.20: The trend in SF_6 VMR calculated from MIPAS measurements. The tropospheric (Tp) and stratospheric (St) global monthly means are shown along with best fit lines of 0.30 pptv yr^{-1}. Values based on literature remotely sensed measurements from other satellite instruments (ATMOS and ACE) as well as spectroscopic measurements from the surface are shown in blue (Rinsland et al., 2005; Krieg et al., 2005; Rinsland et al., 2003). Highly accurate surface flask measurements from NOAA/CMDL are shown as red squares (monthly means), with a best fit line (red) through the 2003 data only — corresponding to the central MIPAS measurements. The annual increase was the same (0.3 pptv) over this period for the two wholly independent measurements. The MIPAS data shows an almost constant offset that may be partially assigned to the 3–6% SF_6 spectroscopic error discussed earlier. This does not influence the calculated trend in any way. The finer variability observed in the CMDL data may possibly be replicated in the MIPAS measurements, where both show corresponding wintertime 'plateau' regions. The inset shows the hemispheric variability of MIPAS measured SF_6, about 0.12 pptv.

5.8 Conclusions

Because of its long lifetime and strong infrared properties, better knowledge of SF_6 looks to be of increasing significance in successfully modelling the radiative processes that govern our atmosphere and climate. SF_6 can also be used as a highly inert tracer for determining the age of stratospheric air.

Data from MIPAS is able to provide regular information on latitudinal VMRs and

Table 5.4: Trends in observed VMR over the MIPAS mission

Month	Troposphere			Stratosphere		
VMR (pptv)	NH	**Gbl**	SH	NH	**Gbl**	SH
December 2002	4.71	**4.60**	4.49	4.30	**4.32**	4.34
March 2003	4.63	**4.58**	4.52	4.32	**4.35**	4.38
June 2003	4.70	**4.67**	4.64	4.40	**4.39**	4.38
August 2003	4.87	**4.75**	4.69	4.43	**4.41**	4.38
September 2003	4.88	**4.78**	4.68	4.52	**4.48**	4.45
December 2003	4.91	**4.82**	4.72	4.40	**4.41**	4.42
March 2004	4.90	**4.84**	4.79	4.44	**4.47**	4.50
δVMR yr^{-1}	0.28	**0.24**	0.20	–	**0.12**	–
% yr^{-1}	6.0	**5.2**	4.4	–	**2.8**	–

on long-term trends. We have demonstrated the feasibility of profile retrievals in the range 6–30 km based on single scans, with 4–5 degrees of freedom for each profile. Averaging of multiple orbits to reduce random errors has been successful. A mean mid-latitude profile shows distinct tropospheric — 4.75$\pm$0.007 pptv, global variability (S.D.) 0.17 pptv, August 2003 — and stratospheric (4.41$\pm$0.008 pptv, S.D. 0.81 pptv) regimes, similar to accepted values. This global mean stratospheric loading contains an inter-hemispheric variability of the order of 0.1–0.2 pptv, giving an inter-hemispheric exchange time (troposphere) of approximately one year. Finally, we have shown the continuation of acknowledged global trends in atmospheric concentration, placing our estimate at 0.30$\pm$0.025 pptv yr^{-1}.

It has been possible to build on SF_6 trends reported during the 1990s, for example Harnisch et al. (1996) and Figure 5.20. Using the results from MIPAS retrievals, new data points for 2003 have been added that give more information about the trends.

SF_6 is at the borderline of detectability using the nominal retrieval methodology of one scan sequence to one profile. However, initial studies into statistical treatments of the results have revealed underlying profiles that differ consistently from the assumed

climatology. This deviation is in excellent agreement with published trends, and as such is a useful piece of external validation and verification of the retrieval accuracy.

Chapter 6

Sulphur Dioxide

The target of this chapter is sulphur dioxide, SO_2, once again a special case for retrieval. The SO_2 profile does not decrease monotonically with height. In addition, the emission features are even weaker than the previous species and there is a high degree of variability in abundance. For a single spectrum the lines are not visible above the noise of the instrument and, in addition to this, the spectral range contains a number of interfering species.

6.1 Introduction

Sulphur Dioxide is an acidic gas with both natural and anthropogenic origins. It is of interest to scientists due to its close links with aerosol formation and acidification of precipitation in the troposphere. Like OCS, it is directly involved in the formation and maintenance of SSAs.

The molecule is of point group C_{2v} and it has IR-active vibration-rotation bands at 1151 cm^{-1} [symmetric stretch], 1362 cm^{-1} [asymmetric stretch] and 512 cm^{-1} [symmetric bend]. Of these IR modes, the two stretching modes are within the spectral

range of the MIPAS instrument, and are shown in Figure 6.1. Isotopic variants are not present in detectable amounts.

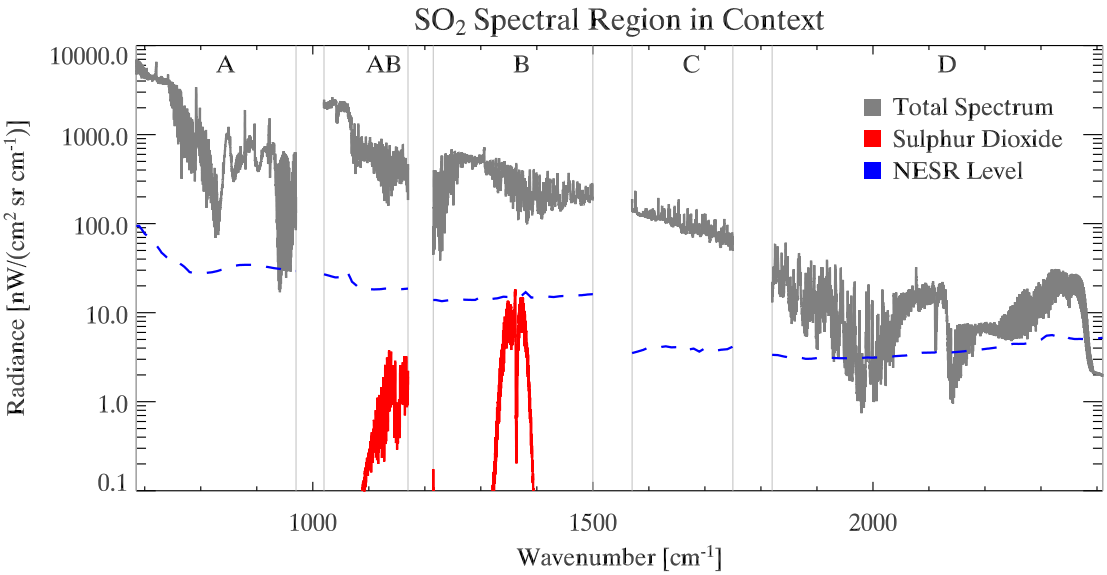

Figure 6.1: A radiative transfer simulation of the relative intensity of SO_2 features compared to the total radiance for a 12 km tangent altitude, based on estimates of mean climatological abundances. The instrument noise level (NESR) is shown as the dashed horizontal line.

6.1.1 Chemistry and Distribution

SO_2 forms a major part of the sulphur cycle processing in the Earth's atmosphere, and this is shown in Figure 6.2. Gaseous SO_2 reacts rapidly with OH radicals to form HSO_3. This, in turn, reacts with molecular oxygen, O_2, to from SO_3. Both these species are soluble in clouds and aerosol droplets, and are able to react to form sulphuric acid, H_2SO_4, Wayne (1999).

In general, the maximum concentration of SO_2 is close to its source and the amount of SO_2 decreases rapidly with distance — both vertical and horizontal. This indicates a short tropospheric lifetime (of the order of a few days). In the dry stratosphere,

especially low down where the concentration of OH radicals is small, the lifetime for SO_2 rises to the order of several weeks, Seinfeld and Pandis (1997).

Direct injection of SO_2 into the stratosphere by volcanic activity results in the formation of stratospheric aerosols. At higher altitudes, photolysis of H_2SO_4 aerosols leads to an increase in SO_2 in the upper stratosphere, Weisenstein et al. (1997); Rinsland et al. (1995). Unlike OCS and SF_6, the more prominent position of SO_2 as an atmospheric pollutant means that a good summary of the physical and chemical processes occurring in the atmosphere may be found in many textbooks, for example, Wayne (1999); Warneck (1988); McEwan and Phillips (1975).

In the atmosphere, sulphur dioxide is present at greatly variable volume mixing ratios. It has a minimum of approximately 10 pptv in the lower stratosphere, rising to 100 pptv by 60 km, Remedios (1999). The recent atmosphere is thought to contain less SO_2 than literature measurements from the mid 1990s due to the absence of recent large volcanic events. The tropospheric variability of SO_2 is much greater, with a strong anthropogenic influence mainly from use of fossil fuels. It ranges from less than 1 ppbv (clean continental air) to 100s ppbv (industrial) depending on latitude and season. An estimated mean climatological profile is shown in Figure 6.3. A zonal mean field of modelled tropospheric values is shown in Figure 6.4, showing the variability in the distribution of SO_2.

The large anthropogenic component can be clearly seen in country and continental scale SO_2 column density maps. An example of summer and winter column amounts is shown in Figure 6.5, which originates from model initialisation fields that make use of aggregated data.

Large volcanic eruptions can dominate both tropospheric distribution and loading. They are also able to inject large quantities of sulphurous material into the stratosphere if the eruption is of sufficient magnitude. For example, the eruption of Mt. Pinatubo

in the Philippines in June 1991 injected over 20 million tonnes of sulphur dioxide into the lower stratosphere and the resulting plume was tracked by satellite as it made its way around the globe, Bluth et al. (1992).

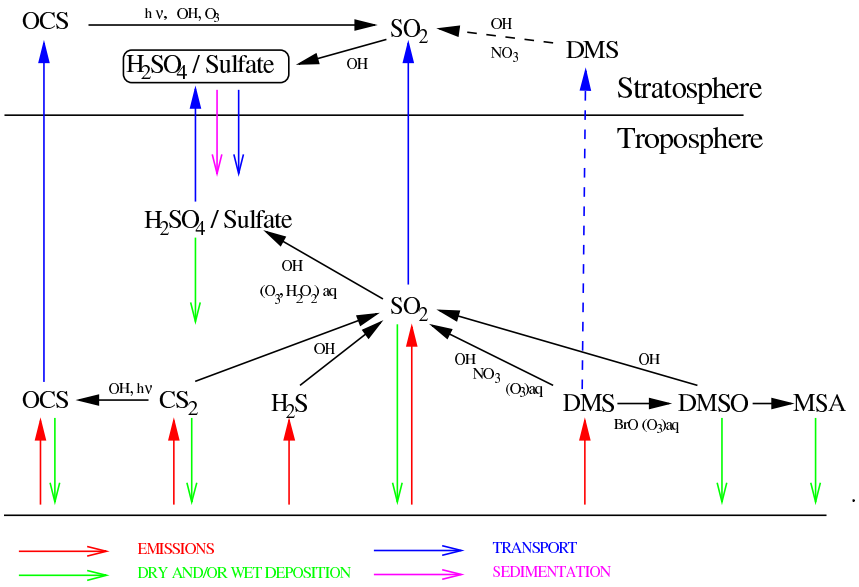

Figure 6.2: The position of SO_2 in the atmospheric sulphur cycle, from WMO (2002).

6.1.2 Previous Satellite Measurements

Due to the interest in sulphur dioxide, from scientific and environmental perspectives, there is a long history of its detection by remote-sensing techniques. A good example of an earlier satellite instrument is TOMS – the Total Ozone Mapping Spectrometer (1980s-1990s), designed to investigate ozone. However, the measurements obtained from these earlier instruments have generally been column amounts. The same is true for more recent instruments, such as GOME (ERS 1 & 2, 1990s) and SCIAMACHY (Envisat, 2002 to date). The advantages in column measurements lies in the better signal-to-noise ratio — a consequence of viewing through the bulk of the atmosphere down to the surface. However, only a vague idea of vertical distribution

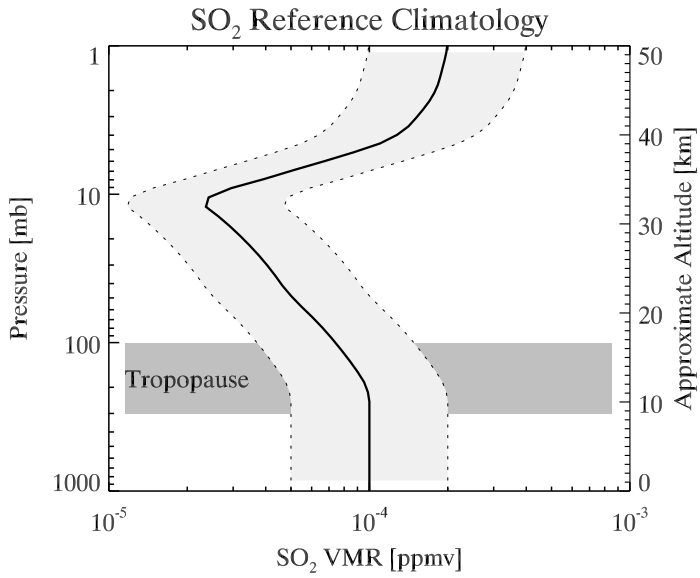

Figure 6.3: Climatological sulphur dioxide profile and its associated uncertainty. The approximate location of the tropopause is shown by the shaded region and both pressure and corresponding altitude are shown on the axes. The increase in VMR above 30 km arises from sulphuric acid photolysis. The lack of latitudinal variability, as for the previous species, reflects the paucity of data more than the physical distribution of SO_2.

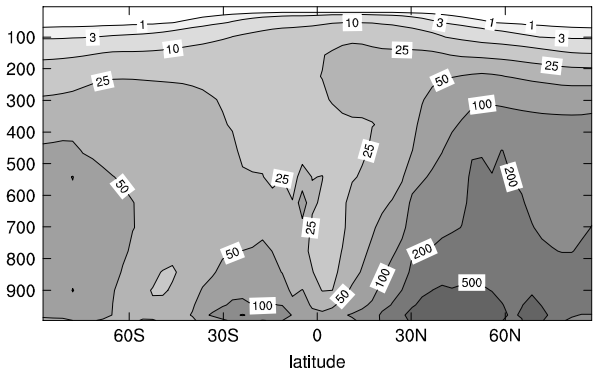

Figure 6.4: The modelled tropospheric SO_2 distribution shown as a zonal mean averaged over the year, from Rotstayn and Lohmann (2002). The vertical ordinate is in pressure (mb) and the contour levels are marked in pptv. The corresponding altitudes and pressures are approximately 450 mb–6 km, 300–9, 200–12 and 150 mb–15 km.

can be achieved from the weighting functions, which are inherently broad for nadir instruments.

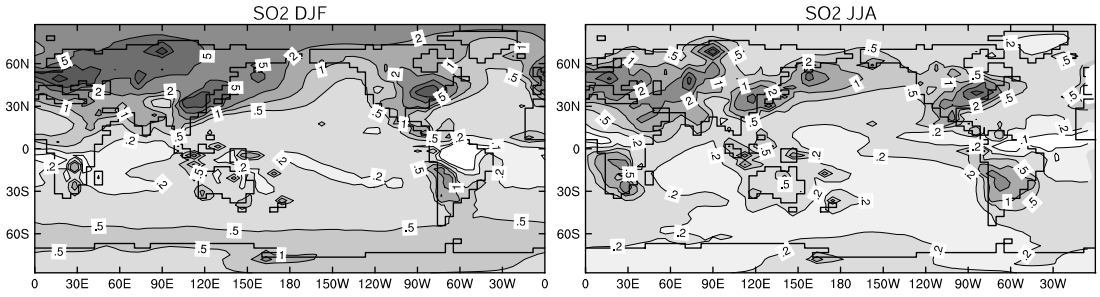

Figure 6.5: Winter and summer global SO_2 column values showing the strong anthropogenic influence on SO_2 abundance, from Rotstayn and Lohmann (2002). The contours are in units of mg S m^{-2}. Winter energy generation is responsible for the large seasonal difference.

High levels of SO_2 have been measured in the lower stratosphere by ultraviolet (UV), infrared and microwave techniques, shortly after the massive eruption of Mt. Pinatubo in June 1991, Bluth et al. (1992). Other volcanic and anthropogenic events have also been studied, in column, using GOME data, Eisinger and Burrows (1998).

The first orbital IR limb measurements of sufficient accuracy to investigate SO_2 profile distribution probably came with ATMOS (1985, 1992, 1993), a sun occultation Fourier transform spectrometer flown on the space shuttle. The advantage of an occultation instrument lies in its very good signal-to-noise. Unfortunately, this is combined with poor coverage over a limited latitudinal range. The short flight time of the shuttle compounds this problem. The results for sulphur dioxide were compared with a model that incorporated sulphuric acid photolysis at high altitudes, for wide latitudinal bands where the spectra had been co-added, Rinsland et al. (1995). This and many other papers demonstrated a clear stratospheric enhancement in SO_2 as a result of Pinatubo, and a subsequent decrease with time as the SO_2 is removed from the atmosphere.

The retrieval methodology applied to SO_2 to date has not really made use of the optimal estimation approach. It has generally been the computationally cheaper ‘least squares’ cost function that is to be minimised by the retrieval (discussed in Chapter 2), or basic variants on the ‘onion peeling’ approach that do not optimally fit the profile to

all levels.

6.1.3 Applications and Initial Work

There has already been interest in the results of MIPAS-derived SO_2 profile data from members of the atmospheric modelling community, both for model validation and for fine-tuning global distributions with the latest values (stratospheric SO_2 concentration is not constant and diminishes if there have not been major eruptions).

A second group that has shown interest are vulcanologists, interested in plume size, sulphur content and other characteristics. However, the spatial resolution of MIPAS is not sufficient for this role, although the resolution of the plume profile itself is expected to be far superior to measurements by satellite nadir instruments, such as GOME. Indeed, work has been presented on MIPAS observations of the autumn 2002 eruption of Mt. Etna, Italy, Burgess (2003). The nominal retrieval approach, of one measurement set to one profile was used. An enhancement at the 6 km level was observed for an overpass whose view geometry corresponded to a direct measurement of the atmospheric volume containing the volcanic plume. This measurement coincidence was confirmed by use of satellite imagery and wind fields. Measurements of the same air volume the previous week consistently showed no enhancement. The main conclusions from the work was that retrieval of single profile information from MIPAS is feasible only when there is significant volcanic enhancement of at least 10 – 100 times the background tropospheric values. This is exactly the situation when a volcanic plume is directly observed within the MIPAS field of view.

Finally, an application of satellite remote sensing instruments to volcanic monitoring has been suggested by several groups. This arises due to difficulty by which in-situ measurements can be made, as many volcanoes are in remote areas and have a habit of erupting unpredictably. This application is suggested in Eisinger and Burrows (1998)

who observed two volcanoes in column measurements. Similarly, an attempt to use 'TOMS data for Volcanic hazard mitigation' has been made, Bluth (2003). It is unlikely that the computational investment required to process MIPAS data in real-time in order to detect volcanic events as they occur would be well-spent.

6.1.4 Residual Error Correlation

An alternative suggestion has been made to make use of the residual data from operational species retrievals to look for large divergences from climatological values in small geographic regions. This technique is known as residual error correlation (REC) analysis. It is discussed in more detail by Jay et al. (2001). In the first instance, the REC approach is designed to look for systematic problems with the retrieval of the core operational species, by looking for persistent signatures in the residuals of the retrievals. The residual is the difference between measured and modelled radiances, once the retrieval has converged.

As long as spectral features of a minor species, such as SO_2, are present in one or more of the operational microwindow regions, it will be possible to indirectly determine how much is present in the atmosphere. As part of the operational forward model makes use of estimated climatological profiles for the unretrieved minor species, the residual should contain a signature radiance that corresponds to the difference between the climatological and actual SO_2 mixing ratios (as well as other non-retrieved species and random noise).

The benefit of this approach is the negligible computational resources required for comparing a single mean residual against a reference spectrum of known gas concentration. As a result, this REC method was thought to be suitable for the routine monitoring of volcanic eruptions in remote areas. An increase in SO_2 in a small region would be a strong indicator of an eruption. This would allow detection and further

observation at short notice, even in remote areas.

Unfortunately, even though some operational microwindows, such as ozone, overlap with the general SO_2 region, they are not optimised for sensitivity to SO_2. As a result, no clear residual attributable to SO_2 was found.

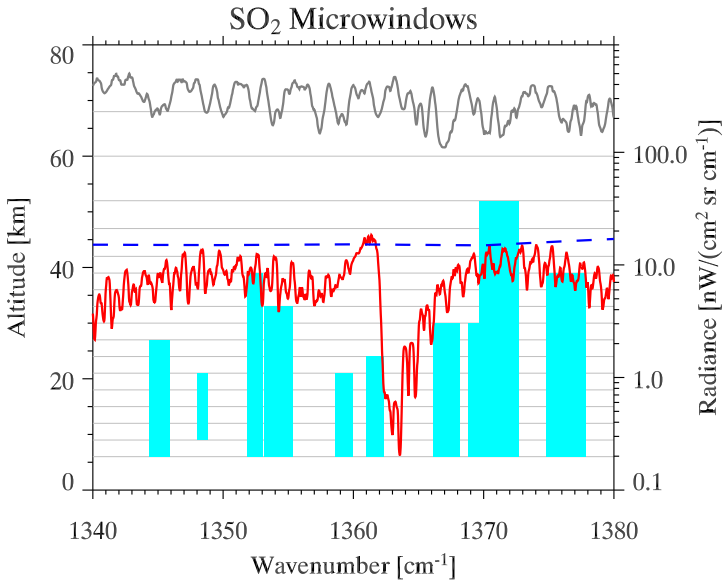

Figure 6.6: Plot indicating the position and altitude range (shaded blocks, left axis) of the selected microwindows, overplotted with the total radiance (grey, right axis) within the significant spectral region for a 12 km tangent height. The lowermost red line shows the radiance contribution from SO_2 to this total radiance. The MIPAS nominal measurement altitudes are shown as pale horizontal lines and the NESR as the horizontal dashed line.

6.2 Microwindow Selection

The feasibility study and subsequent selection of microwindows for SO_2 was similar to the previous species. The position of the ten selected microwindows is shown in Figure 6.6 and they are listed in Table 6.1. There are two classes of microwindow in terms of information content, the first five being much higher than the second five. The growth in information with number of microwindows is shown in Figure 6.7.

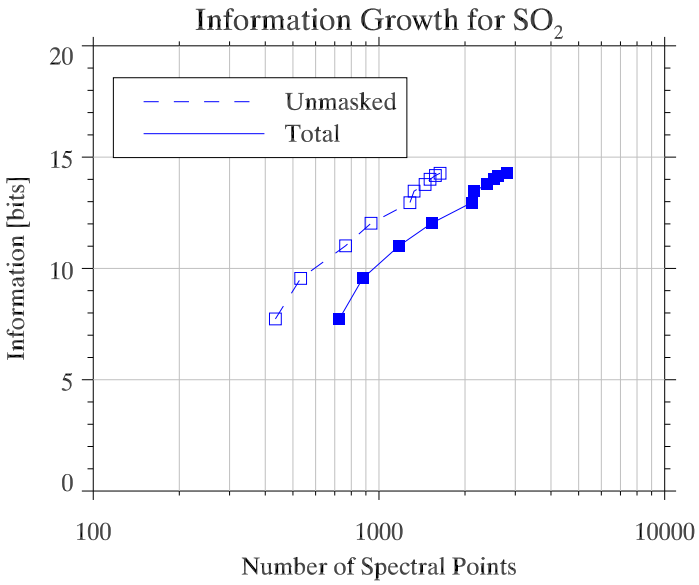

Figure 6.7: The information gain (bits) is plotted against the number of points required, on a logarithmic scale. As the number of spectral points contained in the set of microwindows increases, do does the total information retrieved on the target species. For SO_2 a set of ten microwindows was chosen, giving an estimated 14 bits of information. considering both the bands within the MIPAS spectral range, and assuming that retrieval is possible over all 17 levels, then there is a very large maximum of 136,000 spectral points for SO_2 on this figure. With an initial uncertainty of 100%, this gives an absolute maximum of approximately 20–25 bits of information, although this value would never be reached in practice.

Figure 6.8 shows the error analysis for a retrieval with nominal noise characteristics of 15 nW/(cm^2 sr cm^{-1}).

6.2.1 Microwindow Validation

A similar procedure to OCS and SF_6 was followed to check for sensitivity to various retrieval parameters. An idealised single scan retrieval and its averaging kernel is shown in Figure 6.9. The broad nature of this ideal, noiseless results highlights the difficulty of the SO_2 retrieval. The averaging kernels show that there is very little vertical resolution, even though it is a limb instrument. There are less than 2 degrees of freedom over the 50 km profile extent, with the majority of this information concentrated

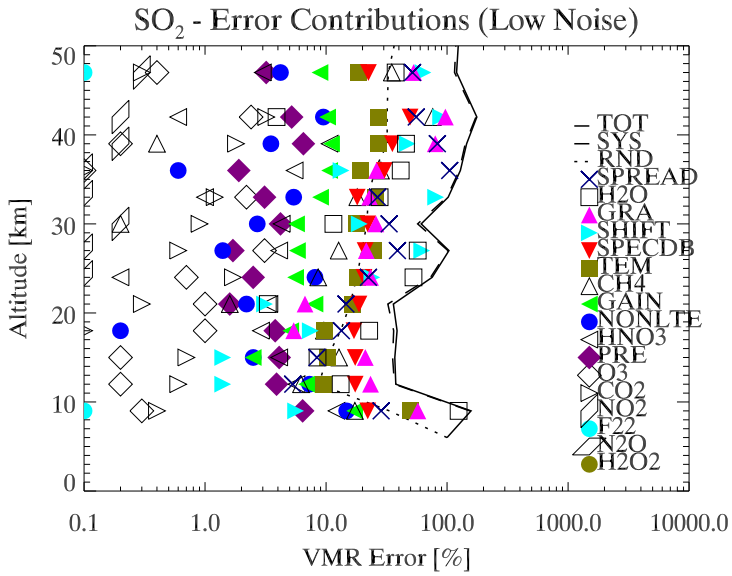

Figure 6.8: Assignment of various error sources to the final error budget as calculated during microwindow selection. The total error is shown (solid line) together with the random error component (dotted line) based on the instrument NESR. The total of the systematic error contributions is also shown (dashed line). The full list of possible error terms was defined in Chapter 2. The a priori uncertainty was assumed to be 100%.

Table 6.1: The ten best sulphur dioxide microwindows.

Microwindow	Band	Spectral Range (cm^{-1})	Altitude Range (km)
SO2_0101	B	1369.675 – 1372.675	6 – 52
SO2_0102	B	1361.025 – 1362.350	6 – 24
SO2_0103	B	1366.100 – 1368.150	6 – 30
SO2_0104	B	1353.150 – 1355.325	6 – 33
SO2_0105	B	1374.850 – 1377.850	6 – 39
SO2_0106	B	1348.150 – 1348.700	9 – 21
SO2_0108	B	1351.875 – 1353.050	6 – 39
SO2_0107	B	1358.575 – 1359.950	6 – 21
SO2_0109	B	1368.875 – 1369.500	6 – 30
SO2_0110	B	1344.350 – 1345.925	6 – 27

in the lower atmosphere. The effect of the a priori correlation length is significant because the profile is not monotonic. The minimum value in the mid stratosphere will be

poorly represented if there is a long correlation length (corresponding to strong vertical smoothing). For these tests, the correlation length was set to 1 km.

The sensitivity of the microwindows to changes in SO_2 VMR is shown in Figure 6.10. These results are not encouraging.

To understand the problem, especially in the mid stratosphere, consider the abundance of SO_2. A VMR of 10 pptv corresponds to approximately 6.4 kg (100 moles) of SO_2 in the $300\times\ 30\times\ 3 = 27{,}000$ km^3 view volume of MIPAS at 30 km (10 mb). This is about 0.25 g per cubic kilometre.

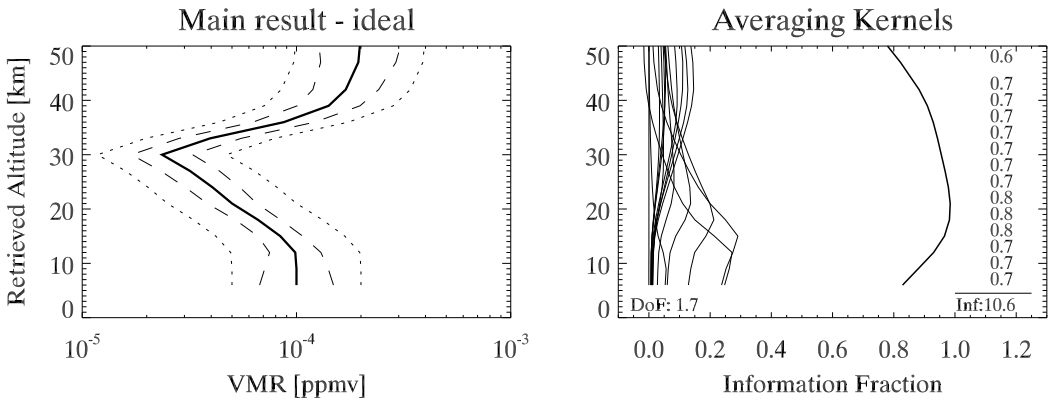

Figure 6.9: Retrieved profile and averaging kernel for an idealised simulated retrieval based on a mid-latitude daytime atmosphere with spectral noise level set to 15 nW/(cm^2 sr cm^{-1}). The a priori uncertainty was set to 100%. Diagnostic information, including the averaging kernels, is shown on the right. The degrees of freedom in this profile, of fourteen levels considered, are shown on the bottom left of the averaging kernel figure. The Shannon information gain for this retrieval is shown bottom right, with a level by level breakdown above.

6.3 Coaddition

The predicted SO_2 retrieval is sufficiently poor that other approaches need to be considered. Whereas before our strategy involved the retrieval of individual profiles in isolation, followed by some form of post-retrieval coaddition and correction, the random noise on the radiances is now dominant over the signal. As a result, the signal

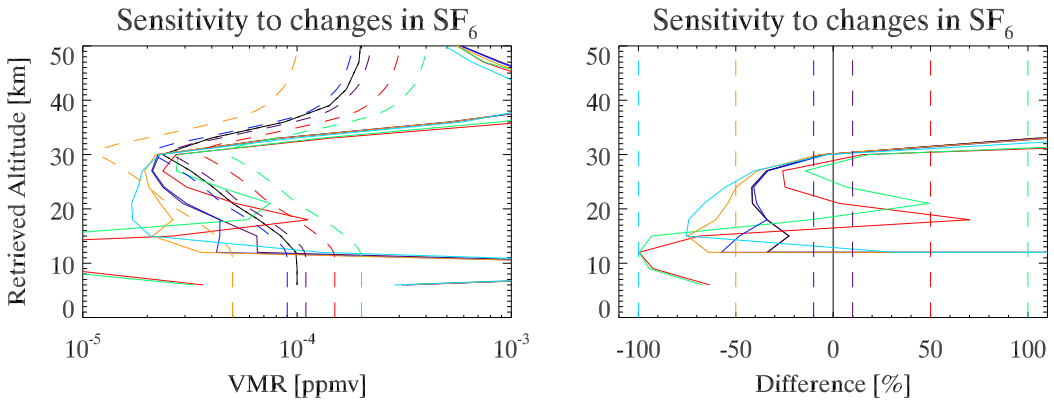

Figure 6.10: This plot shows the percentage deviation from the profile used to simulate the spectra that the retrieval was performed upon. The same retrieval parameters were used throughout, with the same a priori. A set of six profiles were used: no SO_2, -50%, -10%, +10%, +50% and +100% of the climatological profile. The results show the sensitivity of the microwindows to changes in the amount of SO_2 in the atmosphere.

component of the retrieval target radiance needs to be improved. In Chapter 3, the various options for coadding before retrieval were discussed.

6.3.1 Radiance

Figure 6.11 shows the mean of around 100 radiances ($\bar{y}$) from nominal cloud-free (1.8 threshold) scans from August 2003. The radiances all originated from the same region of the atmosphere, 45 – 60° S, 0 – 30° W, in order to minimise the difference in atmospheric structure between measurements. A retrieval was then performed on these mean mid latitude spectra. The other parameters, such as the temperature, were set to the mean of the set of individual retrievals in the first instance and retrieved from the mean radiances in the second instance. Retrieving pT and water from the mean spectra gave a marginally improved result, and hence the results of this second method are shown in Figure 6.12.

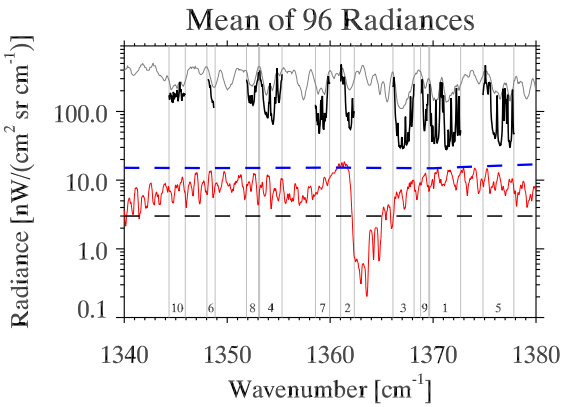

Figure 6.11: Result of coaddition in the spectral domain about the SO_2 microwindows at 12 km. The solid black line shows the mean radiance of 100 scans, chosen to have a similar geolocation and atmospheric state, overlaid on a simulated radiance for this altitude based on climatological values and without noise (grey line). The solid red line outlines the simulated radiance for a nominal SO_2 VMR and mid latitude atmospheric conditions. The noise level of an individual spectrum is outlined as the dashed line. Although the random noise is reduced by approximately 10 times the total increase in radiance from SO_2 that lies above the noise is modest. The position of the numbered microwindows are highlighted by the vertical lines.

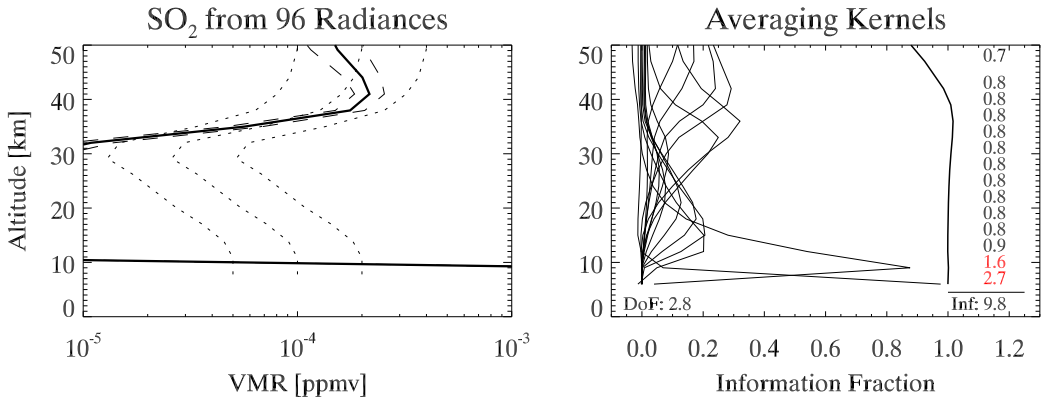

Figure 6.12: Retrieved profile (left) and averaging kernel (right) for a retrieval based on the mean radiances shown in the previous figure. The layout is as Figure 6.9. The lower noise associated with the spectra directly gives rise to improved information content and a larger number of degrees of freedom. This is most pronounced at higher altitudes, where the atmospheric variability is much reduced and the non-linear terms in the radiance coaddition are less dominant.

6.3.2 Residuals

Based on the work in Chapter 3, the next logical approach is to calculate some form of mean residual ($\bar{z}$) from which an idealised 'measurement' can be reconstructed, but

with lower random noise. Initially, a residual set for a single profile measurement was calculated by retrieving the key interfering species, but keeping the SO_2 profile fixed at the climatological value. The result of an arithmetic mean of a set of these residuals from many scans was then calculated. Independently, the forward model was used to calculate 'synthetic' spectra, using the mean retrieved values of all the interfering species, along with the climatological value of SO_2. The mean residual is then added to this synthetic spectra and a retrieval of just SO_2 performed, with the noise level set appropriately. In principle, the mean residual should contain all the small deviations of SO_2 VMR from the climatology, which will be mapped directly into the deviation of this final retrieval from the climatology. If the mean residual happened to be zero, then the climatological value of SO_2 would be retrieved (in a similar manner to the simulated retrieval shown previously in Figure 6.9). By removing the bulk of the SO_2 radiance from the residuals, the deviations that make up the residual should be as close to linear in radiance space as possible.

As an alternative approach, the residual is calculated assuming that the climatological abundance of SO_2 is zero. As a result the residual will contain the whole of the SO_2 residual signature along with the usual random noise and incorrectly modelled interfering species. The simulated radiance, likewise, is calculated without SO_2. The remainder of the method is the same. This approach is marginally less linear, but has the advantage that a much stronger SO_2 residual signature is produced.

The residual spectra from this approach are shown in Figure 6.13 and the subsequent retrieval from the synthetic radiance is shown in Figure 6.14.

6.3.3 Kalman Filter

The retrieval from the mean of a set of residuals is an improvement over adding individual retrievals. However, there is another way to combine the information from

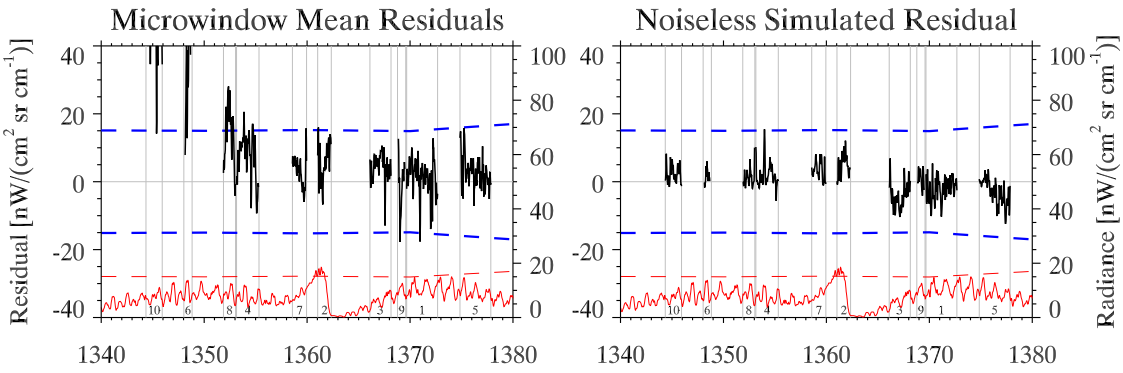

Figure 6.13: [Left] Result of coaddition of SO_2 microwindows residuals from 12 km. The solid black line shows the mean of 100 sets of residuals, with the noise level highlighted by the dashed lines (left axis, linear). The red lines outline the simulated SO_2 radiance and the noise level of an individual spectrum (right axis, logarithmic). [Right] Simulated SO_2 residual, in the absence of noise and incorrectly modelled interfering species, for the same altitude.

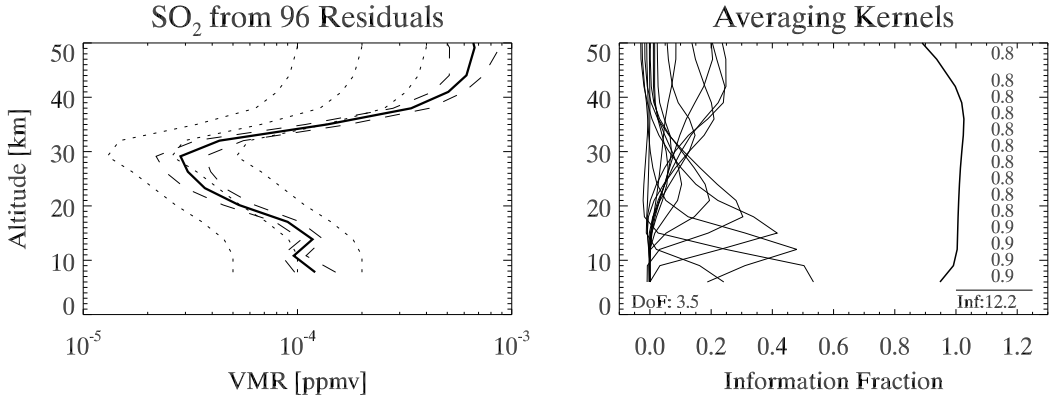

Figure 6.14: Retrieved profile (left) and averaging kernel (right) for a retrieval from the reconstructed mean residual spectra shown in the previous figure. Previously, pressure, temperature and other interfering species were calculated as the mean of the set of approximately 100 individual retrievals. The residual approach appears better in practice, in line with the discussion in Chapter 3.

multiple radiances. By choosing a sequence of measurements of similar atmospheric characteristics within a narrow geolocation, it is possible to use the resulting profile (and associated covariance) as the starting point of the next retrieval. In that way the prior information only enters the retrieval a single time. As each retrieval is performed, a small addition to the information content of the composite profile is made. At the

end of a hundred or so profiles, the random error on the final profile should be approximately a tenth that of an individual retrieval. This method is sensitive to faulty or weak cloud flagging, as a 'bad' retrieval partway through can shift the profile such that it takes many measurements to recover. The effect can sometimes be reduced by the addition of a 'relaxation factor', that slightly increases the covariance between steps to allow the subsequent measurement slightly more leeway.

This approach, in theory, deals better with anomalous profiles than the coadition of radiance or residual approaches. Figure 6.15 shows the evolution of a profile from the same dataset as the residual calculations in the previous figures. The majority of profiles cluster together as would be expected from a relatively small error covariance for their initial states combined with the noisy (uncertain) new measurements.

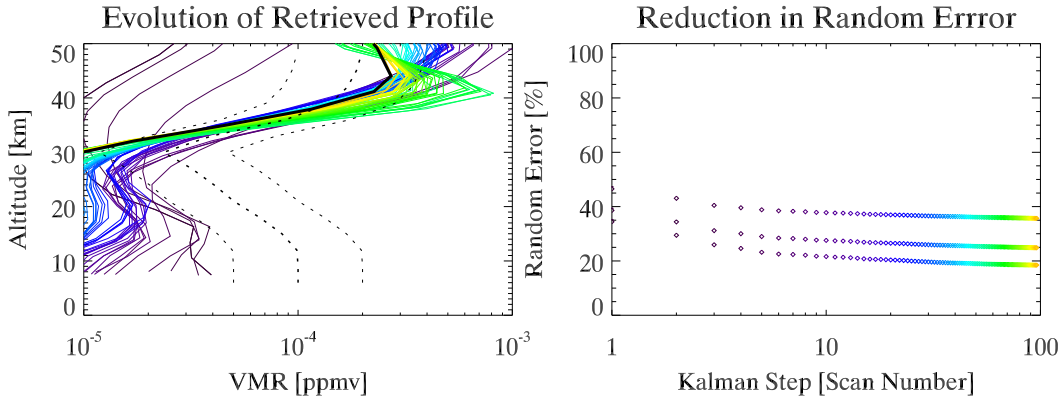

Figure 6.15: [Left] Evolution of the final profile over 100 steps, from purple (start) to orange (end). The final profile is shown as the heavy solid and dotted lines. The initial state is shown by the dotted lines.
[Right] Reduction in random error component as elements are added to the retrieval.

6.3.4 Mean Profiles

The original mean profile method ($\bar{\hat{x}}$) used in the previous two chapters was used to produce the profile in Figure 6.16. It used the same scans as in the residual and radiance approaches, above. The mean of large numbers of individual retrievals mainly

contiains prior information, although the lowermost levels retain some sensitivity to atmospheric state. A zonal mean by this method is also shown later in this chapter, displaying limited latitudinal sensitivity.

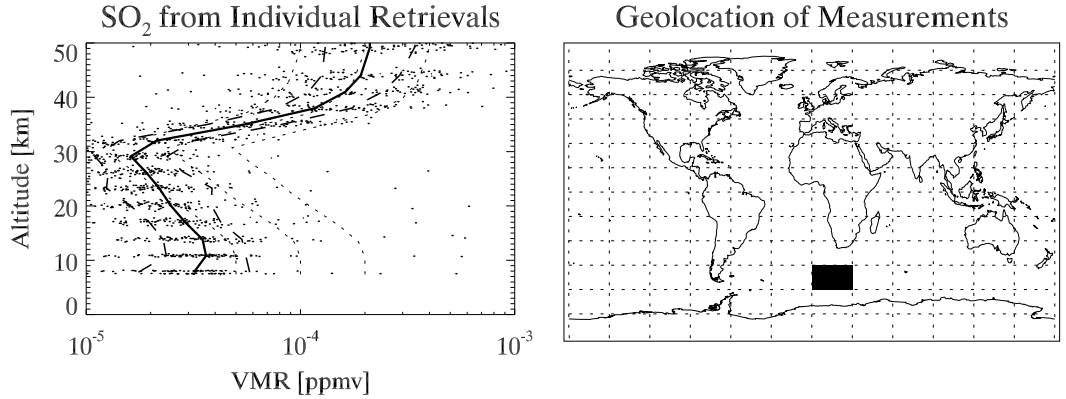

Figure 6.16: [Left] Result of coaddition of 100 individual retrievals corresponding to the radiances used in the various coaddition approaches. The average random error value is shown as the dashed lines and the scatter in the individual retrieved profiles (and hence standard deviation) is displayed as the clusters of dots at each level. The dotted lines show the a priori and its uncertainty. As with the previous species, the mean profile contains a significant prior information contribution. [Right] Geolocation of the chosen measurements for all methods.

6.4 Global Retrievals

The various retrieval methods were applied to a global distribution of measurements, on a $15\times30^\circ$ grid. This allowed the generation of zonal means and global maps, as for the previous species, for the four methods. Each can be compared against the tropospheric zonal mean in the introduction (Figure 6.4) and a different model run extending into the upper stratosphere, Figure 6.17. An additional model result from a different group is shown in Figure 6.18 for comparison, giving some idea of the variability observed between models themselves.

Figure 6.19 shows the MIPAS SO_2 fields from August 2003, for each of the four methods.

Mean Profiles

The features to notice include the almost uniform middle atmosphere (25–50 km), which probably indicates a high degree of prior information in the means, the high values at the south pole and the lower atmospheric shape that follows the tropopause. Although the tropospheric shape is good, with an associated high variability in line with the literature, the overall result appears too uniform and too close to the a priori. There is some significant information from the measurements in this zonal mean, but it is hard to separate from the a priori. Removing the a priori makes the result very unstable and replacing it does not improve the result due to the large natural variability. Experiments where the initial guess atmospheres were constant with latitude still gave an enhancement at the southern pole, so there is either a pronounced sensitivity to low temperature or to an interfering species whose distribution differs markedly from the climatologies in the perturbed region.

Mean Radiances

The mean radiance retrieval has not given satisfactory results. The method minimises the prior information in the result, but is very sensitive to small changes in atmospheric state between elements of the mean. The tropospheric shape is poorly defined and the areas of high variability and rapid changes in VMR in the middle atmosphere are thought unphysical.

Mean Residuals

This approach is much improved. The tropospheric VMRs are generally reasonable and the high values are only at latitudes and can be attributed to anthropogenic influences. High values at the southern pole are detected again, which may be evidence for

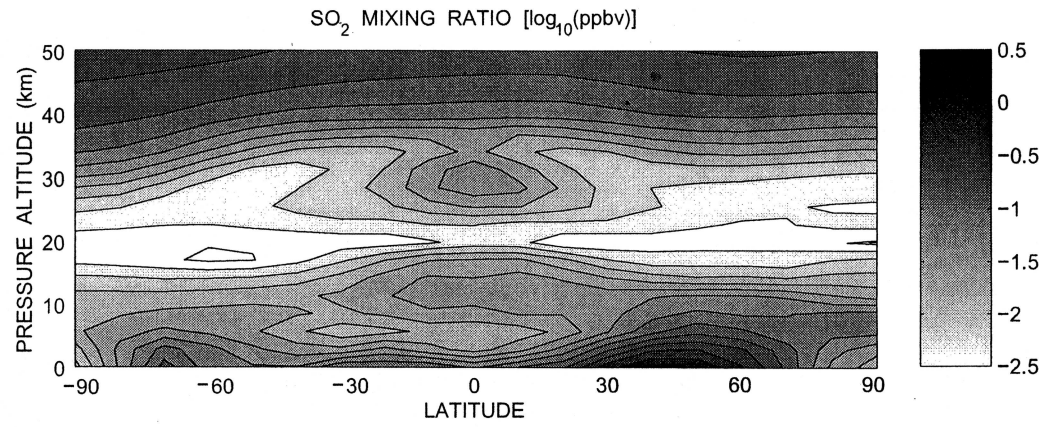

Figure 6.17: Modelled SO_2 zonal mean, Pitari et al. (2002). There is a clear anthropogenic hemispheric asymmetry. The log scale ranges from 3 ppbv to 3 pptv.

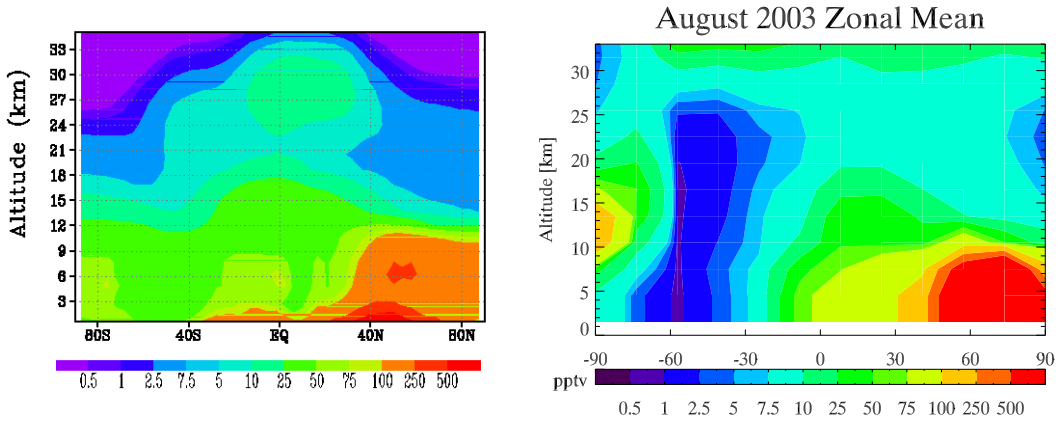

Figure 6.18: [Left] Another modelled SO_2 zonal mean, for June–August, Timmreck, (*Pers. Comm.*, 2003). [Right] August MIPAS result from the Kalman approach on same colourscale and similar altitude range. The MIPAS data from the 4.5–7.5 km bins have been repeated towards the surface to aid comparison.

a significant surface source – especially as there is not really a tropopause there at this time of year. The tropospheric shape is not well defined, but neither are the values unreasonable. The minimum VMRs around 25 km are higher than previous methods by a factor of two. In the middle atmosphere, the residual approach implies that previous measurements and models have significantly underestimated the quantity of sulphate aerosol that is photolysed, with 2–3 times as much SO_2 present in this region. This

result is potentially real, as the retrieval diagnostics (Figure 6.14) imply that there is good sensitivity at these upper levels, especially in comparison with the mean profile approach. The variability of this zonal mean is much lower and more uniform than previous approaches, except for in the region of known high variability (Northern mid latitude troposphere).

Kalman Approach

Although the most elegant method, and one of the simplest to implement in existing codes, there seems to be a minimum VMR required to correctly initialise the retrieval. The northern hemisphere shows good sensitivity, with a well defined troposphere, low variability in the middle atmosphere and consistency both vertically and, more importantly for validation, horizontally. The southern hemisphere — which has a lower tropospheric SO_2 abundance — appears to have converged on low tropospheric profile values. Indeed, this can be seen in Figure 6.15, which is in the southern hemisphere. The resulting tropospheric values of around 10 pptv is about 10 times lower than model and point measurements suggest, and 100 or more times lower than equivalent northern hemispheric measurements.

6.4.1 Anthropogenic SO_2 Sources

Figure 6.20 shows the retrieved global tropospheric distribution from the best two methods, the mean Residuals and the Kalman approaches. It can be compared with the global *column* distributions shown in Figure 6.5, although the bulk of the sulphur mass is below the 6 km level and the distribution will be better mixed.

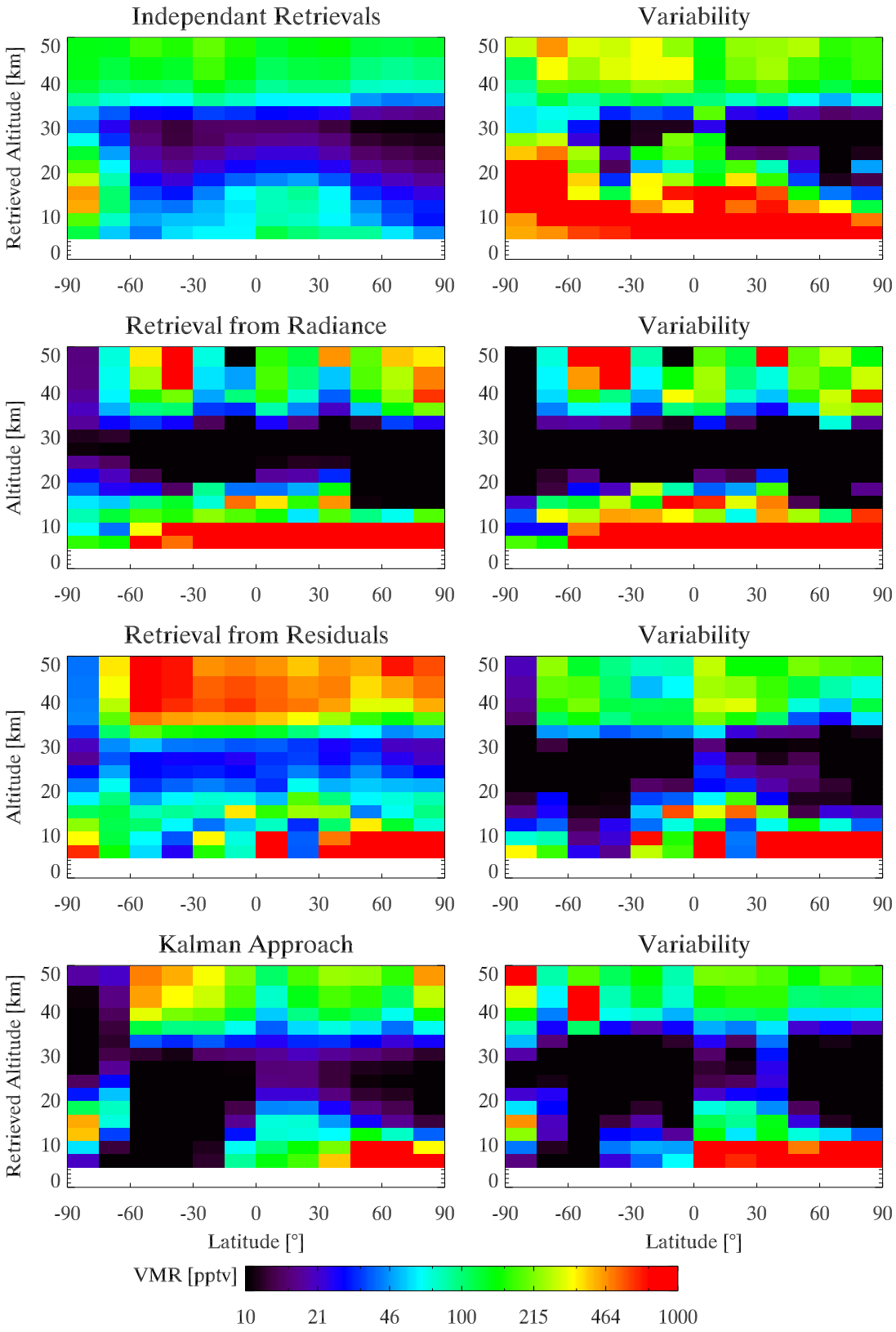

Figure 6.19: Zonal means (left) and standard deviation for the various retrieval approaches. In order, Mean Profiles, Mean Radiance, Mean Residual, Kalman.

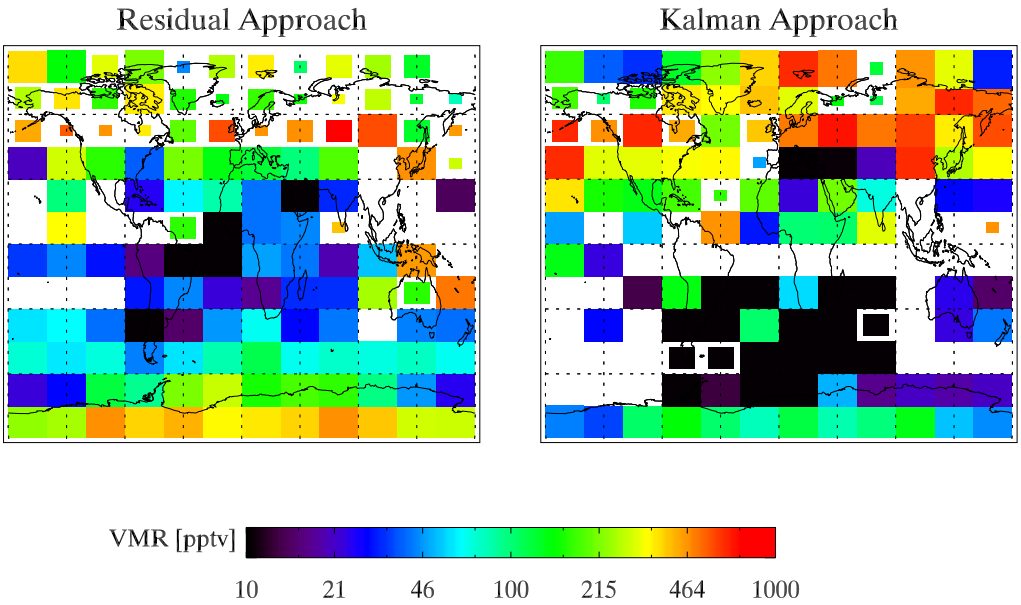

Figure 6.20: Retrieved global tropospheric distribution from two methods; [Left] Mean Residual and [Right] Kalman approach. Both plots share the same colourscale. The global plots are noisy but both show similar global scale atmospheric distributions, with a northern hemispheric enhancement.

6.5 Conclusions

SO_2 is at the borderline of detectability using the nominal retrieval methodology of one scan sequence to one profile. It can be retrieved by this method mainly when strongly enhanced, as in a volcanic plume. This chapter has explored more complex methods of retrieving this very weak species, and shown definite potential in both the 'Residual' and the 'Kalman' approaches. Initial zonal means, by a variety of methods, have been created and comapred with a common model mean. However, the moderate resolution — both spatial and temporal — coupled with the computational demand of both these new methods means that operational limb SO_2 detection remains unlikely.

6.5.1 Further Work

There are two areas for further investigation. Firstly, looking at the seasonal variability of the retrieved SO_2 distribution will allow additional validation. For example, there is an increase in northern winter SO_2 in the northern mid latitudes due to energy generation for heating. In addition, there are a selection of well-known surface sources, such as effusive volcanic eruptions, large cities and heavily polluting industry whose locations are well known. Detecting enhancement in SO_2 in the downwind plume would be a good validator of the retrieval as well as having direct applications in monitoring. Apart from validation, the generation of a seasonal climatology would be of interest to the modelling community. Unfortunately, it is uncertain if the product is able to be sufficiently validated to be of use.

Chapter 7

Ammonia

The final target selected has turned out to be the most challenging, although initial calculations indicated that ammonia should have been relatively simple to retrieve in the troposphere. This was due to an overestimate in the climatological concentration.

7.1 Introduction

Ammonia (NH_3) is a simple pyramidal molecule found in the lower atmosphere. It has two main absorbtion features in the thermal infrared, 700–1200 cm^{-1} (asymmetric) and 1500–1800 cm^{-1} (symmetric), which can be resolved into lines. These regions are shown in Figure 7.1. The range of mixing ratios in the troposphere ranges from 1 pptv to 1 ppbv depending on location and altitude, e.g. Bouwman et al. (1997). Ammonia plays a key role in the formation and composition of aerosols, though a variety of processes, many of which are poorly understood. The ammonium cation (NH_4^+) is readily formed by dissolution in water and is usually associated with nitrate (NO_3^-) or sulphate (SO_4^{2-}) anions. Consequently, the lower atmospheric residence time is short, less than 10 days (Seinfeld and Pandis, 1997). The resulting particles of ammonium

salts are very hygroscopic and are easily incorporated into aerosols. These salts also form part of the ionic mix to be found in cloud and rain. Both wet and dry deposition are major removal mechanisms for ammonia (Adams et al., 1999).

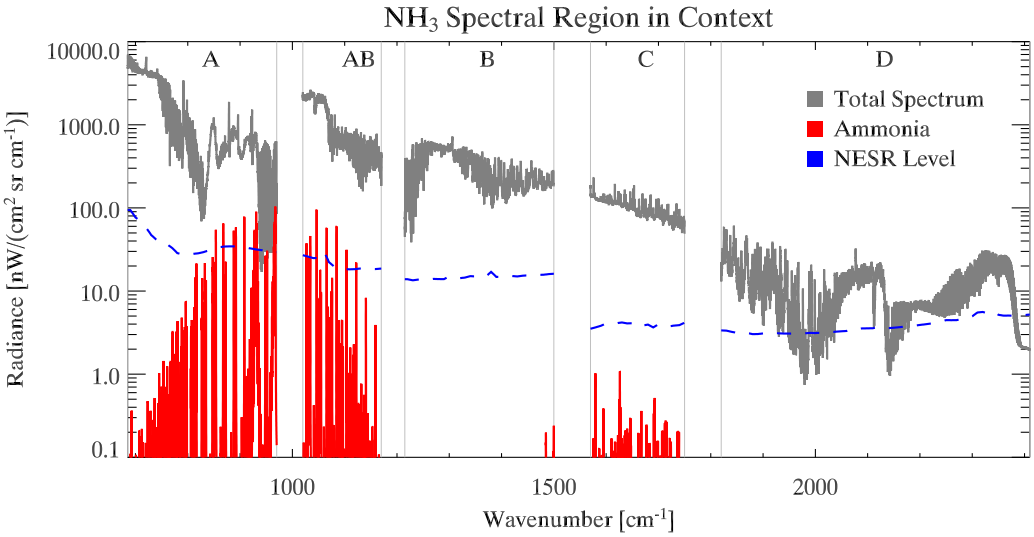

Figure 7.1: A radiative transfer simulation of the relative intensity of NH_3 features compared to the total radiance for a 12 km tangent altitude, based on the initial climatological abundance by Remedios (1999). The instrument noise level (NESR) is shown as the dashed horizontal line.

7.1.1 Sources and Sinks

Major natural sources include oceans, animal respiration and soil microbial processes. Significant anthropogenic sources of ammonia emissions are livestock, chemical fertilizers, waste management and industry (Wayne, 1999). For each of these sources there remain large uncertainties in the magnitude of emissions, the diurnal and seasonal variation, and the spatial distribution. As a consequence, there are large uncertainties in the formation of sulphate and nitrate aerosols (Asman et al., 1998).

Once released into the atmosphere, ammonia is eventually deposited as either gaseous ammonia or as the ammonium ion. The deposition of ammonia is a com-

plex process, thought to be in dynamic equilibrium with growing vegetation, which is able to act as both a source and a sink of the gas (Asman et al., 1998; Liao et al., 2003).

7.1.2 Chemistry

Ammonia is the most significant basic atmospheric gas and, after molecular nitrogen and nitrogen oxides, the most abundant nitrogen-containing gas in the atmosphere. The role of ammonia is accepted as a major contributor to secondary aerosol formation in the atmosphere (Wayne, 1999). Ammonia reacts rapidly with both sulphuric and nitric acids to form fine particles. Reaction of ammonia with sulfuric acid or ammonium bisulphate is favored over reaction with nitric acid. As a result, in regions of moderate to high anthropogenic sulphur emissions, the majority of aerosol ammonium is associated with sulphate ion (Seinfeld and Pandis, 1997). However, significant amounts of ammonium nitrate are formed in regions where sulphate levels are low and ammonia and nitrogen oxide emissions are high. The ammonium nitrate formed is thermally unstable and in dynamic equilibrium with ammonia and nitric acid. Since sulphate aerosols deposit much more slowly than either ammonia or nitric acid, the formation of ammonium sulphate aerosol serves to distribute the ammonia/ammonium over a much larger region than occurs when nitrate aerosol is formed (Liao et al., 2003).

7.1.3 Measurement

The accurate quantification of atmospheric ammonia is particularly challenging. Ammonia is a ‘sticky’ gas that readily adsorbs onto almost all surfaces. Much of the adsorbed material will subsequently desorb if ammonia levels decrease in the sample air stream (NOAA, 2000). Consequently, in-situ measurements are difficult to make and suffer from both under and over estimates of the true concentration. Remote sensing in

the atmosphere is equally difficult as the high reactivity of ammonia leads to very low volume mixing ratios in the free troposphere. Oelhaf et al. (1982) discusses one of the few literature NH_3 limb measurements. The rapid variability makes instrument noise and pointing accuracy and variability significant factors in the accurate determination of ammonia quantities.

The majority of previous ammonia measurements are concerned with the boundary layer and often consist of point measurements near to areas of local interest. Examples include monitoring of farm and industrial emissions as well as city pollution (Lan et al., 2004). Very little height-resolved information exists, due to the problems explained above.

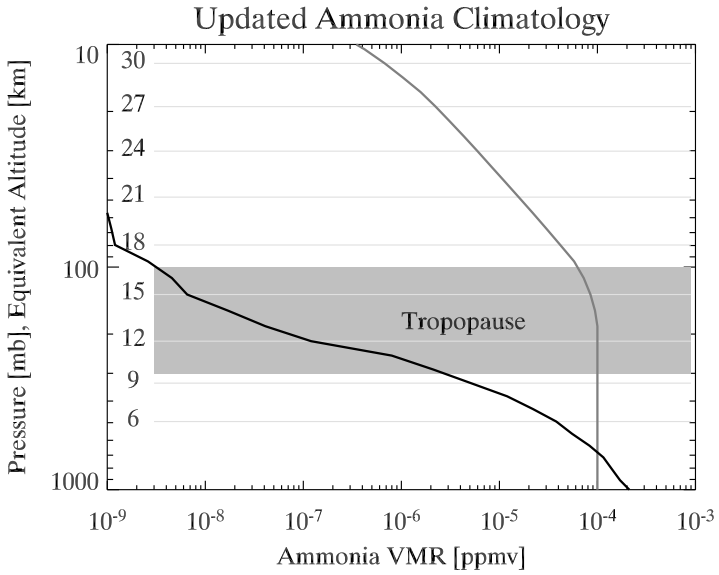

Figure 7.2: The ammonia climatology derived from results in this chapter (black line) compared with the original version (grey line), Remedios (1999). Only the lower atmosphere, to 30 km, is shown. There is neither latitudinal nor seasonal variation in either climatology. Ammonia is not well mixed (uniform tropospheric VMR) due to its very short lifetime and there is substantial variability within the boundary layer.

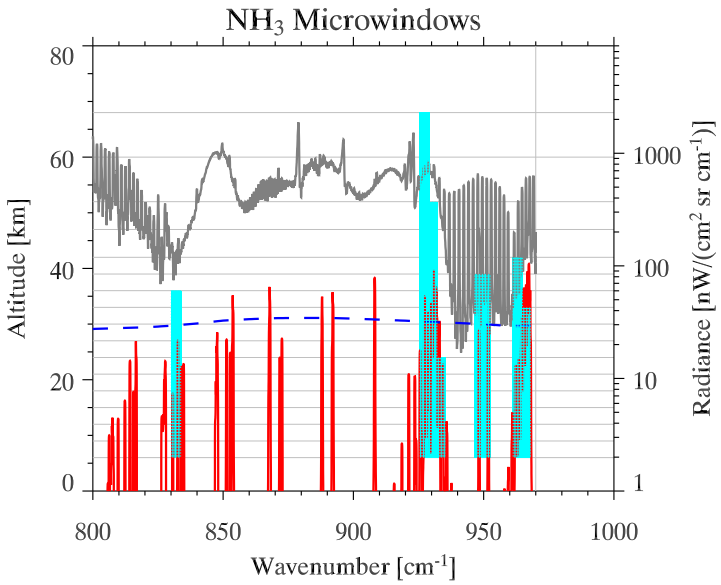

Figure 7.3: Plot indicating the position and altitude range (blue blocks) of the selected microwindows, overplotted with the total radiance (grey) within the significant spectral region for a 12 km tangent height. The lowermost lines (red) show the radiance contribution from NH_3 to this total radiance. The MIPAS nominal measurement altitudes are shown as pale horizontal lines and the NESR by the dashed blue line.

Table 7.1: The eight best ammonia microwindows.

Microwindow	Band	Spectral Range (cm^{-1})	Altitude Range (km)
NH3_0101	A	964.6500 – 967.6500	6 – 33
NH3_0102	A	928.8250 – 931.8250	6 – 52
NH3_0103	A	949.3500 – 952.1750	6 – 39
NH3_0104	A	961.6250 – 964.6250	6 – 42
NH3_0105	A	947.6000 – 949.1500	6 – 39
NH3_0106	A	926.0750 – 928.8000	6 – 68
NH3_0107	A	830.4250 – 833.4250	6 – 36
NH3_0108	A	931.8500 – 934.8500	6 – 24

7.2 Feasibility

The assessment of feasibility for retrieving ammonia followed the same procedure as the previous species. Using the initial climatological profile shown in grey in Figure

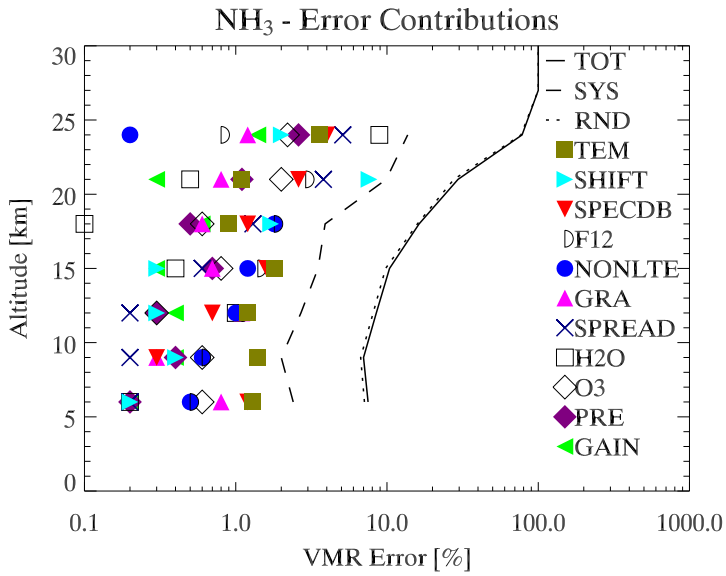

Figure 7.4: Assignment of various error sources to the final error budget as calculated during microwindow selection. The total error is shown (solid line) together with the random error component (dotted line) based on the instrument NESR. The total of the systematic error contributions is also shown (dashed line). The full list of possible error terms was given in Chapter 2. The a priori uncertainty was assumed to be 100%.

7.2 a series of microwindows were selected. Due to signal-to-noise considerations they all were in the 'A' band and their positions are shown in Figure 7.3 and in Table 7.1. The error analysis, Figure 7.4, indicates that ammonia should be relatively easy to retrieve. Given that its climatological abundance has a high uncertainty we should be able to massively improve on our knowledge of its global distribution. Blind test results, where profiles were retrieved from simulated data also indicated that MIPAS measurements of ammonia would greatly increase our knowlegde of its abundance.

7.3 Initial Retrievals

Despite this positive feasibility assessment, the retrieval gave poor results from MIPAS data.

A major problem in limb profile retrievals is contamination of the lower views with cloud. When a set of ammonia retrievals was performed over an entire orbit, it became obvious where marginal cloud was located because poor retrieval convergence was observed. There was a strong correlation between these measurements and enhanced continuum extinction values assigned to the spectra by the retrieval. The more cloudy measurements were already identified and removed by the nominal cloud flagging approach using the ratio threshold of 1.8. However, even when choosing a threshold of 4.0 (which leaves less than 10% of the profiles available for retrieval) there remained poor retrieval performance. This was characterised by high retrieved random error, randomly oscillatory profiles and poorly defined averaging kernels with areas significantly below one.

An over-estimate in the upper troposphere of the climatological abundance used to initalise the retrieval was a possible cause. This would be the case if the true ammonia VMR was falling away faster with altitude than had been anticipated. The climatological fields had used a constant tropospheric value based on boundary layer values extended up to the tropopause.

7.3.1 New A Priori

A new a priori was created that had lower values in the troposphere. A differing structure was also added, consisting of a steep falloff throughout the troposphere. This is shown in Figure 7.2. This new profile was derived by iteratively changing the a priori ($\mathbf{x}_b$) applied to a set of retrievals from real data until the difference between the a priori and measured profiles was minimised.

The lower a priori does not significantly affect the validity of the selected microwindows, but the reduced radiance associated with a lower VMR significantly impacts the random error and available information.

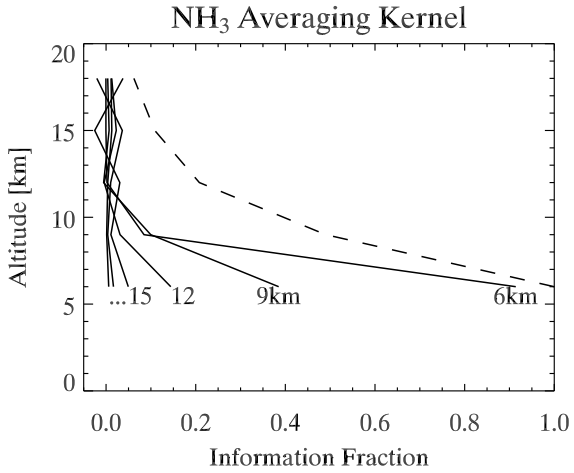

Figure 7.5: Averaging kernels from a successful retrieval. The solid lines show the contribution a measurement at one altitude has made to the retrieved values at all levels. The dotted line indicates the sum of these contributions for each level and gives an indication of the total contribution from all measurements to the final retrieved value.

Repeating the retrieval, with the improved a priori, showed limited improvement. The retrieval diagnostics highlighted that little information was gained. There were only 1-2 degrees of freedom per profile. This indicates that the useful retrieval of individual, independent profiles of ammonia are not feasible as the uncertainty on the measurement is of similar magnitude to the uncertainty in the climatology.

The averaging kernels for representative retrieval based on the new a priori is shown in Figure 7.5 and it demonstrates that only the 6 and 9 km levels show significant contributions to the retrieved values. Above 12 km there is almost no sensitivity to the atmospheric state, indicating that values above this altitude are based on the a priori constraints on the retrieval. Due to the steep VMR falloff, the variability in observed altitude (satellite pointing) becomes significant if taking the mean of a set of measurements. As a result of this a pressure level of 450 mb was chosen and information from the 6 and 9 km retrieval levels was used to calculate a VMR associated with this pressure level. This procedure also reduced the influence of pointing instability, but introduces an interpolation uncertainty.

The results were more stable than before and similar to the shape of the new a priori (as would be expected for a retrieval where the information content is still low). The exhibited a weak latitudinal structure, with higher values in profiles associated with the Northern Hemisphere. This is directly in line with surface emission distributions (Bouwman et al., 1997).

7.4 Kalman Filter

As for SO_2, previously, various approaches were attempted to improve the signal-to-noise ratio. In this instance, making use of a Kalman filter, discussed in Section 2. In this approach, the final state (VMR profile, covariance etc.) of the first successful retrieval is used as the a priori of the subsequent retrieval. The resulting state from this second retrieval is used as the a priori for the next. This approach assumes that the variation between scans around an orbit is small. Unlike the method for SO_2, the covariance of the current state is 'relaxed' by a small amount between profiles, so as not to over-constrain the subsequent retrieval. As we expect a hemispheric gradient, a value that corresponds to an along-track length of 20,000 km was chosen as the relaxation factor, so measurements of one pole are (approximately) uncorrelated with those of the other pole. The amount of information in a given spectrum is unchanged, but each retrieval step adds a bit more information about the current region whilst discarding older information that was associated with a geographically distant region. The results are discussed in the next section.

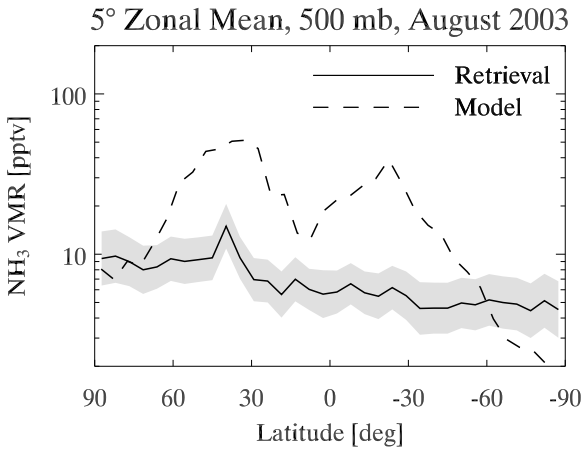

Figure 7.6: Comparison of latitudinal structure of the model and retrieval for August 2003. Shading indicates the RMS of the random error, pale shading shows the 3-σ region.

7.5 Validation

The most useful form of validation was a model comparison. The model itself is a global chemical model (HadAM3-STOCHEM), driven by historic advection data. The ammonia values originate from a selection of surface point measurements used as constant source terms to initialise the model, from the 'EDGAR' database. Further details are available in, for example, Stevenson et al. (2003) where the model set-up etc. are described. The model contains 10 psuedo-pressure levels that reach from the surface up to the tropopause. The model resulted in 120 monthly mean global data fields, driven by 1990s dynamics. For validation purposes, a decadal mean was taken for each month to try to capture monthly and seasonal variations in the ammonia field in the troposphere.

The comparison of these ammonia retrievals for August 2003 with a decadal mean model average for the month of August is shown in Figure 7.6. The model appears to have a greater dynamic range — it contains values that are up to an order of magnitude higher than the retrieval. Although the Kalman approach will have a significant

smoothing effect, the overall mean values should end up similar. The zonal mean of the model shows extratropical peaks in both hemispheres that are not observed in the retrieval. It is thought that this indicates a low retrieval sensitivity. In-situ measurements at altitude are really required, as it is also possible that the model is incorrect.

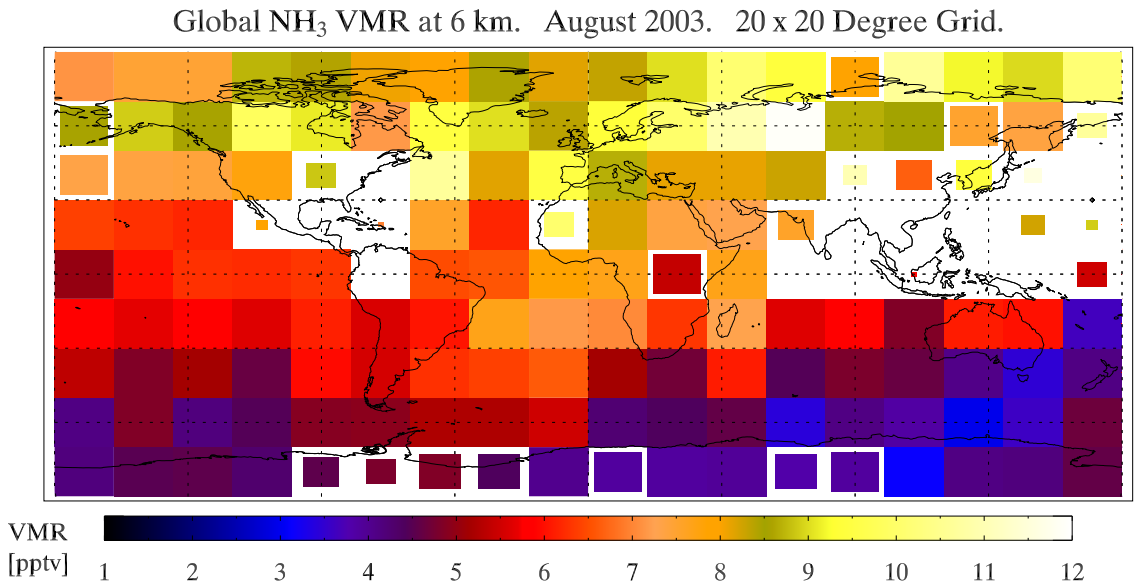

Figure 7.7: Global distribution of upper tropospheric ammonia in the gas phase. The shade of each rectangle represents the mean VMR of ammonia in ppmv. Over 15,000 retrieved values were interpolated onto a 450 mb surface (approximately 6 km altitude). These were then binned to a 20° by 20° grid covering the globe. For each bin large statistical outliers, if present, were removed. The number of measurements and the standard deviation per grid box were used to assign a 'confidence' value to each location, represented by the size of the box, rangeing from 100% confidence (full box) to no confidence (no box / blank space). Interesting features include the large region of lower confidence over Indochina, low measurement counts around the whole equator and the marked hemispheric difference in VMR with the Northern Hemisphere 5-10 times greater.

7.5.1 Global Distribution

The pressure-interpolated VMR values for ammonia for the month of orbits were binned to a 20° by 20° grid. For each gridbox, large statistical outliers were flagged

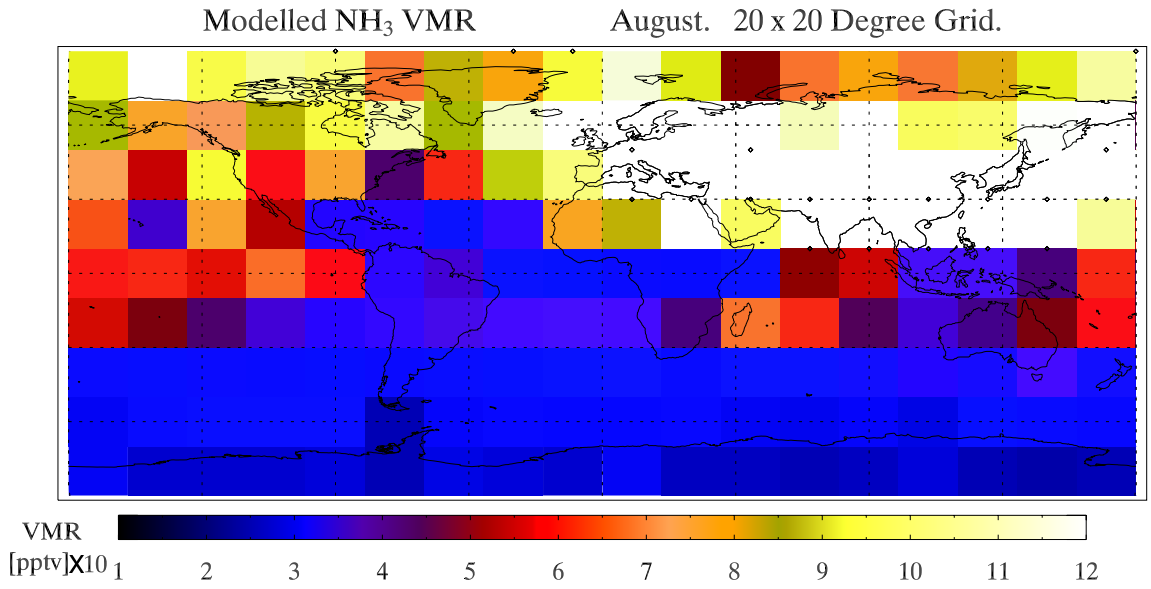

Figure 7.8: A decadal mean of the distribution of upper tropospheric ammonia in the gas phase for the month of August, as represented by a model. The resolution has been downsampled from 72×36 gridboxes and the colour scale restricted in order to match the measurements in Figure 7.7. The shade of each rectangle represents the mean VMR of ammonia in ppmv. The model works in zeta height ordinates but the level shown corresponds to approximately 450 mb.

and removed. These data were used to assign the colour and size to each of the boxes shown in Figure 7.7, which summarises these global results.

The comparison of the ammonia field for August 2003 with a decadal mean of the average output from the model for the month of August, shown in Figure 7.8, highlights several interesting features. Both show an enhancement over Indochina, with the model recording values up to 120 pptv, over the retrieval peak of 17 pptv in this region. Highs towards the North Pole, initially thought spurious are also visible in the model field. The model appears to have a greater dynamic range — it contains values that are both lower than the retrieved minimum and higher than the retrieved maximum . However, the observed order of magnitude discrepancy is within the limits of the large uncertainties in the surface source fluxes used to drive the model when combined with the chemical and dynamical modelling uncertainties used to calculate the associated value at 450 mb.

7.6 Conclusions

We have tried to give an impression of both the significance and difficulty of ammonia retrievals, along with a demostration of the current progress that has been made. It is hoped that the global ammonia distribution will aid the understanding of aerosol formation and the interaction of ammonia in sulphur and nitrogen cycles. Unfortunately, the current MIPAS ammonia data is currently too uncertain to be of any practical use.

Chapter 8

Age of Air

MIPAS results are applied to the calculation of a quantity known as ‘age of air’. Determining the age of a parcel of air is invaluable for validating model dynamics and hence the model predictions. SF_6 has a very long stratospheric lifetime coupled with a steady increase in emission and this makes it an ideal tracer for calculating the time since a volume of air was in the troposphere – its ‘age’.

8.1 Introduction

The transport of climatically important trace species plays a significant role in their global distribution. Often, regions of production (sources) are well separated from areas of destruction (sinks). A complex interaction between chemistry and transport results, that must be accurately captured by models if they are to have useful predictive value

The concept of ‘age of air’ was first applied in the stratosphere by Kida (1983), based on observations of the properties of the results of a general circulation model (GCM).

When considering atmospheric dynamics, it is useful to have species that act as tracers. These are generally unreactive on the timescale of the process under study and tend to be highly correlated with each other due to mixing (dynamics) that is much more rapid than their chemistry (kinetics). As a consequence, each infinitesimal parcel of air maintains the same concentration of inert tracer that it acquired at source. However, only the average properties of many of these infinitesimal elements may be measured and this is known as the 'mean age' (a quantity often called Γ, outlined below). Due to the presence of mixing, the pathways that have been followed by a measured set of such elements give rise to a distribution in experienced transit times. This distribution is known as an 'age spectrum' which gives us information on the mixing of air parcels with different photochemical histories. An example is shown in Figure 8.1. The mean age can be calculated from measurements of a conserved tracer, provided the variation in its emission varies linearly over the time frame of the age spectrum. So, if the rate of emission of an ideal inert tracer, such as SF_6, increases steadily with time, the observed concentration of the species at a point can be directly related to the average time since the elements of the parcel were at the same location as the source.

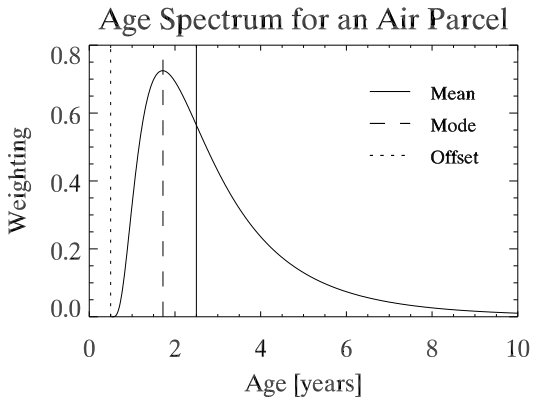

Figure 8.1: The age spectrum of a sampled air parcel, G, and its major features such as offset, mode and mean, contains information on the photochemical history of the irreducible elements within.

There are features of the stratospheric circulation that make the mean age a very useful quantity. On a timescale of months, stratospheric circulation can be described by a zonal mean ('zonally averaged circulation'). Tropospheric air, with its load of trace gases, enters the stratosphere through the tropical tropopause and rises slowly though the tropical stratosphere, spreading towards the poles. Descent occurs at mid to high latitudes, most strongly at the winter pole. This is known as the Brewer-Dobson circulation and occurs over a period of several years (Andrews et al., 1987). Below the tropical tropopause there is additional direct exchange with lower stratospheric air at mid latitudes (Holton et al., 1995), sometimes known as the 'leaky pipe' model. At mid latitudes in the stratosphere there is also efficient isentropic mixing caused by the breaking of planetary scale Rossby waves. These processes are summarised in Figure 8.2. This slow meridional circulation coupled with the wave-induced mixing determines the large-scale time averaged distribution of atmospheric tracers (Waugh and Hall, 2002).

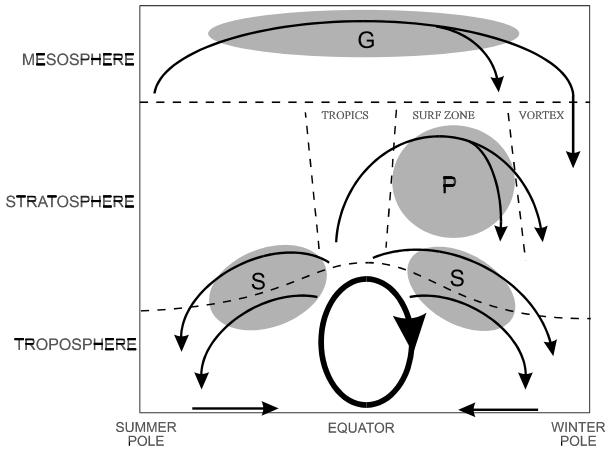

Figure 8.2: A summary of major atmospheric circulation processes, from Plumb (2002). It is a schematic of the residual mean meridional circulation in the atmosphere where heavy ellipse denotes the thermally-driven Hadley circulation of the troposphere. The shaded regions denote 'S'ynoptic and 'P'lanetary-scale waves and 'G'ravity waves, respectively that drive branches of middle atmosphere circulation.

Tracer observations have the potential to constrain the rates of these dynamical processes, and in so doing, validate the dynamical behaviour of modern GCMs. Direct comparisons with measured age profiles have highlighted serious problems in some models (Schoeberl et al., 2003) with symptoms including underestimation of mean age and excessive damping of wave propagation. Indeed, there is interest from the modelling community for zonal age fields (Chipperfield, 2005).

The source of most stratospheric species is the troposphere, which is thoroughly mixed by turbulence, convection and other processes. As a result, the distribution of the long lived tracers show much less variation in the free troposphere, and tend to be mostly independent of source location. The restricted entry into the stratosphere through the tropics also means that one may consider the source term and location for whole stratosphere as being a narrow tropical band. As a result, the tropical tropopause is often used as a reference for calculating the stratospheric lag time, which is often used interchangeably with age.

Non-linearities in the rate of emission directly map into errors in the calculated age and, as discussed in Chapter 5, there is evidence to suggest the near-linear increase in SF_6 emissions over the last 30 years is decreasing (Geller et al., 1997). In fact, the error may be up to half a year for the oldest stratospheric ages as argued by Volk et al. (1997).

Inertness of a tracer is important because loss mechanisms will be interpreted as a false ageing of the parcel. For example, the mesospheric loss term of SF_6 gives rise to an error in Γ within the strong mesospheric descent over the Southern winter pole. Comparisons of some single profile measurements of both CO_2 and SF_6 have been performed by Strunk et al. (2000) and, although generally in good agreement, the results show a 2 year discrepancy between inferred ages of the same parcel of air. They attribute this to transport of SF_6-depleted mesospheric air. A similar effect is

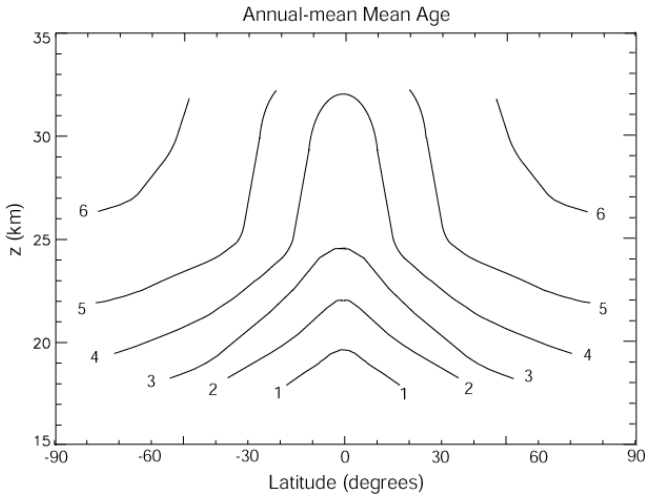

Figure 8.3: Symmetric zonal mean age from collated literature sources, from Waugh and Hall (2002). The symmetry arises due to the major lack of southern hemispheric measurements. There is also a shortage of measurements in the tropics. The ages are based on literature vertical profile observations with aircraft data from the mid 1990s giving extra coverage.

observed by Andrews et al. (2001) using a larger dataset. Reddmann et al. (2001) discusses large uncertainties in the mesospheric loss rate that make quantification of the sink term difficult. Measurements within the vortex reported by Harnisch et al. (1996) indicate an age of 5.5–7.5 years at 17–21 km and 8–10 years at 30 km from SF_6.

Figure 8.3 shows a zonal annual mean age, highlighting ages of around 1 year in the equatorial UTLS, rising to 4 years by 30 km and over 6 years in the mid stratosphere at the poles. Waugh and Hall (2002) highlight the severe shortage of Southern hemispheric measurements of age-compatible species, providing an ideal application for MIPAS measurements. In addition, there is thought to be larger seasonal variability in age at high latitudes.

8.2 Assigning Age to VMR

The lifetime is a major factor in determining the atmospheric loading of a species. The stratospheric lifetime, for example, is simply defined as

$$\tau_{\text{strat}} = \frac{\text{atmospheric load}}{\text{stratospheric sink}} \tag{8.1}$$

Lifetimes can be estimated from global emission inventories and observations of current concentrations and trends.

A measured volume of air is associated with a spectrum of ages (transit times from entry into the stratosphere) attached to its infinitesimal elements. Hall and Plumb (1994) associated this age spectrum with a Green's function of the continuity equation for a conserved tracer. This may be written as

$$\chi(\mathbf{x}, t) = \int_0^\infty \chi_0(t - t')G(\mathbf{x}, t')dt \tag{8.2}$$

where $\chi(\mathbf{x}, t)$ is the mixing ratio at time t and geolocation $\mathbf{x}$ and $G(\mathbf{x}, t')$ is the age spectrum. The mixing ratio at the point of entry into the stratosphere is given by $\chi_0(t)$. The age spectrum, already shown in Figure 8.1, is not directly observable but its mean, Γ, can be measured.

$$\Gamma(\mathbf{x}) = \int_0^\infty t'G(\mathbf{x}, t')dt' \tag{8.3}$$

This is identified with the lag time between the tropospheric and stratospheric VMRs for a linearly growing conserved tracer species (Hall and Plumb, 1994; Volk et al., 1997). Chapter 5 discussed the properties of SF_6 that make it an almost perfect chronological tracer – its well known emission time-series, nearly linear growth rate, long lifetime and stratospheric inertness. For such a perfect tracer, the mean age corre-

sponds to the lag time as given by Hall and Plumb (1994)

$$\chi(\mathbf{x}, t) = \chi_0(t - \Gamma(\mathbf{x})) \tag{8.4}$$

More complex relationships have also been determined, taking into account hemispheric differences as well as the effect of tracer transience and non-linearity in the tropospheric tracer time series. For SF_6, these effects are generally small.

In an interesting application of tracers, Volk et al. (1997) go on to show that knowledge of a tracer gradient at the mid latitude tropopause as a function of mean age, allows the direct calculation of the net global tracer flux through the troposphere. In addition, an approximate shape of the age spectrum may be estimated by using the finite lifetimes of a set of trace gases to probe G. This relies on accurate knowledge of the lifetimes.

8.2.1 Calculating Age from SF_6 VMR

Using a variety of data between 1987 and 1996, Geller et al. (1997) determine a simple quadratic relationship between time and SF_6 VMR, Equation 8.6. Quadratic fits to hemispheric time series were also published and the authors join others, such as Maiss et al. (1996), in estimating the hemispheric exchange time and other dynamical parameters from these results.

$$\chi_0(t) = a + b(t - t_0) - c(t - t_0)^2 \tag{8.5}$$

$$\overline{[\mathrm{SF}_6]}(t) = 3.4361 + 0.2376(t - 1996) + 0.0049(t - 1996)^2 \tag{8.6}$$

Indeed, as discussed in Chapter 5 there have been a selection of trend estimates over the past 20 years, often given in terms of a percentage per annum increase in-

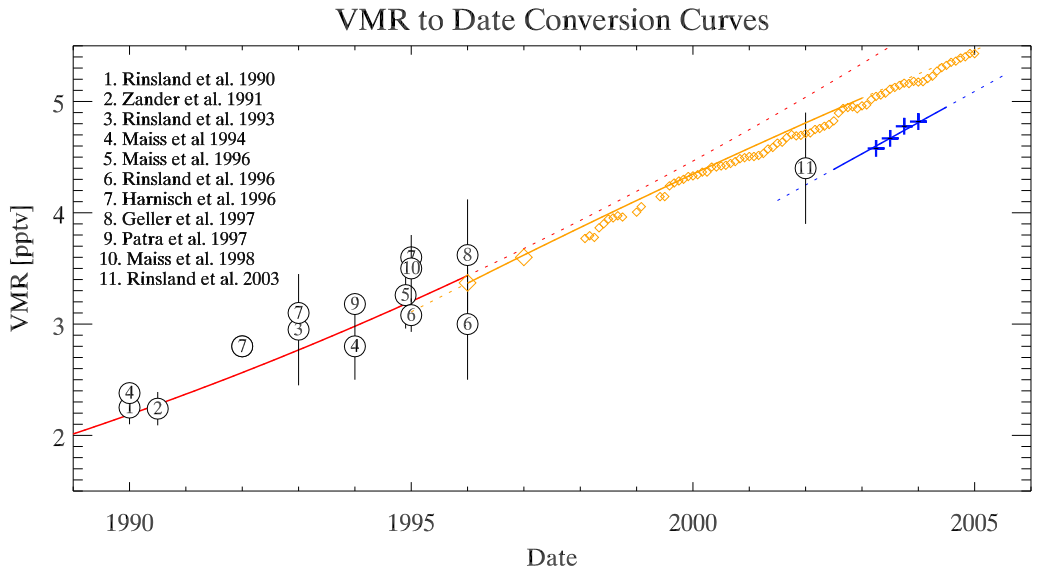

Figure 8.4: Curves relating the SF_6 VMR to age of air. They are the quadratic Equation 8.6 in red, the CMDL surface flask measurements in [orange] and the results of this work in [blue]. In addition, a series of point measurements are shown, with the associated reference shown on the figure.

stead of a fitted quadratic. One such example is the 7% increase observed by Rinsland et al. (2003). Other authors have also investigated the relation between the VMR of SF_6 and the age of the observed air parcel. For example, Waugh and Hall (2002) and Harnisch et al. (1996) determine similar, constant, year-on-year rates of increase during the mid 1990s between 0.2 and 0.3 pptv yr^{-1}. A long term, highly accurate and consistent set of surface flask measurements from eight global sites gives a mean 0.24 pptv yr^{-1} (around 5%) per year SF_6 increase from 1996 to the end of 2003 along with the highest literature value of 5.0 pptv for the end of the year for the Northern hemisphere (Mondeel et al., 2003; Butler et al., 2005). This dataset, from the National Oceanic and Atmospheric Administration (NOAA) Climate Monitoring and Diagnostics Laboratory (CMDL), does point to a slight reduction in the growth of the rate of emission. This value had previously been observed to be constant (or even increasing)

from the late 1970s to the 1990s, although with significantly greater uncertainty on the measurements. For now, the effect of this non-linearity is discounted, but it has the potential to influence calculated ages. This greater uncertainty on older measurements is potentially a major source of error for age determination as although the historic trend is not useful for determining current trend it is the only way to assign age to a measured VMR below current values. Fortunately, the maximum ages are of the order 7–10 years, and in future only the more accurate recent measurements will be of significance to age calculation.

The age calibration curves determined from the quadratic in Equation 8.6, the 7% value quoted by Rinsland et al. (2003), the CMDL flask measurements and the 2002–2003 trend calculated from MIPAS observations in Chapter 5 are all shown in Figure 8.4. In addition there are a variety of point measurements of SF_6 VMR from the literature, concentrated in the mid 1990s, for comparison with the extrapolated trend lines.

8.3 Results

Figure 8.5 shows the application of a composite of the Geller and CMDL curves to the latitudinal profiles from Figure 5.13. Each stratospheric region of these profiles can be assigned an age since it was last at the tropical tropopause by reference to its VMR. As the flask sample trend and the MIPAS results are similar, differing only by absolute VMR, a constant offset of 18 months was applied, corresponding to the VMR difference of 0.45 pptv for equivalent dates. This was done because the flask data smoothly transitions to the trend quadratic that is itself composed mainly of in-situ measurements. An allowance of 6 months to mix well from the surface sources where the flask measurements take place to the tropical tropopause and entry into the

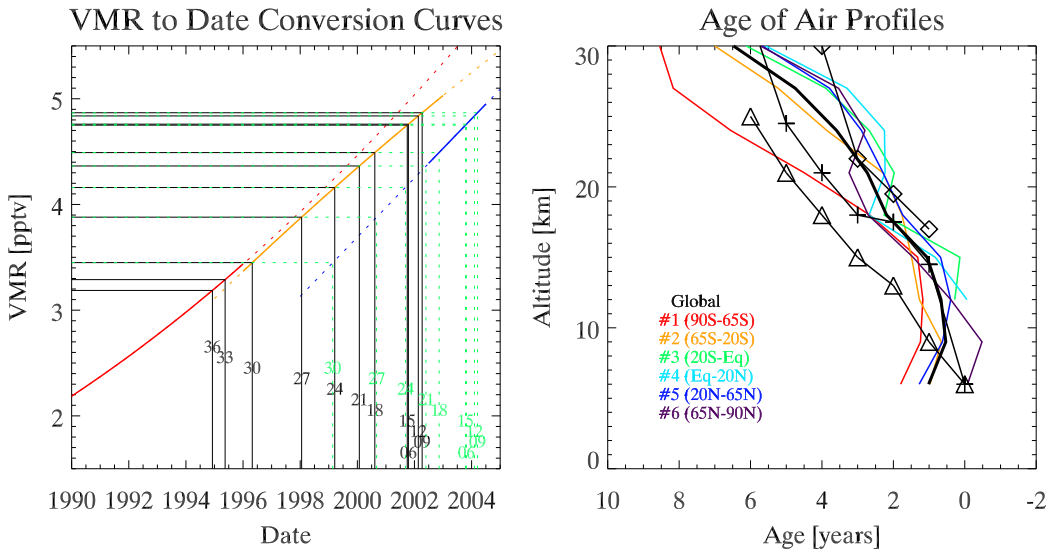

Figure 8.5: [Left] Application of the simple VMR to age conversion. The two curves used join smoothly around 1997–8, although almost all the measured VMRs lie to the right of this date, so a smooth transition is not a necessity. [Right] The effect of applying the almost linear quadratic age conversion curve composite by Geller et al. (1997) and the CMDL to the mean mid latitude SF_6 VMR profiles shown in Figure 5.13. A constant age offset has been applied to compensate for the systematic difference between the remotely sensed mid tropospheric MIPAS results and the surface flask measurements. The ages are approximately comparable with the simple symmetric age distribution in Figure 8.3. The solid symbols show the modelled age distribution from Figure 8.3, corresponding to equatorial (diamonds), polar (triangles) and mid latitudes (crosses).

stratosphere was also applied to the overall age calculation.

The simple age calibration curve can similarly be used to convert the zonal mean maps of SF_6, presented previously, into zonal age distributions. Figure 8.6 shows the zonal mean ages estimated for August 2003. For the Southern polar winter case, the large amount of descent of chemically depleted mesospheric air into the top of the polar vortex gives anomalously old age values. The values at the tropopause are around zero years, and there is the basic dynamical structure of the atmosphere visible in the zonal mean.

Some model results are available for the variation in zonal mean age with the seasons, Reddmann et al. (2001). In effect this also acts as a validation of the SF_6 zonal

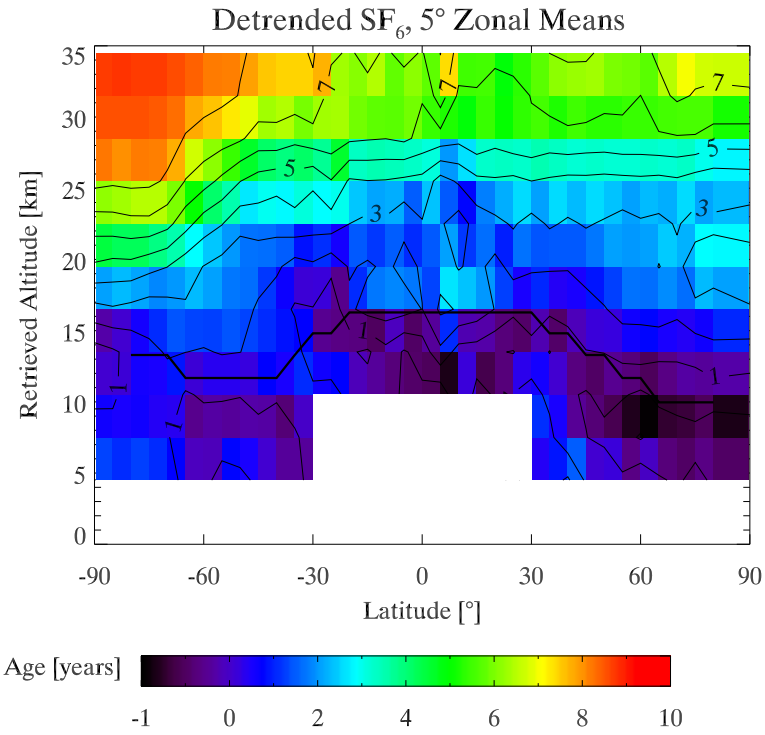

Figure 8.6: August 2003 zonal mean age from SF_6 data, originating from the VMR data shown in Figure 5.14. The conversion was performed using the same almost linear relation as was applied to the latitude bands, in Figure 8.5. Overall the ages are in agreement with previous observations and the general understanding of atmospheric circulation. It shows a young troposphere, with a hemispheric exchange time of about less than 1 year (i.e. difference in age). The oldest air is over the poles at higher altitudes, with this month showing the effect of depletion over the southern winter pole.

means if a purely linear age calibration curve was used (which is a reasonable approximation). Figure 8.7 shows zonal mean age plots for the solstice and equinox months from model data. The corresponding MIPAS results are shown in Figure 8.8, with colour to make the distribution clearer. The MIPAS contours are noisy and only extend to 30 km. However, the gross features and basic age structure are similar. Qualitative comparison is precluded by the lack of machine-readable data.

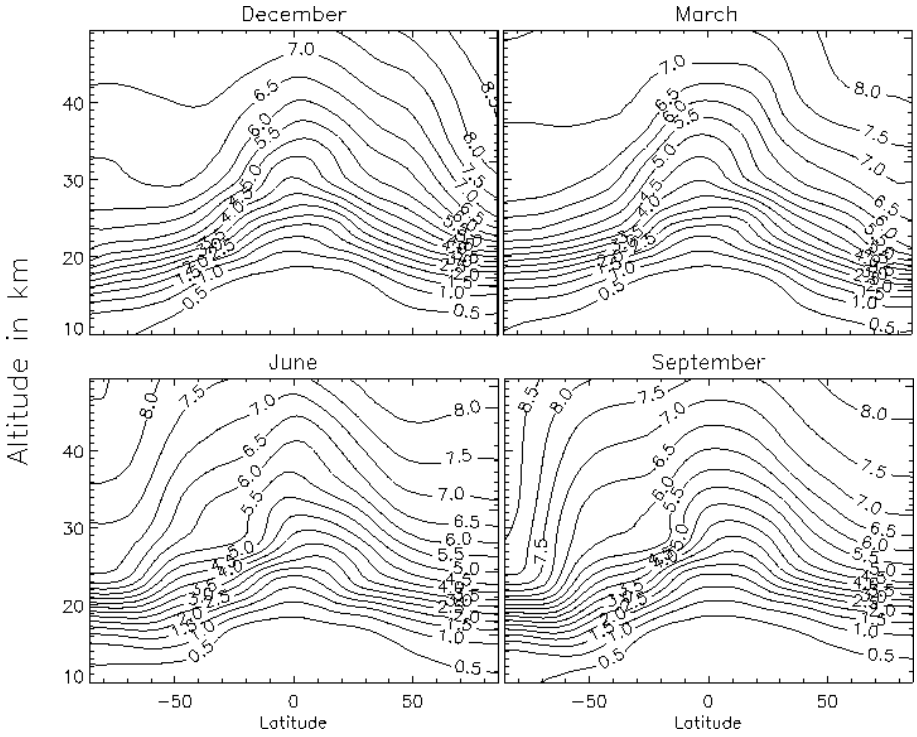

Figure 8.7: Zonal mean age of air fields for the solstice and equinox months.

8.4 Conclusions

This chapter has shown that it is possible to use MIPAS results to determine the seasonal changes in the age of stratospheric air from the inert tracer, SF_6. Potentially, with the wide variety of species that MIPAS can observe, it should be possible to use the distribution of multiple gases to infer the age spectrum of any point observed.

The SF_6 VMR to age conversion is sensitive to calibration curve used. Fortunately the historic trend is highly linear, but even small non-linearities can influence the calculated age. In a related fashion, there is a degree of sensitivity to biases in the MIPAS retrievals, especially at high altitude where the a priori contribution is greater. The prior information will show up as unreasonable age values, whereas no such simple check exists when examining the results as VMRs.

Comparisons with model results showed the same gross structure. However, there

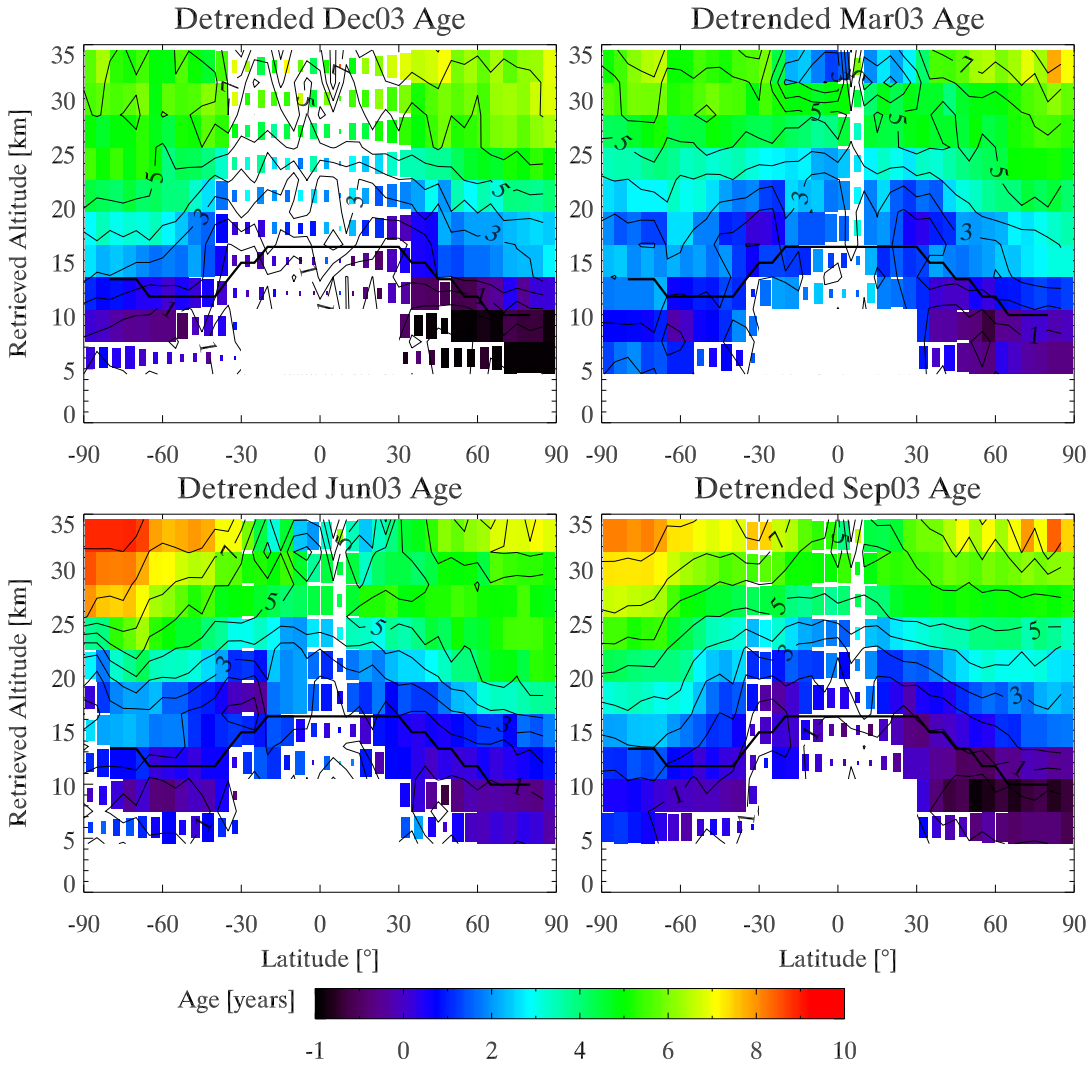

Figure 8.8: Seasonal MIPAS derived age measurements, derived from the SF_6 zonal means shown in Chapter 5.

is known to be a wide variation in the age behaviour of the many models in use world-wide, so the lack of fine agreement — whilst disappointing — is still helpful validation.

There has been interest in SF_6 derived age fields in the modelling community. Indeed, it has been noted that the age is by far preferable to the 'raw' VMR values.

In summary, the calculation of age of air from MIPAS SF_6 data is a useful resource, but requires more quantitative validation before it will be directly usable by members of the modelling community without remote sensing experience.

Chapter 9

Conclusions

The aim of this thesis was to investigate the global distribution of a selection of trace gases. These gases were selected by considering a combination of scientific need and a previous shortage of measurements. In other words, where could the greatest improvement in our knowledge of the atmosphere be made?

Carbonyl sulphide has been shown to have a tropospheric VMR of approximately 500 pptv, in line with climatological expectations. There is no evidence for an interannual trend, although the short length of the time series makes a firm conclusion difficult. There is a small N-S interhemispheric difference of 0-30 pptv, attributed to differences in the geolocations of the dominant source and sink terms. This shows some seasonal dependance. The stratospheric results have shown the lifetime of OCS to be slightly longer than previous literature estimates, at 10 years. This has an effect on various terms of interest to calculating global sulphur budgets and fluxes which influence SSAs and hence the radiative balance of the Earth. The mass of sulphur attributable to OCS in the stratosphere is approximately 0.52 Tg with the bulk of the mass in the troposphere (4.94 Tg). The work on retrieving OCS is very much 'complete' and could potentially become an operational species.

Sulphur hexafluoride has also been a successful target species. A clear year-on-year increase has been demonstrated, from 4.6 pptv in December 2002 to 4.9 pptv in March 2005. There is also a well defined interhemispheric variability of 0.1-0.2 pptv that is directly attributed to the interaction of dynamics with an almost exclusively Northern hemispheric source terms. The inertness of SF_6 and its interannual trend coupled with vertical transport into the stratosphere in the tropics produces an almost ideal tracer. By looking at historic trends and the current VMR of regions of the stratosphere, it is possible to calculate the amount of time that has passed since that parcel was at the tropical tropopause. The resulting age distributions are useful in validating model dynamics.

Sulphur dioxide was used to explore the more complex methods of coaddition as there was insufficient signal-to-noise for the nominal retrieval scheme. Using the same a priori substitution approach as for SF_6 gave rise to a smooth SO_2 field showing reasonable zonal structure. However, the northern mid latitudes showed no anthropogenic enhancement and there was an anomalous enhancement at the southern winter pole that could not be assigned to an interfering species. Unfortunately, the mean radiance approach exhibited very noisy retrievals as there was much less prior information constraining them. The mean residual approach showed some potential, with well formed diagnostics and generally smooth profiles. However, the upper stratospheric values seemed anomalously high and the lower stratospheric minimum on SO_2 was not well resolved. Fourthly, the Kalman filter approach was tried, with some promising results. It showed strong zonal structure, anthropogenic enhancement and the SO_2 minimum. However, it too showed enhanced southern winter pole values. Many of the zonal structures observed are not unreasonable, but they they are not reproduced by models and height resolved measurements to high altitude in the southern hemisphere are lacking.

Finally, the retrieval of ammonia was attempted. Although there is some evidence for zonal sensitivity in the retrieval, the results have been very difficult to validate. However, a new mean tropospheric profile which exhibits a steep vertical concentration gradient has been suggested, and this improves the retrieval diagnostics.

9.1 Future Work

Regarding the four species discussed, the main future work associated with OCS and SF_6 would be the calculation of all months for which the nominal full resolution data exists (September 2002 to March 2004). This would form a useful dataset of previously rare gases. For SF_6, there are more detailed analyses that can be performed with respect to the age of air calculations, although there are unlikely to be any major changes below 20-25 km. For SO_2, there seems to be potential in the Kalman type approach and this is a strong candidate for further investigation. It may also be interesting to try this method on SF_6, to avoid the need for substituting the prior information at the topmost altitudes.

9.2 Summary

This thesis has demonstrated that the measurement of OCS, SF_6, SO_2 and NH_3 by satellite, with its global coverage, has greatly improved our knowledge of the distribution and variation in their abundances. The prior lack of measurements was a direct consequence of the difficulty with which the spectral information on these species may be extracted from the remote measurements. As a result, this thesis has investigated a selection of methods for combining multiple measurements prior, during and post retrieval. It has also considered the implications of using prior information and

the optimal estimation technique to constrain the fitting of the trace gas profiles to the measured spectral data. This work has also attempted to show some of the applications of well characterised 3D global measurements at high resolution, by investigating the stratospheric sulphur budget contribution from OCS as well as inferring the age of regions of stratospheric air by using SF_6 VMRs as an age proxy. Both SO_2 and NH_3 were less successful — defeated by signal-to-noise and, to some extent, atmospheric variability. However, there has been some progress in the limb resolution of SO_2, both in volcanic plumes and zonally. New constraints on the mean tropospheric distribution of ammonia have also been estimated. Indeed, both these species have required more complex techniques that are likely to be of use in other problems.

Bibliography

ABB BOMEM (2002). MIPAS comissioning review and line of sight accuracy. Technical report, European Space Agency. ESA/PO-RP-BOM-GS-1096.

Adams, P., Seinfeld, J., and Koch, D. (1999). Global concentration of tropospheric sulphate, nitrate and ammonium aerosol simulated in a GCM. *J. Geophys. Res.*, 104:13791–13823.

Alpaslan, D. (2004). *Remote Sensing of the Stratosphere*. PhD thesis, ISAC - CNR.

AMIL2DA (2003). AMIL2DA. Technical report, IMK. co–ordinated by T. von Clarmann.

Andrews, A., Boering, K., Daube, B., Wofsy, S., Loewenstein, M., Jost, H., Podolske, J., Webster, C., Herman, R., Scott, D., Flesch, G., Moyer, E., Elkins, J., Dutton, G., Hurst, D., Moore, F., Ray, E., Romashkin, P., and Strahan, S. (2001). Mean ages of stratospheric air derived from in situ observations of CO_2, CH_4 and N_2O. *J. Geophys. Res.-Atmos.*, 106(D23):32295–32314. doi:10.1029/2001JD000465.

Andrews, D., Holton, J., and Levoy, C. (1987). *Middle Atmosphere Dynamics*. Academic Press, San Diego, California.

Asman, W., Sutton, M., and Schjorring, J. (1998). Ammonia: emission atmospheric transport and deposition. *New Phytol.*, 139:27–48.

Aydin, M., Bruyn, W. D., and Saltzman, E. (2002). Preindustrial atmospheric carbonyl sulfide (OCS) from an antarctic ice core. *Geophys. Res. Lett.*, 29:1356–1359.

Barnes, I., Becker, K., and Patroescu, I. (1994). The tropospheric oxidation of dimethyl sulphide: a new source of carbonyl sulphide. *Geophys. Res. Lett.*, pages 2389–2392.

Beer, R. (1992). *Remote Sensing by Fourier Transform Spectrometry*. Wiley–Interscience.

Birk, M., Hase, F., and Wagner, G. (2002). AO 652: IRAC (in-flight radiometric accuracy assessment of MIPAS). Presentation given at Envisat CalVal Workshop, September 2002, ESTEC, ESA SP-1266.

Bluth, G. (2003). Application of TOMS data to volcanic hazard mitigation. http://www.geo.mtu.edu/ gbluth/Research/02.senh.final.html.

Bluth, G., Doiron, S., Schnetzler, C., Krueger, A., and Walter, L. (1992). Global tracking of the SO_2 clouds from the June 1991 Mount Pinatubo eruptions. *Geophys. Res. Lett.*, 19:151–154.

Bouwman, A., Lee, D., Asman, W., Dentener, F., Van Der Hoek, K., and Oliver, J. (1997). A global high-resolution emission inventory for ammonia. *Global Biogeochemical Cycles*, 11(4):561–587.

Burgess, A. and Dudhia, A. (2003). Validation of spectral calibration including the D band using OCS microwindow residuals. MIPAS Quality Working Group (QWG) meeting 2. Florence, Italy.

Burgess, A., Grainger, R., Dudhia, A., Payne, V., and Jay, V. (2004). MIPAS measurements of sulphur hexafluoride (SF_6). *Geophys. Res. Lett.*, 31:L05112. doi:10.1029/2003GL019143.

Burgess, A. B. (2003). Detection of SO_2 from MIPAS, below the tropopause. Presentation given at EGS joint assembly, April 2003, Nice.

Butler, J., Mondeel, D., Scheffer, A., Hall, B., Hurst, D., Dlugokencky, E., Elkins, J., Dutton, G., and NOAA/CMDL (2005). Surface SF_6 flask measurements. National Oceanic and Atmospheric Administration (NOAA) Climate Monitoring and Diagnostics Laboratory (CMDL) Chromatograph for Atmospheric Trace Species (CATS) experiments.

Chin, M. and Davis, D. (1993). Global sources and sinks of OCS and CS_2 and their distributions. *Global Biogeochem. Cyc.*, 2:321–337.

Chin, M. and Davis, D. (1995). A reanalysis of OCS as a source of stratospheric backround sulphate aerosol. *J. Geophys. Res.*, 100:8993–9005.

Chipperfield, M. (2005). Presentation on the exploitation of satellite date in models. SCOUT-O3/DIAC workshop, Leicester.

Connell, P. O., Heil, F., Henriot, J., Mauthe, G., Morrison, H., Niemeyer, L., Pittroff, M., Probst, R., and Taillebois, J. (2000). SF_6 in the electric industry. Paper presented at CIGRE 2000.

Crutzen (1976). The possible importance of CSO for the sulfate aerosol layer of the stratosphere. *Geophys. Res. Lett*, 3:73–76.

Dean, S., Lawrence, B., Grainger, R., and He, D. (2005). Orographic cloud in a GCM: The missing cirrus. *Climate Dynamics*, 24:771–780. doi:10.1007/s00382-005-0020-9.

Dervos, C. and Vassiliou, P. (2000). Sulfur hexafluoride (SF_6): Global environmental effects and toxic byproduct formation. *J. Air Waste Manage. Assoc.*, 50:137–141.

Dinelli, B., Magnani, L., Carlotti, M., and Ridolfi, M. (2003). Multi-target retrieval of the VMR of SF_6 from MIPAS spectra. Poster, Proceedings from ASSFTS–11, Bad-Wildbad, Germany.

Dudhia, A. (2000). Survey of existing algorithms for the selection of auxiliary data, MIPAS special modes study WP4000. Technical report, University of Oxford. ESA Contract 16700/02/I-LG.

Dudhia, A. (2002). The Reference Forward Model (RFM). Technical report, University of Oxford. ESA Contract 11886/96/NL/CN.

Dudhia, A. (2005). The MIPAS Orbital Retrieval using Sequential Estimation (MORSE). Technical report, University of Oxford.

Dudhia, A., Jay, V., and Rodgers, C. (2002a). Microwindow selection for high spectral resolution sounders. *Applied Optics*, 41:3665–3673.

Dudhia, A., Morris, P. E., and Wells, R. J. (2002b). Fast monochromatic radiative transfer calculations for limb sounding. *J. Quant. Spectrosc. Radiat. Transf.*, 74:745–746.

Echle, G., von Clarmann, T., Dudhia, A., Flaud, J.-M., Funke, B., Glatthor, N., Kerridge, B., Lopez-Puertas, M., Martin-Torres, F., and Stiller, G. (2000). Optimized spectral microwindows for MIPAS – Envisat data analysis. *Applied Optics*, 39:5531–5540.

Eisinger, M. and Burrows, J. P. (1998). Tropospheric SO_2 observed by the ERS-2 GOME instrument. *Geophys. Res. Lett.*, 25:4177–4180.

Engel, A. and Schmidt, U. (1994). Vertical profile measurements of carbonyl sulphide in the stratosphere. *Geophys. Res. Lett*, 21:2219–2222.

Envisat (2001). http://envisat.esa.int.

ESA (2000a). Envisat-1: Mission and system summary. Technical report, European Space Agency, Dornier Satellitensysteme GmbH, Matra Marconi Space, Thompson-CSF. ESA/SP-1229.

ESA (2000b). Envisat MIPAS - an instrument for atmospheric chemistry and climate research. Technical report, European Space Agency. ESA Bulletin No. 101, ISSN 0276-4265.

ESA (2004). Envisat MIPAS product handbook. Technical report, European Space Agency. Revision 1.2, September. http://envisat.esa.int/dataproducts.

Flaud, J.-M. (2002). Spectrocopic updates. Presentation and discussion from MIPAS Science Advisory Group, July 2002, ESTEC and MIPAS Special Modes Kick-off meeting, Feb 2003, Bologna.

Flaud, J.-M. (2003). Review of spectroscopic parameters (WP1300). ESA ITT AO/1-4232/02/I-LG, 33pp.

Flaud, J.-M., Piccolo, C., Carli, B., Perrin, A., Coudert, L., Teffo, J.-L., and Brown, L. (2003). Molecular line parameters for MIPAS. *J. Ocean Atm. Opt.*, 16:172–182.

Geller, L., Elkins, J., Lobert, J., Clarke, A., Hurst, D., Butler, J., and Myers, R. (1997). Tropospheric SF_6: Observed latitudinal distribution and trends, derived emissions and interhemispheric exchange time. *Geophys. Res. Lett.*, 6:675–678.

Goldman, A., Coffey, M., Stephen, T., Rinsland, C., Mankin, W., and Hannigan, J. (2000). Isotopic OCS from high-resolution balloon-borne and ground-based infrared solar absorption spectra. *J. Quant. Spectrosc. Radiat. Transf.*, 67:447–455.

Goody, R. and Yung, Y. (1989). *Atmospheric Radiation: Theoretical Basis*. Oxford University Press, 2nd edition.

Griffith, D., Jones, N., and Matthews, W. (1998). Interhemispheric ratio and annual cycle of carbonyl sulfide (OCS) total column from ground-based solar FTIR spectra. *J. Geophys. Res.-Atmos.*, 103:8447–8454.

Griffiths, P. and de Haseth, J. (1986). *Fourier Transform Infrared Spectrometry*. John Wiley and Sons.

Hall, T. and Plumb, R. (1994). Age as a diagnostic of stratospheric transport. *J. Geophys. Res.-Atmos.*, 99:2059–2070.

Harnisch, J., Borchers, R., Fabian, P., and Kourtidis, K. (1995). Aluminium production as a source of atmospheric carbonyl sulfide (COS). *Environ. Sci. Pollut. Res.*, 2:161–162.

Harnisch, J., Borchers, R., Fabian, P., and Maiss, M. (1996). Tropospheric trends for CF_4 and C_2F_6 since 1982 derived from SF_6 dated stratospheric air. *Geophysical Research Letters*, 23:1099–1102.

Harnisch, J. and Eisenhauer, A. (1998). Natural CF_4 and SF_6 on Earth. *Geophys. Res. Lett.*, 25:2401–2404.

HITRAN (2003). Special Edition *J. Quant. Spectrosc. Radiat. Transf.*, vol. 82, numbers 1-4, 2003 and http://www.hitran.com.

Hobe, M. V., Cutter, G., Kettle, A., and Andreae, M. (2002). Dark production: A significant source of oceanic COS. *J. Geophys. Res.-Oceans*, 106:31217–31226.

Holton, J., Haynes, P., McIntyre, M., Douglass, A., Rood, R., and Pfister, L. (1995). Stratosphere-troposphere exchange. *Review of Geophysics*, 33:403–409.

Jay, V. (2000). Remote sounding of the atmosphere by high resolution spectroscopy. D.Phil. University of Oxford.

Jay, V., Dudhia, A., and Rodgers, C. (2001). MIPAS error analysis using spectral signatures. Proceedings of the 10th International Workshop on Atmospheric Science from Space using Fourier Transform Spectrometry (ASSFTS10), Ventura, California.

Johnson, J. (1981). The lifetime of carbonyl sulphide in the troposphere. *Geophys. Res. Lett.*, pages 938–940.

Junge, C., Chagnon, C., and Manson, J. (1961). Stratospheric aerosols. *J. Meteorology*, pages 81–108.

Kettle, A., Kuhn, U., von Hobe, M., Kesselmeier, J., and Andreae, M. (2002a). Global budget of atmospheric carbonyl sulfide: Temporal and spatial variations of the dominant sources and sinks. *J. Geophys. Res.-Atmos.*, 107:4642–4658.

Kettle, A., Kuhn, U., von Hobe, M., Kesselmeier, J., Liss, P., and Andreae, M. (2002b). Comparing forward and inverse models to estimate the seasonal cariation of hemisphere-integrated fluxes of carbonyl sulphide. *Atmos. Chem. Phys.*, 2:343–361.

Kida, H. (1983). General circulation of air parcels and transport characteristics derived from a hemispheric GCM. part 2. very long-term motions of air parcels in the troposphere and stratosphere. *J. Meteor. Soc. Japan*, 61:510–522.

Ko, M., Sze, N. D., Wang, W.-C., Shia, G., Goldman, A., Murcary, F., Murcary, D., and Rinsland, C. (1993). Atmospheric sulfur hexafluoride: Sources, sinks and greenhouse warming. *Journal of Geophysical Research*, 98:10499–10507.

Krieg, J., Nothholt, J., Mahieu, E., Rinsland, C., and Zander, R. (2005). Sulphur hexafluoride (SF_6): comparison of FTIR-measurements at three sites and determination of its trend in the northern hemisphere. *J. Quant. Spectrosc. Radiat. Transf.*, 92 (3):383–392.

Lan, T., Nishimura, R., Tsujino, Y., Imamura, K., Warahina, M., Hoang, N., and Maeda, Y. (2004). Atmospheric concentrations of sulphur dioxide, nitrogen oxides, ammonia, hydrogen chloride, nitric acid, formic and acetic acids in the south of Vietnam measured by the passive sampling method. *Analytical Sciences*, 20:213–217.

Lelieveld, J., Roelofs, G., Feichter, J., and Rodhe, H. (1997). Terrestrial sources and distribution of atmospheric sulphur. *Philos. Trans. R. Soc. Lond. B-Biol. Sci.*, 352:149–157.

Leung, F., Colussi, A., Hoffmann, M., and Toon, G. (2002). Isotopic fractionation of carbonyl sulfide in the atmosphere: Implications for the source of background stratospheric sulfate aerosol. *Geophys. Res. Lett.*, 29:1470–1474.

Leung, F.-Y. T. (2003). *Elucidation of the Origins of Stratospheric Sulfate Aerosols by Isotopic Methods*. PhD thesis, California Institute of Technology.

Liao, H., Adams, P., Chung, S., Seinfeld, J., Mickley, L., and Jacob, D. (2003). Interactions between tropospheric chemistry and aerosols in a unified general circulation model. *J. Geophys. Res.*, 108(D1):4001. doi:10.1029/2001JD001260.

Mahieu, E., Zander, R., Delbouille, L., Demoulin, P., Roland, G., and Servais, C. (1997). Observed trends in total vertical column abundances of atmospheric gases from IR solar spectra recorded at the Jungfraujoch. *J. Atmos. Chem.*, 28:227–243.

Maiss, M. and Brenninkmeijer, C. (1998). Atmospheric SF_6: Trends, sources, and prospects. *Environ. Sci. Technol.*, 32:3077–3086.

Maiss, M. and Levin, I. (1994). Global increase of SF_6 observed in the atmosphere. *Geophys. Res. Lett.*, 21:569–572.

Maiss, M., Steele, L., Francey, R., Fraser, P., Trivett, R. L. N., and Levin, I. (1996). Sulfur hexafluoride - a powerful new atmospheric tracer. *Atmos. Environ.*, 30:1621–1629.

McEwan, M. and Phillips, L. (1975). *Chemistry of the Atmosphere*. Arnold.

Moller, D. (1995). *Sulfate aerosols and their atmospheric precursors*. Wiley.

Mondeel, D., Scheffer, A., Hall, B., Hurst, D., Butler, J., Dlugokencky, E., Elkins, J., and Dutton, G. (2003). Atmospheric sulfur hexafluoride still on the increase. Technical report, National Oceanic and Atmospheric Administration (NOAA) Climate Monitoring and Diagnostics Laboratory (CMDL). Annual Report.

Nguyen, B., Mihalopoulos, N., and Putard, J. (1994). Rice straw burning in southeast-asia as a source of CO and COS to the atmosphere. *J. Geophys. Res.-Atmos.*, 99:16435–16439.

NOAA (2000). Atmospheric ammonia: Sources and fate — a review of ongoing federal research and future needs. Technical report, NOAA Aeronomy Laboratory. Air Quality Research Subcommittee Meeting Report.

Notholt, J., Kuang, Z., Rinsland, C., Toon, G., Rex, M., Jones, N., Albrecht, T., Deckelmann, H., Krieg, J., Weinzierl, C., Bingemer, H., Weller, R., and Schrems, O. (2003). Enhanced upper tropical tropospheric COS: Impact on the stratospheric aerosol layer. *Science*, 300:307–310.

Oelhaf, H., LEupolt, A., and Fisher, H. (1982). Discrepancies between balloon-borne IR atmospheric spectra and corresponding synthetic spectra calculated line by line around 825 wavenumbers. *Applied Optics*, 22(5):647–649.

Patra, P., Lal, S., Subbaraya, B., Jackman, C. H., and Rajaratnam, P. (1997). Observed vertical profile of sulfur hexafluoride (SF_6) and its atmospheric applications. *J. Geophys. Res.-Atmos.*, 102:8855–8859.

Pitari, G., Mancini, E., Rizi, V., and Shindell, D. (2002). Impact of future climate and emission changes on stratospheric aerosols and ozone. *J. Atm. Sci.*, 59:414–417.

Plumb, R. A. (2002). Stratospheric transport. *J. Met. Soc. Japan*, 80 (4B):793–809.

Reddmann, T., Ruhnke, R., and Kouker, W. (2001). Three-dimensional model simulations of SF_6 with mesospheric chemistry. *J. Geophys. Res.-Atmos.*, 106:14525–14537.

Regalia-Jarlot, L., Hamdouni, A., Thomas, X., der Heyden, P. V., and Barbe, A. (2002). Line intensities of the bands of the $^{16}O^{12}C^{32}S$ molecule. *J. Quant. Spectrosc. Radiat. Transf.*, 74:455–470. doi:10.1016/S0022-4073(01)00267-9.

Remedios, J. J. (1999). Extreme atmospheric constituent profiles for MIPAS. *Proceedings of the European Symposium on Atmospheric Measurements from Space*, 2:779–783.

Ridolfi, M., Carli, B., and Carlotti, M. (2000). Optimized forward model and retrieval scheme for MIPAS near-real-time data processing. *Appl. Optics*, 39:1323–1340.

Rinsland, C., Boone, C., Nassar, R., Walker, K., P.Bernath, Mahieu, E., Zander, R., McConnell, J., and Chiou, L. (2005). Trends of HF, HCl, CCl_2F_2, CCl_3F, $CHClF_2$ (HCFC-22), and SF_6 in the lower stratosphere from Atmospheric Chemistry Experiment (ACE) and Atmospheric Trace Molecule Spectroscopy (ATMOS) measurements near 30 degrees N latitude. *Geophys. Res. Lett.*, 32 (16):L16S03. doi:10.1029/2005GL022415.

Rinsland, C., Goldman, A., and Flaud, J.-M. (1992a). Infrared spectroscopic parameters of COF_2, SF_6, ClO, N_2, and O_2. *J. Quant. Spectrosc. Radiat. Transf.*, 48:693–699.

Rinsland, C., Goldman, A., Mahieu, E., Zander, R., Notholt, J., Jones, N., Griffith, D., Stephen, T., and Chiou, L. (2002). Ground-based infrared spectroscopic measurements of carbonyl sulfide: Free tropospheric trends from a 24-year time series of solar absorption measurements. *J. Geophys. Res.-Atmos.*, 107:4648–4657.

Rinsland, C., Goldman, A., Stephen, T., Chiou, L., Mahieu, E., and Zander, R. (2003). SF_6 ground-based infrared solar absorption measurements: long-term trend, pollution events, and a search for SF_5CF_3 absorption. *J. Quant. Spectrosc. Radiat. Transf.*, 78:41–53.

Rinsland, C., Gunson, M., Abrams, M., Lowes, L., Zander, R., and Mahieu, E. (1993). ATMOS/ATLAS 1 measurement of sulfur hexafluoride (SF_6) in the lower stratosphere and upper troposphere. *J. Geophys. Res.-Atmos.*, 98:20491–20494.

Rinsland, C., Mahieu, E., Zander, R., Gunson, M., Salawitch, R., Chang, A., Goldman, A., Abrams, M., Abbas, M., Newchurch, M., and Irion, F. (1996). Trends of OCS, HCN, SF_6, $CHClF_2$, (HCFC-22) in the lower stratosphere from 1985 and 1994 atmospheric trace molecule spectroscopy experiment measurements near 30 degrees n latitude. *Geophys. Res. Lett.*, 23:2349–2352.

Rinsland, C., Zander, R., Mahieu, E., Demoulin, P., Goldman, A., Ehhalt, D., and Rudolph, J. (1992b). Ground based infrared measurements of carbonyl sulphide total column abundances – long term trends and variability. *J. Geophys. Res.-Atmos.*, 97:5995–6002.

Rinsland, C. P., Gunson, M. R., Ko, M. K., Weisenstein, D. W., Zander, R., Godman, A., Sze, N., and Yue, G. (1995). H_2SO_4 photolysis: A source of sulfur dioxide in the upper stratosphere. *Geophys. Res. Lett.*, 22:1109–1112.

Rodgers, C. (1990). Characterization and error analysis of profiles retrieved from remote sounding measurements. *J. Geophys. Res.*, 95:5587–5595.

Rodgers, C. (2000). *Inverse Methods for Atmospheric Sounding: Theory and Practice*. World Scientific.

Rodhe, H. (1999). Human impact on the atmopsheric sulphur balance. *Tellus*, 51AB:110–122.

Rosenlof, K. and Holton, J. (1993). Estimates of the stratospheric residual circulation using the downward control. *J. Geophys. Res.*, 98:10465–10479.

Rotstayn, L. and Lohmann, U. (2002). Simulation of the tropospheric sulfur cycle in a global model with a physically based cloud scheme. *J. Geophys. Res.*, 107(D21):4592. doi:10.1029/2002JD002128.

Schoeberl, M., Douglass, A., Zhu, Z., and Pawson, S. (2003). A comparison of the lower stratospheric age spectra derived from a general circulation model and two data assimilation systems. *J. Geophys. Res.-Atmos.*, 108(D3):4113. doi:10.1029/2002JD002652.

Seinfeld and Pandis (1997). *Atmospheric Chemistry and Physics: From Air Pollution to Climate Change*. Wiley.

Shannon, C. E. and Weaver, W. (1949). *The mathematical theory of communication*. University of Illinois Press, 8th edition.

Spang, R., Remedios, J., and Barkley, M. (2004). Colour indices for the detection and differentiation of cloud types in infra-red limb emission spectra. *Adv Space Res*, 33:1041–1047.

Stevenson, D., Johnson, C., Highwood, E., Gauci, V., Collins, W., and Derwent, G. (2003). Atmospheric impact of the Laki eruption: Part 1 chemistry modelling. *Atmos. Chem. Phys.*, 3:487–507.

Strunk, M., Engel, A., Schmidt, U., Volk, C., Wetter, T., Levin, I., and Glatzel-Mattheier, H. (2000). CO_2 and SF_6 as stratospheric age tracers: consistency and the effect of mesospheric SF_6-loss. *Geophys. Res. Lett.*, 27 (3):341–344.

Sturges, W., Penkett, S., Barnola, J., Chappellaz, J., Atlas, E., and Stroud, V. (2001). A long-term record of carbonyl sulfide (COS) in two hemispheres from firn air measurements. *Geophys. Res. Lett.*, 28:4095–4098.

Timmreck, C. (2001). Three-dimensional simulation of stratospheric background aerosol: First results of a multiannual general circulation model simulation. *J. Geophys. Res.-Atmos.*, 106:28313–28332.

Ulshofer, V., Uher, G., and Andrae, M. (1995). Evidence for a winter sink of atmospheric carbonyl sulfide in the Northeast Atlantic-ocean. *Geophys. Res. Lett.*, 22:2601–2604.

Varanasi, P., Gopalan, A., and Brannon, J. (1992). Infrared absorption-coefficient data on SF_6 applicable to atmospheric remote-sensing. *J. Quant. Spectrosc. Radiat. Transf.*, 48:141–145.

Volk, C., Elkins, J., Fahey, D., Dutton, G., Gilligan, J., Loewenstein, M., Podolske, J., Chan, K., and Gunson, M. (1997). Evaluation of source gas lifetimes from stratospheric observations. *J. Geophys. Res.-Atmos.*, 102 (D21):25543–25564.

Warneck, P. (1988). *Chemistry of the Natural Atmosphere*. Academic Press. Chapter 10.

Watts, S. (2000). The mass budgets of carbonyl sulfide, dimethyl sulfide, carbon disulfide and hydrogen sulfide. *Atmos. Environ.*, 34:761–779.

Waugh, D. and Hall, T. (2002). Age of stratospheric air: Theory, observations, and models. *Rev. Geophys.*, 4:27.

Wayne, R. (1999). *Chemistry of Atmospheres, 3rd edition*. Wiley.

Weisenstein, D., Yue, G., Ko, M., Sze, N., Rodriguez, J., and Scott, C. (1997). A two-dimensional model of sulfur species and aerosols. *J. Geophys. Res.*, 102:13019–13035.

Weiss, P. and Andrews, S. (1995). Photoproduction of carbonyl sulphide in south pacific waters as a function of irradiation wavelength. *Geophys. Res. Lett*, 22:215–218.

WMO (2002). Scientific assessment of ozone depletion: 2002, global ozone research and monitoring project. Technical report, World Meteorological Organization. Report No. 47, 498pp., Geneva.

Yang, Z., Kong, L., Zhang, J., Wang, L., and Xi, S. (1998). Emission of biogenic sulfur gases from chinese rice paddies. *Sci. Total Environ.*, 224:1–8.

Zander, R. and et al. (1988). Concentrations of carbonyl sulphide and hydrogen cyanide in the free upper troposphere and lower stratosphere deduced from ATMOS/Spacelab-3 infrared solar occultation spectra. *J. Geophys. Res.-Atmos.*, pages 1669–1678.

Zander, R., Rinsland, C., and Demoulin, P. (1991). Infrared spectroscopic measurements of the vertical column abundance of sulfur-hexafluoride, SF_6, from the ground. *J. Geophys. Res.-Atmos.*, 96:15447–15454.

Zepp, R. and Andrae, M. (1994). Factors affecting the photochemical production of COS in seawater. *Geophys. Res. Lett*, 21:2813–2816.